



**A NUMERICAL METHODOLOGY FOR ASSESSING THE
HYDROKINETIC ENERGY POTENTIAL IN NATURAL
CHANNELS**

KAAJAL GOPIE

**MASTER'S DISSERTATION IN MECHANICAL SCIENCES
DEPARTAMENTO DE ENGENHARIA MECÂNICA**

Brasília, September 2022

**FACULDADE DE TECNOLOGIA
UNIVERSIDADE DE BRASÍLIA**

**UNIVERSIDADE DE BRASÍLIA
FACULDADE DE TECNOLOGIA
DEPARTAMENTO DE ENGENHARIA MECÂNICA**

**A NUMERICAL METHODOLOGY FOR ASSESSING THE
HYDROKINETIC ENERGY POTENTIAL IN NATURAL
CHANNELS**

**UMA METODOLOGIA NUMÉRICA PARA PREVER O
POTENCIAL HIDROCINÉTICO EM CANAIS NATURAIS**

KAAJAL GOPIE

**ORIENTADOR: TAYGOARA FELAMINGO DE OLIVEIRA, PROF.
DR., UNB**

**MASTER'S DISSERTATION IN MECHANICAL
SCIENCES**

PUBLICAÇÃO: PPGEA.TD-001/11

BRASÍLIA/DF: SEPTEMBRO - 2022

UNIVERSIDADE DE BRASÍLIA
FACULDADE DE TECNOLOGIA
DEPARTAMENTO DE ENGENHARIA MECÂNICA

A NUMERICAL METHODOLOGY FOR ASSESSING THE
HYDROKINETIC ENERGY POTENTIAL IN NATURAL
CHANNELS

KAAJAL GOPIE

DISSERTAÇÃO DE MESTRADO SUBMETIDA AO DEPARTAMENTO DE
ENGENHARIA MECÂNICA DA FACULDADE DE TECNOLOGIA DA UNIVERSIDADE
DE BRASÍLIA COMO PARTE DOS REQUISITOS NECESSÁRIOS PARA A
OBTENÇÃO DO GRAU DE MESTRADO.

APROVADA POR:

Taygoara Felamingo de Oliveira, Prof. Dr., UnB
Orientador

Cláudio José Cavalcante Blanco, Prof. Dr., UFPA
Membro Externo

Antonio Cesar Pinho Brasil Junior, Prof. Dr., UnB
Membro Interno

Edgar Amaral Silveira, Prof. Dr., UnB
Membro Suplente

BRASÍLIA, 16 DE SEPTEMBRO DE 2022.

FICHA CATALOGRÁFICA

GOPIE KAAJAL

A numerical methodology for assessing the hydrokinetic energy potential in natural channels [Distrito Federal] 2022.

xx, 83p., 210 x 297 mm (ENM/FT/UnB, Mestrado, Mechanical Sciences, 2022).

Master's Dissertation – Universidade de Brasília, Faculdade de Tecnologia.

Departamento de Engenharia Mecânica

- | | |
|--|----------------------------|
| 1. Escoamento em Canais Naturais | 2. Potencial Hidrocinético |
| 3. Simulação Numérica de Escoamentos Turbulentos | 4. Modelos de Turbulência |
| I. ENM/FT/UnB | |

REFERÊNCIA BIBLIOGRÁFICA

GOPIE, K. (2022). A numerical methodology for assessing the hydrokinetic energy potential in natural channels . Master's Dissertation em Mechanical Sciences, Publicação PPGEA.TD-001/11, Departamento de Engenharia Mecânica, Universidade de Brasília, Brasília, DF, 83p.

CESSÃO DE DIREITOS

AUTOR: Kaajal Gopie.

TÍTULO: A numerical methodology for assessing the hydrokinetic energy potential in natural channels .

GRAU: Mestrado

ANO: 2022

É concedida à Universidade de Brasília permissão para reproduzir cópias desta dissertação de mestrado e para emprestar ou vender tais cópias somente para propósitos acadêmicos e científicos. O autor reserva outros direitos de publicação e nenhuma parte desta dissertação de mestrado pode ser reproduzida sem autorização por escrito do autor.

Kaajal Gopie

Departamento de Engenharia Mecânica (ENM) - FT

Universidade de Brasília (UnB)

Campus Darcy Ribeiro

CEP 70919-970 - Brasília - DF - Brasil

*This work is dedicated to girls in
the world of engineering. Keep
breaking barriers!*

ACKNOWLEDGEMENTS

Commencing a new course in the middle of a worldwide pandemic can be daunting. The past two years certainly have been proven to be so. If it were not for certain people, the last years would have surely been difficult. First of all I would like to thank my parents for their unconditional support, even from afar. Next, my gratitude goes out to my supervisor, professor Taygoara, for his excellent guidance and patience during the last two years. I thank hereby also my colleague Isadora from the Equipe de simulação numérica em 3D. And especially, Rafael. Without your willingness to help me at any time, this work would not have been possible. Not to forget, my friends and colleagues both in Suriname and in Brazil at LEA, for keeping me company (some from a long distance) and helping me brainstorm through difficult phases of the research project. Two more important people deserve my thanks, for leading me in the direction of studying in Brazil and helping me navigate through the daily life there: professora Thelma and Prof. Rudi. As last, but most definitely not the least, I am grateful for the financial support provided through scholarships by Serra do Facão Energia S.A. (Sefac) for the development of the project Desenvolvimento de metodologia para determinação de potencial de energia hidrocínética em usinas hidroelétricas (ANEEL:P&D06899-2002/2020) and CAPES while obtaining my Master's degree at UnB.

RESUMO

Título: Uma metodologia numérica para prever o potencial hidrocínético em canais naturais

Autor: Kaajal Gopie

Orientador: Taygoara Felamingo de Oliveira, Prof. Dr., UnB

Programa de Pós-Graduação em Mechanical Sciences

Brasília, 16 de setembro de 2022

Neste trabalho, é apresentada uma metodologia numérica para avaliação do potencial hidrocínético em canais naturais. A metodologia é validada usando um canal de benchmark sinuoso cujos dados são disponíveis na literatura. O canal de benchmark é modelado e simulado empregando métodos de simulação numérica de escoamentos turbulentos considerando. Os resultados de referência são comparados com resultados gerados por três modelos de turbulência diferentes: o modelo $k - \varepsilon$ padrão, um modelo $k - \varepsilon$ modificado e um RSM. O RSM forneceu resultados mais consistentes com os da literatura. Este desenvolvimento comprova a metodologia proposta capaz de reproduzir o escoamento no canal benchmark. Portanto, a mesma metodologia pode ser empregada para simular o escoamento em um canal natural, juntamente com o modelo de turbulência provado como o mais consistente e proficiente na replicação do escoamento no canal benchmark. Como modelo geométrico para esta fase da pesquisa, são utilizados os dados batimétricos do canal à jusante da usina hidrelétrica da Sefac. Para avaliar o potencial hidrocínético disponível neste canal, são procuradas áreas com alta velocidade e profundidade. Um total de cinco áreas encontram-se em conformidade com esses requisitos. Destas cinco, três são encontradas para conter os maiores valores de velocidade ($\approx 1 \text{ m/s}$) e profundidade ($\approx 1.5 \text{ m}$). Essas áreas também foram estudadas quanto aos seus níveis de turbulência, para prolongar a vida útil das turbinas, analisando a ocorrência de correntes secundárias e perfis de intensidade de turbulência. Os níveis de turbulência, embora muito baixos em valores absolutos, são os mais altos próximos ao leito do canal, onde nenhuma turbina seria instalada, enquanto as correntes secundárias não foram observadas. Na contemplação de avaliar o potencial hidrocínético produzido anualmente por essas três áreas, foram simulados cenários de vazão adicionais, representando as vazões com ocorrências mais frequentes em um dado ano. Posteriormente, foram estudadas as velocidades nas três áreas previamente selecionadas para encontrar locais potenciais específicos para instalação de turbinas hidrocínéticas. No final, os três trechos têm potencial para instalação de um total de 24 turbinas, capazes de gerar $\approx 71 \text{ MWh}$ no ano de 2018.

Palavras-chave: Escoamento em Canais Naturais, Potencial Hidrocínético, Simulação Numérica de Escoamentos Turbulentos, Modelos de Turbulência.

ABSTRACT

Title: A numerical methodology for assessing the hydrokinetic energy potential in natural channels

Author: Kaajal Gopie

Supervisor: Taygoara Felamingo de Oliveira, Prof. Dr., UnB

Graduate Program in Mechanical Sciences

Brasília, September 16th, 2022

In this work, a numerical methodology for evaluating the hydrokinetic potential in natural channels is presented. The methodology is validated using a meandering benchmark channel found in the literature. The benchmark channel is modeled and simulated employing CFD tools. The results from the literature are compared to results generated by three different turbulence models: the standard $k - \varepsilon$ model, a modified $k - \varepsilon$ model and a RSM. The RSM is proven to be the most consistent and proficient at generating results similar to the literature. This development proves the proposed methodology capable of replicate the flow in the benchmark channel. Therefore, this methodology is employed for simulating the flow in a natural channel, along with the turbulence model proven to be the most consistent and proficient in reproducing the flow in the benchmark channel. As a geometric model for this phase of the research, the bathymetric data of the channel downstream of the Sefac hydroelectric facility is utilized. In order to assess the hydrokinetic potential available within this channel, areas with the highest velocities and depths of are desired. A total of five areas are found complying to these requirements. Out of these five areas, three are found to contain the highest velocities ($\approx 1 \text{ m/s}$) and depth ($\approx 1.5 \text{ m}$) values. These areas were also studied for their turbulence levels, to prolong the lifespan of the turbines, by analyzing the occurrence of secondary currents and turbulence intensity profiles. The turbulence levels, although negligible by their value, are found to be the highest near the channel bed, where no turbines would be installed, while the secondary currents are low to none. In contemplation of evaluating the hydrokinetic potential produced yearly by these three areas, additional flow rate scenarios were simulated, representing the most frequent occurring flow rates of the year 2018. Subsequently, the velocities in the three previously selected areas were studied to the end of finding specific potential locations for installing hydrokinetic turbines. Ultimately, the three sections allow for installing a total of 24 turbines, capable of generating a potential $\approx 71 \text{ MWh}$ in the year of 2018.

Keywords: Hydrokinetic Potential, Natural channel Flow, Turbulent Flow Numerical Simulation, Turbulence models.

SUMMARY

1	INTRODUCTION	1
1.1	OVERVIEW	1
1.2	NUMERICAL METHODS FOR ASSESSING THE HYDROKINETIC ENERGY POTENTIAL IN NATURAL CHANNELS.....	2
1.3	PROBLEM DEFINITION AND SCOPE OF WORK	4
1.4	OBJECTIVES	6
1.4.1	SPECIFIC OBJECTIVES	7
2	TURBULENT FLOW MODELING	8
2.1	NUMERICAL MODELING OF TURBULENT CHANNEL FLOW	8
2.1.1	MODELING TURBULENCE FOLLOWING THE RANS APPROACH ..	8
2.1.2	ALTERNATIVE APPROACHES FOR MODELING TURBULENT FLOW	13
2.2	STATE-OF-THE-ART ON OPEN-CHANNEL FLOW MODELING	14
2.3	DESCRIPTION OF THE SELECTED TURBULENCE MODELS.....	17
2.3.1	THE $k - \varepsilon$ MODEL	17
2.3.2	MODIFYING THE $k - \varepsilon$ MODEL: RNG $k - \varepsilon$ MODEL.....	18
2.3.3	THE RSM.....	19
3	METHODOLOGY	22
3.1	NUMERICAL METHOD VALIDATION	22
3.2	NUMERICAL SIMULATION OF THE SEFAC CHANNEL	27
3.2.1	INSTALLATION AREAS FOR THE HYDROKINETIC TURBINES.....	28
3.2.2	TURBINE SITING AND THE ANNUAL POTENTIAL POWER GEN- ERATION OF THE TURBINE FARM	28
4	RESULTS AND DISCUSSION	31
4.1	BENCHMARK SIMULATIONS	31
4.1.1	MESH GRID SENSITIVITY ANALYSIS.....	31
4.1.2	TURBULENCE MODEL ASSESSMENT	32
4.2	NUMERICAL RESULTS VALIDATION	39
4.2.1	VELOCITY STREAMLINES	39
4.2.2	PRESENCE OF SECONDARY FLOW.....	40
4.3	SEFAC CHANNEL MESH GRID ANALYSIS	41
4.4	DESCRIPTION SEFAC CHANNEL GEOMETRY.....	43
4.5	SELECTION OF INSTALLATION PLANES FOR THE TURBINES.....	44
4.5.1	INITIAL SELECTION	44

4.5.2 FINAL PLANE SELECTION.....	47
4.6 ANNUAL POWER GENERATION POTENTIAL OF THE STUDIED AREA....	57
4.6.1 TURBINE SITING DETAILS	57
4.6.2 OPTIMAL TURBINE LAYOUT ACCORDING TO PERIOD 1.....	57
4.6.3 OPTIMAL TURBINE LAYOUT ACCORDING TO PERIOD 2.....	59
4.6.4 DETERMINATION ANNUAL POTENTIAL POWER GENERATION	60
4.7 DISTINGUISHING CHARACTERISTIC OF THE SEFAC CHANNEL	65
5 CONCLUSION AND RECOMMENDATIONS.....	68
5.1 CONCLUSION	68
5.2 FUTURE WORKS	69
REFERENCES.....	70
A BATHYMETRIC DATA ACQUISITION	78
B HYDROKINETIC TURBINE ROTOR DESIGN AND TUR-	
BINE EFFICIENCY	80

LIST OF FIGURES

1.1	Sefac hydroelectric facility, showing the dam with the upstream and downstream channels, with the downstream channel showing signs of a slight curve, suggesting heightened secondary flow in that area.	6
1.2	Difference in streamwise velocity profiles caused by varying the open-channel width, in turn causing possible high turbulence. Derived from [23].....	6
2.1	Secondary flow vectors in the compound channel by [49], with a water level in the main channel H of 200 mm and $DR = 0.25$, the ratio between the water levels on the floodplain to main channel.....	15
2.2	Different types of secondary flow encountered in an open rectangular channel by Kang and Choi (2006) [35].	16
3.1	Benchmark channel design (a) plan view as constructed within the SERC-FCF with multiple bends to research secondary currents and a 45° compound trapezoidal (varying) cross section, presenting a likeness to morphology encountered in natural channels and (b) detailed geometry for straightforward adapting into the chosen designing software, derived from de Lima da Silveira e Lorena (1992) [39].....	24
3.2	Benchmark channel cross section of 45 ° of the meandering 60 ° channel designed by de Lima da Silveira e Lorena (1992) [39] with the eight studied regions per cross section as reported by Jing et al. (2011) [31]....	25
3.3	Channel domain with the studied sections as simulated by Jing et al. (2011) [31].	25
3.4	Monitoring points location in the Sefac channel mesh, with the first point nearest to the inlet.....	28
3.5	Daily measured and 20-day moving average flow rates with the two most frequent occurring flow rates in the Sefac channel during 2018.	29
4.1	Benchmark mesh grid analysis results for the turbulence intensity U for regions L3, L4 and L5, obtained by the $k - \varepsilon$ model.	33
4.2	Benchmark mesh grid analysis results for the turbulence intensity I for regions L3, L4 and L5, obtained by the $k - \varepsilon$ model.	34
4.3	Benchmark mesh grid analysis at two selected heights for the turbulence intensity I for regions L3, L4 and L5, obtained by the $k - \varepsilon$ model.	35
4.4	Benchmark mesh grid analysis at two selected heights for the average velocity U for regions L3, L4 and L5, obtained by the $k - \varepsilon$ model.	36

4.5	Results comparison among the simulated models in present work, experimental and numerical results derived from Jing et al. (2011) [31] for the longitudinal velocity u from regions L3, L4 and L5. The \star and $+$ graphs are assigned to the numerical and experimental results by Jing et al. (2011) [31] while the green, red and purple lines represent the simulated results by respectively the $k - \varepsilon$, the RNG $k - \varepsilon$ model and the RSM.....	37
4.6	Results comparison among the simulated models in present work, experimental and numerical results derived from Jing et al. (2011) [31] for the transverse velocity v from regions L3, L4 and L5. The \star and $+$ graphs are assigned to the numerical and experimental results by Jing et al. (2011) [31] while the green, red and purple lines represent the simulated results by respectively the $k - \varepsilon$, the RNG $k - \varepsilon$ model and the RSM.....	38
4.7	Velocity contours and streamlines for case 3, obtained by (a) present research and both (b) numerically and (c) experimentally by Jing et al. (2011) [31].	40
4.8	Rotating secondary flow vectors for case 3, obtained numerically employing (a) the RSM and (b) derived from Jing et al. (2011) [31].....	41
4.9	Velocity U and turbulence intensity I profiles by the RSM for the three meshes.	43
4.10	Selected velocity U and turbulence intensity I values plotted against the mesh size obtained by the RSM.	43
4.11	Channel bed of the Sefac channel, obtained by the experimental data collection team with the Chasing Dory underwater drone.....	44
4.12	Depth contours obtained by the RSM simulation with the deepest area located right after the inlet and the shallowest areas at the channel banks, indicating a compound channel cross section.....	45
4.13	Velocity contours obtained by the RSM, with the free surface showing yellow-green to red contours as high velocity areas.	45
4.14	Velocity contour map with initially selected transverse planes and their width y for installing the turbines located in potentially high velocity and sufficient depth areas.	46
4.15	Local velocity contours of plane 1 focused on the four selected regions, starting at the left side of the plane (from the inlet's point of view) with P1 and ending with P4, along with the maximum depth for further analysis of the velocity and turbulence levels.	47

4.16	Local velocity contours of plane 2 focused on the four selected regions, starting at the left side of the plane (from the inlet's point of view) with P1 and ending with P4, along with the maximum depth for further analysis of the velocity and turbulence levels.	47
4.17	Local velocity contours of plane 3 focused on the four selected regions, starting at the left side of the plane (from the inlet's point of view) with P1 and ending with P4, along with the maximum depth for further analysis of the velocity and turbulence levels.	48
4.18	Local velocity contours of plane 4 focused on the four selected regions, starting at the left side of the plane (from the inlet's point of view) with P1 and ending with P4, along with the maximum depth for further analysis of the velocity and turbulence levels.	48
4.19	Local velocity contours of plane 5 focused on the four selected regions with the highest depth and velocity values, starting at the left side of the plane (from the inlet's point of view) with P1 and ending with P4, along with the maximum depth for further analysis of the velocity and turbulence levels.	49
4.20	Simulated velocity profiles of the four studied regions for plane 1 with a mass flow rate \dot{m} of 91000 kg/s	50
4.21	Simulated velocity profiles of the four studied regions for plane 2 with a mass flow rate \dot{m} of 91000 kg/s	51
4.22	Simulated velocity profiles of the four studied regions for plane 3 with a mass flow rate \dot{m} of 91000 kg/s	52
4.23	Simulated velocity profiles of the four studied regions for plane 4 with a mass flow rate \dot{m} of 91000 kg/s	53
4.24	Simulated velocity profiles of the four studied regions for plane 5 with a mass flow rate \dot{m} of 91000 kg/s	53
4.25	Secondary flow and vector fields focused on the four selected regions with the highest depth and velocity values in the plane, P1-P4, for sections (a) 1, (b) 2 and (c) 5. The secondary flow field is given by plotting the transverse velocity v contours.	54
4.26	Turbulence intensity profiles of the four studied regions for plane 1 simulated with a mass flow rate of 91000 kg/s	55
4.27	Turbulence intensity profiles of the four studied regions for plane 2 simulated with a mass flow rate of 91000 kg/s	55
4.28	Turbulence intensity profiles of the four studied regions for plane 5 simulated with a mass flow rate of 91000 kg/s	56
4.29	Simulated velocity profiles of plane 1 with a mass flow rate \dot{m} of 51390 kg/s	58

4.30	Simulated velocity profiles of plane 2 with a mass flow rate \dot{m} of 51390 kg/s .	59
4.31	Simulated velocity profiles of plane 5 with a mass flow rate \dot{m} of 51390 kg/s .	60
4.32	Simulated velocity profiles of plane 1 with a mass flow rate \dot{m} of 158720 kg/s .	61
4.33	Simulated velocity profiles of plane 2 with a mass flow rate \dot{m} of 158720 kg/s .	62
4.34	Simulated velocity profiles of plane 5 with a mass flow rate \dot{m} of 158720 kg/s .	63
4.35	Local velocity contours and depth for a mass flow rate \dot{m} of 158720 kg/s used for determining the available width for installation of the turbines for planes (a) 1, (b) 2 and (c) 5. The planes display the available width to its best advantage, causing the colder and warmer colours (respectively the lowest and highest velocities), similar to the contours found in Figures 4.15, 4.16 and 4.19, to be excluded.	64
4.36	Longitudinal velocity u with velocity streamlines of the longitudinal section (side view) of the depression area for mass flow rates \dot{m} (a) 47410 and (b) 158720 kg/s .	65
4.37	Transverse velocity v with velocity streamlines of the cross section of the depression area for mass flow rates \dot{m} (a) 47410 and (b) 158720 kg/s .	66
A.1	Setup of the field experiments through a (a) boat with (b) the ADP assembly.	78
A.2	Boat trajectories on the channel taken for the measured depth.	79
B.1	Rotor design.	82
B.2	Estimated performance curve for the rotor design.	83

LIST OF TABLES

3.1	Case 3 inlet values by Jing et al. (2011) [31].	25
4.1	Mesh sizes for the benchmark mesh grid analysis.	31
4.2	Processing time for the simulations employing different benchmark channel mesh sizes.	32
4.3	Mesh sizes for the natural channel mesh grid analysis.	42
4.4	Processing time for the simulations employing different natural channel mesh sizes.	42
4.5	Simulated velocities for planes 1, 2 e 5 with a mass flow rate \dot{m} of 51390 kg/s	58
4.6	Simulated velocities for planes 1, 2 and 5 with a mass flow rate \dot{m} of 158720 kg/s	61
4.7	Mean velocity per section for a mass flow rate \dot{m} of 158720 kg/s	62
4.8	Calculated converted power $P_{converted}$ per installation site for a mass flow rate \dot{m} of 158720 kg/s	62
4.9	Annual potential power generation $P_{converted}$ of the turbine layout for 2018.	63
B.1	Inlet parameters of the rotor design based on Blade Element Method (BEM).	82
B.2	Geometry of the resulting blade following the algorithm for the blade design.	82

LIST OF SYMBOLS

Greek symbols

Ω_{ij}	Vorticity tensor in the ij -direction for the mean field	[1/s]
Ω_{ik}	Vorticity tensor in the ik -direction for the mean field	[1/s]
Ω_{kj}	Vorticity tensor in the kj -direction for the mean field	[1/s]
Π_{ij}	Turbulent pressure-strain term in the SSG and the Reynolds stress equation RSM	[Pa/s]
τ_{ii}	Reynolds stress tensor in the ii -direction	[m ² /s ²]
τ_{ij}	Reynolds stress tensor in the ij -direction	[m ² /s ²]
τ_{ik}	Reynolds stress tensor in the ik -direction	[m ² /s ²]
τ_{jk}	Reynolds stress tensor in the jk -direction	[m ² /s ²]
τ_{kl}	Reynolds stress tensor in the kl -direction	[m ² /s ²]
ε_{ii}	Turbulent kinetic energy dissipation rate in the ii -direction	[m ² /s ³]
ε_{ij}	Turbulent kinetic energy dissipation rate in the ij -direction	[m ² /s ³]
ε_{in}	Turbulent kinetic energy dissipation rate at the inlet	[m ² /s ³]
ε	Turbulent kinetic energy dissipation rate	[m ² /s ³]
μ_T	Turbulent dynamic viscosity	[Pa·s]
μ	Dynamic viscosity	[Pa·s]
ω	Angular velocity	[rad/s]
ϕ	Inflow angle	[°]
ρ	Fluid density	[kg/m ³]
ϑ_T	Turbulent kinematic viscosity	[m ² /s]
ϑ	Kinematic viscosity	[m ² /s]

Latin symbols

A	Cross sectional area	[m ²]
C	Blade cord length	[m]
DR	Relative water depth	[m]
D	Diameter	[m]
H	Water depth	[m]
L_μ	Turbulent length scale	[m]
$P_{available}$	Available power	[Watt]
$P_{converted}$	Converted power	[Watt]
P_{ij}	Turbulence production term for the Reynolds stress equation	[m ² /s ³]
P_k	Turbulence production term	[m ² /s ³]
Q	Volumetric flow rate	[m ³ /s]

R	(hydraulic) radius	[m]
S_{ij}	Mean strain-rate in the ij -direction	[1/s]
S_{ik}	Mean strain-rate in the ik -direction	[1/s]
S_{jk}	Mean strain-rate in the jk -direction	[1/s]
S_{kj}	Mean strain-rate in the kj -direction	[1/s]
S_{lk}	Mean strain-rate in the lk -direction	[1/s]
S	Strain-rate tensor	[1/s]
T	Torque	[Nm]
U_∞	Turbine inlet velocity	[m/s]
U_{in}	Inlet velocity	[m/s]
U_{sim}	Simulated velocity	[m/s]
U	Velocity obtained by calculating the vector of the u , v and w component	[m/s]
W_{ij}	Rotation tensor in the ij -direction for the SSG RSM	[1/s]
W_{ik}	Rotation tensor in the ik -direction for the SSG RSM	[1/s]
W_{jk}	Rotation tensor in the jk -direction for the SSG RSM	[1/s]
\tilde{U}_i	Instantaneous mean velocity in the i -direction	[m/s]
\tilde{p}	Instantaneous mean pressure	[Pa]
\dot{m}	Mass flow rate	[kg/s]
$\overline{\tilde{U}_i \tilde{U}_j'}$	Reynolds stress tensor according to the Boussinesq hypothesis	[m ² /s ²]
$\overline{\tilde{U}_i}$	Time-averaged velocity in the i -direction	[m/s]
$\overline{\tilde{U}_j}$	Time-averaged velocity in the j -direction	[m/s]
$\overline{\tilde{U}_k}$	Time-averaged velocity in the k -direction	[m/s]
$\overline{\tilde{p}}$	Time-averaged pressure	[Pa]
$\overline{u'u'}$	Reynolds stress tensor according to the Boussinesq hypothesis in the uu -direction	[m ² /s ²]
$\overline{u'v'}$	Reynolds stress tensor according to the Boussinesq hypothesis in the uv -direction	[m ² /s ²]
$\overline{u'w'}$	Reynolds stress tensor according to the Boussinesq hypothesis in the uw -direction	[m ² /s ²]
$\overline{v'v'}$	Reynolds stress tensor according to the Boussinesq hypothesis in the vv -direction	[m ² /s ²]
$\overline{v'w'}$	Reynolds stress tensor according to the Boussinesq hypothesis in the vw -direction	[m ² /s ²]
$\overline{w'w'}$	Reynolds stress tensor according to the Boussinesq hypothesis in the ww -direction	[m ² /s ²]
\tilde{U}_i'	Instantaneous fluctuating velocity in the i -direction	[m/s]
\tilde{U}_j'	Instantaneous fluctuating velocity in the j -direction	[m/s]
\tilde{U}_k'	Instantaneous fluctuating velocity in the k -direction	[m/s]

\tilde{U}_i	Instantaneous mean velocity in the i -direction	[m/s]
\tilde{U}_j	Instantaneous mean velocity in the j direction	[m/s]
\tilde{U}	Instantaneous velocity	[m/s]
\tilde{p}'	Instantaneous fluctuating pressure	[Pa]
\tilde{p}	Instantaneous mean pressure	[Pa]
d_{ij}	Diffusion tensor in the RSM and Reynolds stress equation	[m ² /s ³]
d	Diffusion term in the turbulent kinetic energy equation	[m ² /s ³]
h	Floodplain/bankfull water depth	[m]
k_{in}	Inlet turbulent kinetic energy	[m ² /s ²]
k	Turbulence kinetic energy	[m ² /s ²]
r	Radius of annulus	[m]
t	Time	[s]
u'	Fluctuating longitudinal velocity	[m/s]
u	Longitudinal velocity	[m/s]
v'	Fluctuating transverse velocity	[m/s]
v	Transverse velocity	[m/s]
w'	Fluctuating normal velocity	[m/s]
w	Vertical velocity	[m/s]
x_i	X-component in the i -direction	[m]
x_j	X-component in the j -direction	[m]
x_k	X-component in the k -direction	[m]
x_l	X-component in the l -direction	[m]
y	Distance along a transverse (river) section	[m]

Dimensionless symbols

C_μ	Constant in the Boussinesq approach
$C_{\varepsilon 1}$	Constant for the RNG $k - \varepsilon$ models
$C_{\varepsilon 2}$	Constant for the RNG $k - \varepsilon$ models
C_ε	Constant in the transport equation for ε in the RSM
C_d	Drag coefficient
C_l	Lift coefficient
C_n	Variable based on the lift and drag coefficient
C_s	Constant for the diffusion tensor in the RSM
C_t	Variable based on the lift and drag coefficient
C_p	Power coefficient
F	Correction function for blade tip and hub losses
I	Turbulence intensity
N_b	Number of blades
δ_{ij}	Kronecker delta in the ij -direction

δ_{ik}	Kronecker delta in the ik -direction
δ_{jk}	Kronecker delta in the jk -direction
λ	Tip speed ratio
a'	Tangential induction factor
a	Axial induction factor
b_{ik}	Anisotropy tensor in the ik -direction
b_{jk}	Anisotropy tensor in the jk -direction
b_{kl}	Anisotropy tensor in the kl -direction
b_{mn}	Anisotropy tensor in the mn -direction
b_{nm}	Anisotropy tensor in the nm -direction
α_0	Empirical constant for the turbulent pressure-strain term in the SSG RSM
α_1	Empirical constant for the turbulent pressure-strain term in the SSG RSM
α_2	Empirical constant for the turbulent pressure-strain term in the SSG RSM
α_3	Empirical constant for the turbulent pressure-strain term in the SSG RSM
α_4	Empirical constant for the turbulent pressure-strain term in the SSG RSM
α_5	Empirical constant for the turbulent pressure-strain term in the SSG RSM
b_{ij}	Anisotropy tensor in the ij -direction
β	Constant for the RNG $k - \varepsilon$ model
η_0	Constant for the RNG $k - \varepsilon$ model
η	Expansion parameter for the RNG $k - \varepsilon$ model
π	Ratio of circumference of circle to its diameter
σ_ε	Constant for the $k - \varepsilon$ model
σ_k	Constant for the $k - \varepsilon$ model
y^+	The dimensionless distance from vertex to wall

LIST OF ACRONYMS AND ABBREVIATIONS

2D	two-dimensional. 1, 3, 8, 14, 22, 31, 68
3D	three-dimensional. 1, 2, 8, 10, 13, 14, 22, 31, 68
ADCP	Acoustic Doppler Current Profiler. 1, 2, 8, 22, 31, 68
ADP	Acoustic Doppler Profiler. 1, 8, 22, 31, 68, 70, 78
BEM	Blade Element Method. xiv, 1, 8, 22, 31, 68, 81
BEMT	Blade Element Momentum Theory. 1, 8, 22, 31, 68, 80
CFD	Computational Fluid Dynamics. i, 1, 4, 5, 8, 22, 31, 68
DEM	digital elevation model. 1, 3, 8, 22, 31, 68
DNS	Direct Numerical Simulation. 1, 8, 13, 22, 31, 68
FVCOM	Finite Volume Community Ocean Model. 1, 3, 8, 22, 31, 68
GIS	Geographical Information System. 1, 3, 8, 22, 31, 68
HR	Research Council Ltd.. 1, 8, 14, 22, 31, 68
HYCOM	Hybrid Coordinate Ocean Model. 1, 3, 8, 22, 31, 68
HYDROKAL	hydrokinetic calculator. 1, 3, 8, 22, 31, 68
LES	Large-eddy simulation. 1, 8, 13, 22, 31, 68
NS	Navier-Stokes. 1, 8, 11, 13, 22, 31, 68
PDE	partial differential equation. 1, 8, 12, 22, 31, 68
RAM	Random-access Memory. 1, 8, 22, 31, 32, 68
RANS	Reynolds-averaged Navier-Stokes. viii, 1, 6, 8, 9, 11, 13, 14, 16, 22, 31, 68, 69
RNG	Renormalization Group. viii, xi, xvii, xviii, 1, 8, 18, 22, 26, 31, 32, 35, 37, 38, 68
ROMS	Regional Ocean Modeling System. 1, 3, 8, 22, 31, 68

RSM	Reynolds Stress Model. i, viii, xi, xv–xviii, 1, 8, 12, 13, 15, 16, 19, 20, 22, 26, 31, 32, 35, 37–41, 43–45, 57, 65, 68
Sefac	Serra do Facão Energia S.A.. x, xi, 1, 2, 5, 6, 8, 22, 27–29, 31, 43, 44, 65, 68, 70, 78
SERC	Science and Engineering Council. 1, 8, 14, 22, 31, 68
SERC-FCF	Science and Engineering Council Flood Channel Facility. x, 1, 8, 14, 15, 22, 24, 31, 68
SSG	Speziale, Sarkar and Gatski. xv, xvi, xviii, 1, 8, 20, 22, 26, 31, 68
SWAT	Soil and Water Assessment Tool. 1, 3, 8, 22, 31, 68
UnB	University of Brasília. 1, 2, 5, 8, 22, 31, 68
URANS	Unsteady Reynolds-averaged Navier-Stokes. 1, 8, 13, 22, 31, 68

1 INTRODUCTION

"Nothing in life is to feared, it is only to be understood. Now is the time to understand more, so that we may fear less."

-Marie Curie, Polish-French physicist

1.1 OVERVIEW

With the world's fossil fuel supply coming to an end, alternative energy sources must be explored. A sustainable, but foremost, environment friendly alternative, are renewable energy sources. Out of all renewable energy forms, hydropower is known to be the most efficient and largest resource. Almost 60% of the energy generation in Brazil relies on the conversion of hydropower into electricity, provided by hydroelectric facilities [46, 43]. However, research has shown that the water flowing downstream of the facilities still contains energy in the currents to generate yet even more electricity. This type of energy can be harvested by applying the hydrokinetic technology [26, 38]. This conversion method eradicates the need for the construction of a dam or water reservoirs for hydroelectric facilities, as no or little elevation is needed for the energy generation [44]. The hydrokinetic energy is harvested by hydrokinetic turbines, whose rotors are brought in movement by the water currents, converting the available kinetic energy into mechanical power and generating electrical currents using generators. The energy is extracted from the fluid by the decreasing flow velocity [25, 38].

Hydrokinetic turbines have simple designs, are easy to transport, and can be installed with a low environmental impact. These applications turn the turbine versatile and capable of being used in several coastal or river locations [27], not limiting its use to only channels downstream of hydroelectric facilities. Installing the turbines at ideal installation sites containing a high hydrokinetic energy potential, optimizes the conversion of energy.

A possible numerical method to study the hydrokinetic energy potential in natural channels would be to model and simulate the river flow. In order to complete this task, the velocity, depth and relief of the river bed, in other words, the bathymetry, are necessary [48]. Potentially high hydrokinetic energy areas are encountered where the water is fast-moving in the channel, signifying high velocities. Thus, the potential

can be determined by mapping out the velocity field [7]. In contemplation of installing the turbines, a sufficient amount of depth is also required.

Perceiving the benefits of exploiting the remanescent kinetic energy in the water flowing downstream of their hydroelectric facility through hydrokinetic technology, the Serra do Facão Energia S.A. (Sefac), a Brazilian private company focused mainly on the electric power sector, operating the Serra do Facão electrical power plant (in portuguese: Usina Hidrelétrica Serra do Facão), has entrusted a group of researchers, under the name of team Lambari (in portuguese: *equipe Lambari*), at the University of Brasília (UnB) with the responsibility and financial support of carrying out the project: The development of a methodology to determine the hydrokinetic energy potential in hydroelectric facilities (in portuguese: *Desenvolvimento de metodologia para determinação de potencial de energia hidrocínética em usinas hidroelétricas*). This author is part of the three-dimensional (3D) numerical simulation team, where the channel downstream of the Sefac hydroelectric facility, henceforth known as the Sefac channel in this work, is used as a model for testing out the developed methodology.

1.2 NUMERICAL METHODS FOR ASSESSING THE HYDROKINETIC ENERGY POTENTIAL IN NATURAL CHANNELS

Methods for assessing the hydrokinetic energy in natural channels are still in development, thus comes forth the purpose of this research. However, over the years, promising progress has been made in numerically determining this renewable energy resource. The site properties for such studies consist out of [50]:

- The bathymetry for modeling the natural channel collected by Acoustic Doppler Current Profilers (ADCPs);
- Velocity distribution along the channel collected by ADCPs for calibrating the numerical models;
- Bed surface and sediment properties, as they may change the bathymetry, hence influence the flow field;
- The temperature, density and kinematic viscosity serving as important properties in characterizing the properties.

Not all site properties are used for estimating the hydrokinetic potential in researches. However, all researches agree on one site property imperative to the assessment: the velocity distribution. The literature review reveals one numerical method

used predominantly for assessing the hydrokinetic potential. This method contains an assessment carried out through the use of a hydrodynamic model. For implementing the hydrodynamic model, data on the flow rate, bathymetry and digital elevation model (DEM) of the concerning area is necessary. The model can be used to simulate the current, from tidal (including straits and estuaries) [55] and ocean [33] to river [47]. The assessments using this model have been mostly realized for tidal current energy, using various well known hydrodynamic models, such as Hybrid Coordinate Ocean Model (HYCOM) [33], Regional Ocean Modeling System (ROMS) [20] and the Finite Volume Community Ocean Model (FVCOM) [53]. Another numerical method for assessing the hydrokinetic potential is realized through the use of a hydrological model. This model is able to simulate the changing flow rates due to precipitation and the terrain characteristics [50, 36]. In Ali et al. (2020) [2], a Geographical Information System (GIS) was utilized in combination with a Soil and Water Assessment Tool (SWAT) for determining the theoretical hydrokinetic energy in U-Tapao river basin in southern Thailand. According to this study, the theoretical potential depends the most on the hydraulic head and the flow rates of the studied area. The GIS-based technique was used for calculating the hydraulic head, whereas the flow rates were simulated by the hydrological model. For setting up the hydrological model, information on the geometry of the studied area in the form of the topography (DEM), land-use, soil map and slope maps were required, along with meteorological data to simulate the flow. In the case of incomplete information, such as the daily velocity data series, the flow-velocity model by Cruz et al. (2020) [16] can be applied to obtain the velocity distribution along river cross sections to eventually determine the hydrokinetic potential in a natural channel. In their work, the authors apply this model to the Amazon basin. The model employs known flow rates along with a random cross sectional area from the channel to obtain the velocity distribution along the cross section and predict the daily average velocity and finally estimate the hydrokinetic potential. Another numerical study conducted for natural channels in similar circumstances as in present work, is found in Holanda et al. (2017) [18]. This work assesses the hydrokinetic potential in the tailwater of the Tucuruí hydroelectric facility in the Tocantins River. This study employs a hydrodynamic model, the Saint-Venant model, in 2D. The study was able to determine turbine sites by considering the current velocity and the energy density. Available also for evaluating the potential hydrokinetic energy in rivers is the numerical tool, hydrokinetic calculator (HYDROKAL) by Duvoy et al. (2012) [21]. This tool is programmed within Fortran 90 as an extension of the hydrodynamic model CCHE2D, developed at the National Center for Computational Hydroscience and Engineering, University of Mississippi. The simulated velocities by CCHE2D are employed within HYDROKAL to calculate the instantaneous power density. The potential hydrokinetic energy is determined after considering also a user-defined turbine efficiency.

As has been discussed in the review above, most numerical studies are conducted through hydrodynamic models. Up till now, a computational mesh produced from bathymetric data and generated employing solely CFD tools, similar to the mesh to be generated in present study, has only been encountered in Santos et al. (2019) [48], where the authors realize a hydrokinetic potential and economic analysis of hydrokinetic turbines implementation in two rivers. It is also noted, that in previous studies, the aim of turbine siting lies more on extracting the highest amount of energy from a potential site (employing also a known turbine efficiency as demonstrated by Holanda et al. (2017) [18], Cruz et al. (2020) [16] and Duvoy et al. (2012) [21]), rather than determining an optimal turbine installation site, as most studies strictly focus only on the velocity and/or depth and do not consider the negative impact of turbulence on the turbines.

Taking these two factors into consideration, the main contribution of this work to the literature and scientific community is to fill in the knowledge gaps created by both the lack of meshes based on bathymetric data produced with CFD tools and neglect of the negative impact of high turbulence levels on turbines. High turbulence levels will be procured through secondary flow and the local turbulence intensity. Furthermore, this research will provide the reader with the results of multiple turbulence models, ultimately determining the most accurate model for the proposed numerical method. An emphasis is placed on turbine siting by taking an important factor like turbulence and results from the turbulence model most accurately to simulate natural channel flow, into consideration.

1.3 PROBLEM DEFINITION AND SCOPE OF WORK

One of the greatest difficulties in estimating the hydrokinetic potential in natural channels is the difficulty in modeling the velocity field. In open-channels, interactions between the channel bed, walls and the free surface determine the velocity profile from channel bed to the direction of the water surface. In the real-world, this channel can assume the shape of various intricate geometries, such as with slopes, expansions and contractions, compound or trapezoidal cross sections, meandering, straight or braided channels. The interactivity between the channel bed, walls and the free surface for a non-uniform geometry cause an uneven shear stress near the bed, causing an unsteadiness in the vertical velocity profile with a high velocity near the free surface. Figure 1.2 shows how increasing only the width can already noticeably influence the streamwise velocity profile in a smooth rectangular inclined open-channel. The unsteadiness in velocity profiles may be amplified by the presence of secondary flow, as they cause the

streamwise velocity to yet even more diverge, especially in the more complex geometries, affecting the bed shear stress and causing a potentially a higher turbulence level in the concerning area [48, 56].

With all the information presented up until now, the problem can be defined as numerically capturing the flow adequately in a natural channel is a complicated task.

Using Computational Fluid Dynamics (CFD) allows for a more complete and detailed modeling of the channel flow. In order to ascertain the viability of modeling the flow employing CFD tools, a validation will first be conducted in chapter 4.1. The modeled flow will be compared to data retrieved from a consolidated reference, also displaying the occurrence of secondary flow. The next research phase concerns converting the bathymetric data of a natural channel into a geometric model to be simulated with CFD software in chapter 4.3. As geometric model, the bathymetric data of the channel downstream of the Sefac hydroelectric facility in the São Marcos in the state of Goiás in Brazil (Fig. 1.1), will be employed to generate a computational mesh of the resulting geometry and simulated procuring for suitable sites using a high velocity and sufficient depth as main deciding factors in chapter 4.5. This channel is studied as a result of the association between the UnB and Serra do Facão Energia S.A.. For determining the hydrokinetic turbine installation sites, more information will be necessary to estimate the energy conversion of the available hydrokinetic energy. Other than studying high velocity areas, local levels of turbulence will also be studied in chapter 4.5.2 to lower the negative impact on the turbine efficiency and lifespan. For the same reasons, areas with secondary currents must also be avoided as they indicate areas of high turbulence. The finalized sites will be integral to estimating the potential annual hydrokinetic power generation in chapter 4.6. The detailed research methodology is given in chapter 3, with the necessary theory behind turbulent flow modeling and advances in this area in chapter 2. The final remarks regarding this research are presented in chapter 5.



Figure 1.1 – Sefac hydroelectric facility, showing the dam with the upstream and downstream channels, with the downstream channel showing signs of a slight curve, suggesting heightened secondary flow in that area.

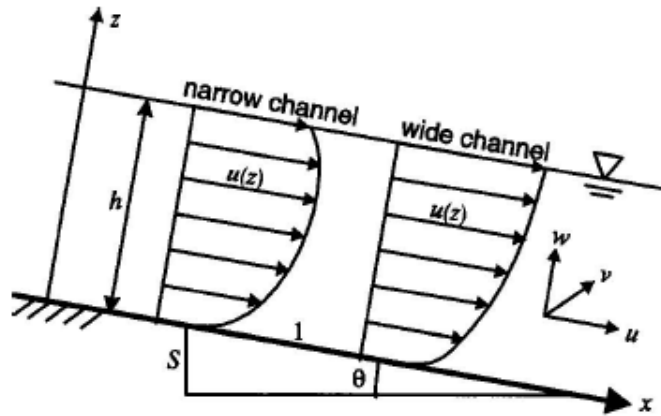


Figure 1.2 – Difference in streamwise velocity profiles caused by varying the open-channel width, in turn causing possible high turbulence. Derived from [23].

1.4 OBJECTIVES

The main objective of this study is to develop a numerical methodology, employing Reynolds-averaged Navier-Stokes (RANS) turbulence models, to assess the hydrokinetic potential in natural channels, through determining optimal installation points for horizontal axis turbines, decided by the highest velocities, sufficient (lowest) depths and low turbulence areas.

1.4.1 Specific objectives

To genuinely consolidate a trustworthy, versatile and accurate methodology, the study will consist out of two main stages:

1. Validation of the proposed methodology;
2. Employ the validated methodology to determine ideal turbine installation sites, and ultimately determine the annual power generation for the natural channel model.

The validation of the proposed methodology must achieve the following specific objectives:

- The selection of a benchmark channel with similar characteristics to a natural channel and available experimental data for validating the proposed methodology;
- A mesh grid analysis with the modeled benchmark channel to configure the computational mesh;
- A turbulence model performance study to ascertain the turbulence model predicting results closest to the reference data;
- Acceptability of the simulated data as compared to the experimental data;
- Predict the presence of secondary flow.

The validated numerical method is subsequently used for attaining the following objectives:

- Model the natural channel using the collected bathymetric data from field experiments;
- Configure the natural channel computational mesh with a mesh grid study;
- Determine optimal installation sites for the turbines, taking into consideration high velocity areas, adequate depth and local turbulence levels;
- Determine the estimated annual potential power generation capacity of the installed hydrokinetic turbine farm by studying the most frequent occurring flow rates.

2 TURBULENT FLOW MODELING

"That we have written an equation does not remove from the flow of fluids its charm or mystery or its surprise."

-Richard Feynman, American theoretical physicist

2.1 NUMERICAL MODELING OF TURBULENT CHANNEL FLOW

2.1.1 Modeling turbulence following the RANS approach

The motion of an incompressible fluid can be described by the Navier-Stokes (NS) equations, as presented below

$$\frac{\partial \tilde{U}_i}{\partial t} + \tilde{U}_j \frac{\partial \tilde{U}_i}{\partial x_j} = -\frac{1}{\rho} \frac{\partial \tilde{p}}{\partial x_i} + \vartheta \frac{\partial^2 \tilde{U}_i}{\partial x_j^2}. \quad (2.1)$$

Along with the NS equations, the equation of continuity is also solved

$$\frac{\partial \tilde{U}_i}{\partial x_i} = 0, \quad (2.2)$$

in which \tilde{U} is the instantaneous fluid velocity, ϑ the fluid kinematic viscosity, ρ the density of the fluid and \tilde{p} the fluid pressure. The continuity equation stands for the conservation of mass, while the NS equations represent the conservation of momentum. For simple geometries or laminar flow, solving these equations does not present much of a problem. However, in the case of complex geometries or turbulent flows, with more forces at work, solving these equations turns much more complicated. Solving the NS equations for this problem would require a fine mesh in order to solve all the occurring eddies in the fluid. This would result in an extreme high amount of computational power, unable to be provided by even a supercomputer. The turbulence occurring within these flows can be approached by statistical methods. Turbulence has no predictable behavior, as it demonstrates fluctuations in time and space, thus a time averaging might be answer to solving the occurring eddies. This averaging is obtained by the RANS approach [15, 19]. This approach first uses the Reynolds decomposition to separate the turbulent quantities, the velocity \tilde{U} and the pressure \tilde{p} , into an mean and fluctuating component

$$\tilde{U}_i = \bar{U}_i + \tilde{U}'_i, \quad (2.3)$$

$$\tilde{p} = \bar{p} + \tilde{p}'. \quad (2.4)$$

Substituting the division of the turbulence quantities into the continuity equation and averaging this equation results in

$$\frac{\partial \bar{\tilde{U}}_i}{\partial x_i} = 0. \quad (2.5)$$

The RANS equations are obtained following the same procedure as employed for the continuity equation

$$\frac{\partial \bar{\tilde{U}}_i}{\partial t} + \bar{\tilde{U}}_j \frac{\partial \bar{\tilde{U}}_i}{\partial x_j} = -\frac{1}{\rho} \frac{\partial \bar{p}}{\partial x_i} + \frac{\partial}{\partial x_j} \left(\vartheta \frac{\partial \bar{\tilde{U}}_i}{\partial x_j} - \overline{\tilde{U}'_i \tilde{U}'_j} \right). \quad (2.6)$$

Multiplying the RANS equations with the density ρ and rearranging the terms results in the following non linear equation for the turbulent flow

$$\rho \bar{\tilde{U}}_j \frac{\partial \bar{\tilde{U}}_i}{\partial x_j} = \rho + \frac{\partial}{\partial x_j} \left(-\bar{p} \delta_{ij} + 2\mu S_{ij} - \rho \overline{\tilde{U}'_i \tilde{U}'_j} \right), \quad (2.7)$$

in which $\bar{\tilde{U}}_j$ and $\bar{\tilde{U}}_i$ are the time-averaged velocities, μ the dynamic viscosity, δ_{ij} the Kronecker delta and S_{ij} the mean strain-rate of the tensor, defined as

$$S_{ij} = \frac{1}{2} \left(\frac{\partial \bar{\tilde{U}}_i}{\partial x_j} + \frac{\partial \bar{\tilde{U}}_j}{\partial x_i} \right). \quad (2.8)$$

The three terms between the brackets in Eq. (2.7) represent respectively the mean pressure stress, mean viscous stress tensor and the Reynolds stress tensor $\overline{\tilde{U}'_i \tilde{U}'_j}$ multiplied with the density ρ . Comparing Eq. (2.7) to Eq. (2.1) shows the Reynolds stress tensor as an additional term added after the viscous term on the right-hand side [19, 54]. This tensor can be further expanded in three directions u , v and w

$$-\overline{\tilde{U}'_i \tilde{U}'_j} = -\tau_{ij} = \begin{pmatrix} \overline{u'u'} & \overline{u'v'} & \overline{u'w'} \\ \overline{u'v'} & \overline{v'v'} & \overline{v'w'} \\ \overline{u'w'} & \overline{v'w'} & \overline{w'w'} \end{pmatrix}, \quad (2.9)$$

where the diagonal terms represent the normal stresses and the remaining terms the

shear stresses. Expanding the Reynolds stress tensor results in 9 unknowns, however, as this matrix is symmetric through the diagonal terms, only six unknowns are produced by Reynolds averaging. In the case of 3D flows, in addition to the six components of the Reynolds stress tensor, the pressure and the three velocity components are also solved, leading to a total of 10 unknowns needing to be solved. The additional unknowns cause an inequality between the available equations and unknowns, resulting in an unclosed problem. The problem can be closed by obtaining additional equations to solve unknowns. An equation for the conservation of the fluctuating fields [32] is obtained by subtracting the mean field given in Eq. (2.6) from the instantaneous field in Eq. (2.1), leading to

$$\frac{\partial \tilde{U}'_i}{\partial t} + \overline{\tilde{U}_j} \frac{\partial \tilde{U}'_i}{\partial x_j} = -\frac{1}{\rho} \frac{\partial \tilde{p}'}{\partial x_i} + \frac{\partial}{\partial x_j} \left(\vartheta \frac{\partial \tilde{U}'_i}{\partial x_j} + \tau_{ij} \right). \quad (2.10)$$

By multiplying Eq. (2.10) by a fluctuating property \tilde{U}'_j and averaging the product, the transport equation [32] for the Reynolds stress tensor components is obtained

$$\frac{\partial \tau_{ij}}{\partial t} + \overline{\tilde{U}_j} \frac{\partial \tau_{ij}}{\partial x_j} = P_{ij} + \Pi_{ij} + d_{ij} - \varepsilon_{ij}, \quad (2.11)$$

where influences by the fluctuating fields are given by the production term Π_{ij} , pressure-strain correlation Π_{ij} , diffusion d_{ij} , and the kinetic energy dissipation rate ε_{ij} , defined as

$$P_{ij} = -\tau_{ik} \frac{\partial \overline{\tilde{U}_j}}{\partial x_k} - \tau_{jk} \frac{\partial \overline{\tilde{U}_i}}{\partial x_k} = -\tau_{ik} (S_{kj} - \Omega_{kj}) - \tau_{jk} (S_{ik} - \Omega_{ik}), \quad (2.12)$$

$$\Pi_{ij} = \overline{\tilde{p}' \left(\frac{\partial \tilde{U}_i}{\partial x_j} + \frac{\partial \tilde{U}_j}{\partial x_i} \right)}, \quad (2.13)$$

$$d_{ij} = -\frac{\partial}{\partial x_k} \left(\frac{1}{2} \overline{\tilde{U}'_i \tilde{U}'_j \tilde{U}'_k} + \overline{\tilde{p}' (\tilde{U}'_i \delta_{jk} + \tilde{U}'_j \delta_{ik})} - \vartheta \frac{\partial \tau_{ij}}{\partial x_k} \right), \quad (2.14)$$

and

$$\varepsilon_{ij} = 2\vartheta \overline{\frac{\partial \tilde{U}'_i}{\partial x_k} \frac{\partial \tilde{U}'_j}{\partial x_k}}. \quad (2.15)$$

In Eq. (2.12), the velocity gradient tensors are decomposed into a symmetric part, S_{ij} , as given in Eq. (2.8), and an antisymmetric tensor, Ω_{ij} (see Eq. (2.16)), the vorticity tensor for the mean field.

$$\Omega_{ij} = \frac{1}{2} \left(\frac{\partial \tilde{U}_i}{\partial x_j} - \frac{\partial \tilde{U}_j}{\partial x_i} \right) \quad (2.16)$$

Another equation to solve the unknown variables can be found by assuming equal indices, $i = j$ for Eq. (2.10) and defining the turbulent kinetic energy [32] as

$$k \equiv \frac{1}{2} \tau_{ii} = \frac{1}{2} \overline{\tilde{U}_i \tilde{U}_i}, \quad (2.17)$$

where the turbulent kinetic energy equation is given by

$$\frac{Dk}{Dt} = \frac{\partial k}{\partial t} + \tilde{U}_j \frac{\partial k}{\partial x_j} = P_k + d - \varepsilon, \quad (2.18)$$

with the production term P_k , diffusion d and the turbulent kinetic energy dissipation rate ε given by

$$P_k = -\tau_{ik} \frac{\partial \tilde{U}_i}{\partial x_k}, \quad (2.19)$$

$$d = -\frac{\partial}{\partial x_k} \left(\frac{1}{2} \overline{\tilde{U}_i' \tilde{U}_j' \tilde{U}_k'} + \tilde{p}' \tilde{U}_k' - \vartheta \frac{\partial k}{\partial x_k} \right), \quad (2.20)$$

$$\varepsilon = \frac{1}{2} \varepsilon_{ii}. \quad (2.21)$$

With the additional equations given in Equations (2.11) and (2.18), more unknowns are generated, up to a point where the problem remains unclosed. This is caused by the non linearity of the NS equations. The unknowns can be approximated employing flow properties, resulting in sufficient equations to close the system, presenting the aim of turbulence modeling [57].

The unclosed problem can be approached with a simpler form of the Reynolds stress tensor. A simpler method of solving the RANS equations is provided in the form of the eddy viscosity concept by Boussinesq [3]. According to Boussinesq, the Reynolds stress tensor τ_{ij} can be replaced by the product of the velocity gradients and the turbulent viscosity μ_T . This assumption creates a proportionality between the Reynolds stress tensor and the mean strain-rate, defined as

$$\tau_{ij} = \frac{2}{3} \rho k \delta_{ij} - 2\mu_T S_{ij}, \quad (2.22)$$

where μ_T is the turbulent viscosity, making this variable now necessary to be modeled.

The turbulent (dynamic) viscosity μ_T , otherwise known as the eddy viscosity, is evaluated through turbulence models. Using the Boussinesq approach, four main categories of turbulence models were developed, out of which the first three are also known as eddy viscosity models [19, 57].

- Algebraic models: This category of models uses an algebraic expression to predict the turbulent viscosity μ_T , defined as $\nu_T \times \rho$. The velocity gradient is employed as a velocity scale along with a physical length as the turbulent length scale. Both variables are used to predict the eddy viscosity. Algebraic models are familiar as the most simple eddy viscosity models, also known as zero-equation models. Two well known zero-equation models are the Baldwin-Lomax and the Cebeci-Smith model.
- One-equation models: In this case, the partial differential equation (PDE) for the transport is solved for one turbulent quantity, such as the turbulent kinetic energy k . An algebraic expression is used to obtain a second turbulent quantity, in most cases the turbulent length scale. An established one-equation model is the Spalart-Allmaras model.
- Two-equation models: These models derive the PDE for the transport of two scalars, such as the turbulent kinetic energy k and turbulent kinetic energy dissipation rate ε . These two scalars will subsequently be used to predict the turbulent viscosity.
- Reynolds Stress Models (RSMs): For this category, from the Reynolds stress tensor τ_{ij} , is derived a transport equation. An additional transport equation will be necessary for determining the length scale of the turbulence, which would be in most cases an equation for the turbulent kinetic energy dissipation rate ε .

The four categories are organized in increasing order of ability to predict turbulence, model complexity and computation time. The first two categories are excessively used for designs in the aerospace industry. They are mostly employed for flows with attached wall-bounded flows. The simulations are used to verify rather the reliability of the design than predict the flow structures. This being the case, these models are unsuitable for predicting turbulent structures such as flow separation and recirculating flow, indicating only reliability for flows with a low Reynolds number [6, 4]. The two-equation models are simple to implement and function for fully turbulent flows. These models function well for predicting isotropic turbulence. This also signifies that these models are not suitable for predicting normal stresses, which results in difficulties in predicting irrotational strain and the flow for complex geometries with strong curvature. Nevertheless, improvements have been made on these models to simulate the

flow structures in complex geometries. Unlike the unimproved two-equation models, the RSMs can model the stresses in strong curvature geometries. However, aside from being difficult to execute, the computation time is also high [19].

2.1.2 Alternative approaches for modeling turbulent flow

Up to this point, a possible method of modeling turbulent flow is to divide the turbulent quantities into a mean and fluctuating part, avoiding the necessity of solving the instantaneous fluctuating quantities or smaller turbulent scales. This is done through the RANS approach. The RANS equations serve for modeling steady flow. For unsteady flow, exists the Unsteady Reynolds-averaged Navier-Stokes (URANS), by retaining the transient term $\partial\tilde{U}_i/\partial t$, in the URANS momentum equation (NS equation) [17]. However, an alternative method may be used to steer clear of simulating the smallest eddies. This method is called filtering, where the continuity and the momentum equation of the NS equations are integrated over space, producing time-dependent variables. The filtering method also produces additional terms in the filtered NS equations, causing an unclosed problem, with the unknowns to be modeled as in the case for the RANS equations. The filtering method is employed by the Large-eddy simulation (LES) approach. This approach, as its name suggests, models the large eddies within an unsteady flow, while filtering the smallest eddies. The LES approach requires a highly accurate spacial and temporal discretization. The 3D computational mesh needs a high resolution to be solved with small time steps. This approach does generate more reliable results, but at a high computational cost [40, 10, 11]. For resolving explicitly all turbulent scales, the Direct Numerical Simulation (DNS) approach can be used. As opposed to both the LES and RANS approaches, the flow is not modeled, but rather solved directly through non-empirical solutions of the flow. The DNS approach simulates unsteady flow with time-dependent variables. As this approach solves even the smallest eddies, the computational cost finds itself to be even higher than the one for the LES approach [14]. Additional restrictions to this numerical method are the Reynolds number and the geometry. The method is limited to low Reynolds numbers and simple geometries.

For this work, the most turbulent areas in the natural channel are needed, as the focus lies more on finding optimal locations for installing turbines by avoiding high turbulence areas. This signifies that only the highest turbulent areas need be simulated. The use of DNS method is discarded by its impairments for simple flows and its computational cost. As the LES approach still focuses on the smaller eddies and possesses also a high computational cost, the RANS approach is better suited to this research, as it will model the most turbulent areas, containing the highest turbulent kinetic energy k , within the channel with a low computation time.

2.2 STATE-OF-THE-ART ON OPEN-CHANNEL FLOW MODELING

Early works on the flow in a channel are found attempting to reproduce the flow in a natural channel in artificial channels within a controlled environment. The channels consisted mostly of a rectangular cross section [1]. The experimental studies are focused on the flow behavior by varying parameters, mostly the geometry by adding a floodplain [8], depicting a natural channel. The velocity components were measured employing a type of Laser Doppler Anemometer system [28], helping in visualizing 2D or 3D flow. The numerical studies [29, 42] were realized by using the RANS turbulence models with success, as the models were able to predict accurately the basic flow characteristics of turbulence, such as the Reynolds stresses and the kinetic energy.

Another focal point for both the numerical and experimental studies was the occurrence of secondary flow. To comprehend secondary currents, many experimental researches were carried out, such as Akihiro et al. (1991) [1] and Iehisa et al. (1986) [28], already listed previously. Important works regarding this subject are written by Knight and Shiono (1990) [37] and Knight and Shiono (1991) [49]. The research presented in both articles have been carried out in the Science and Engineering Council Flood Channel Facility (SERC-FCF). This facility was constructed specifically to research the hydraulic behavior of rivers with floodplains and was jointly founded by the Science and Engineering Council (SERC) and Research Council Ltd. (HR), where also the facility is located. Within this facility, many researches were able to be conducted, with varying geometries and boundary conditions, creating through the facility experiments a well known and well referenced database for turbulent channel flow. Both researches conducted by Knight and Shiono (1990) [37] and Knight and Shiono (1991) [49] were able to demonstrate the presence of secondary currents using experiments realized within the SERC-FCF. Knight and Shiono (1990) [37] focus on studying the turbulence in the shearing layers, in an attempt to understand turbulent flow structures in a compound open channel. Knight and Shiono (1991) [49] concentrates on the effects of turbulence caused by the channel bed, the turbulence lateral shear and secondary flow in the internal shear stress. All studied subjects produced precise results, of which the secondary flow is presented in Fig. 2.1.

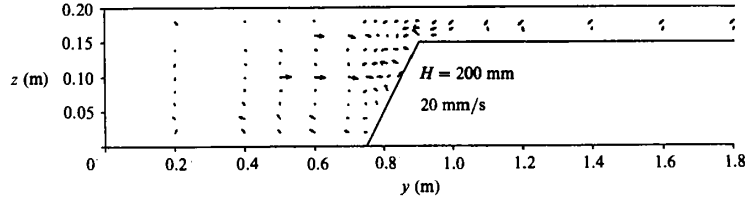


Figure 2.1 – Secondary flow vectors in the compound channel by [49], with a water level in the main channel H of 200 mm and $DR = 0.25$, the ratio between the water levels on the floodplain to main channel.

Continuing with numerical results, in Kamel et al. (2014) [34], results of a meandering compound open-channel are presented along with a straight open-channel. The flow structure, velocity distribution and mass transport process of both channels was studied employing the $k - \varepsilon$ model. The results were able to predict velocity profiles at different locations in the channel, among other complex flow structures in channels with bends and inclined river beds. The results show that the $k - \varepsilon$ model is suitable to be employed in cases of natural channel simulations. Two numerical researches realized with validation from experiments in the SERC-FCF are Jing et al. (2009) [30] and Jing et al. (2011) [31]. Both studies concentrate on the flow in compound meandering channels with different cross sections, indicating complicated flows affected various factors, such as centrifugal forces, pressure and bed shear stress. The turbulence model utilized is the RSM. In Jing et al. (2009) [30], the flow within a semi-natural cross sectional channel is simulated, while in Jing et al. (2011) [31], a channel with a trapezoidal cross section is employed for the simulations. Both studies present a good concordance between the experimental and numerical results, providing a suitable turbulence model predicting the flow in a natural open-channel. The work of Kang and Choi (2006) [35] even managed to demonstrate a different kind of secondary currents, as seen in Fig. 2.2, for an open rectangular channel employing the RSM. The inner secondary current appears in the junction created by the wall and the free surface, increasing the wall shear stress in that area. Thus, this type of secondary flow also affects the flow field and turbulent structures.

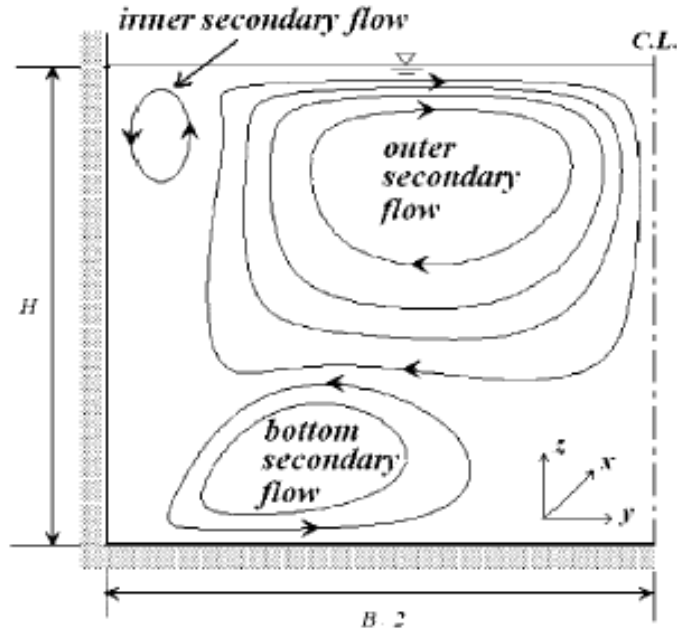


Figure 2.2 – Different types of secondary flow encountered in an open rectangular channel by Kang and Choi (2006) [35].

Whilst numerically reproducing the flow of a natural channel, it is only logical to simulate flows with real-life conditions encountered in a natural channel. Fischer-Antze et al. (2001) [22] studied a channel partially covered with vegetation. The vegetation was represented by vertical cylinders, with the $k - \varepsilon$ model employed for the simulations. Several cases were studied by varying the velocity and the vegetation density. Comparisons between the numerical and experimental results show a good agreement. In an attempt to overcome the ability of the $k - \varepsilon$ model only simulating isotropic turbulence, a variation of this model, including a non linear $k - \varepsilon$ model for predicting turbulence anisotropy was employed in Zhang et al. (2010) [58]. The studied channel also contains vegetation, creating a complex flow, as the vegetation would create more flow variations by acting as an obstacle. The resistance by the vegetation in the flow is treated by the drag force approach, applying an additional drag force sink term to the momentum and $k - \varepsilon$ model equations. The numerical results were eventually compared to experimental data, showing a successful prediction by modifying the $k - \varepsilon$ model.

In the case of simulating a natural channel flow, it becomes important to choose the correct model for simulating a difficult to predict turbulence structure: the secondary flow. The literature shows three types of RANS models dominating in the researches. The RSMs have been employed consistently with success, which makes this type of model necessary to include for the simulations in this work. The $k - \varepsilon$ model is a stable and well used model, demonstrating, despite its limited capabilities discussed during

chapter 2.1.1, promising results in simulating complex flow fields. Modifying this model heightens the chances of accurately predicting the flow in complex geometries. All three model types managed to simulate secondary flow, which makes them an excellent choice to use for the simulations of the natural channel in present research.

2.3 DESCRIPTION OF THE SELECTED TURBULENCE MODELS

2.3.1 The $k - \varepsilon$ model

The description of the $k - \varepsilon$ model is initiated with the definition of the turbulent length scale L_μ as

$$L_\mu = \frac{k^{3/2}}{\varepsilon}. \quad (2.23)$$

Rewriting Eq. (2.22) in terms of the turbulent kinematic viscosity ϑ_T results in

$$\tau_{ij} = \frac{2}{3}k\delta_{ij} - 2\vartheta_T S_{ij}, \quad (2.24)$$

with

$$\vartheta_T = C_\mu \frac{k^2}{\varepsilon}. \quad (2.25)$$

For this model, closing Eq. (2.18) necessitates an additional equation for the kinetic energy dissipation rate ε , resulting in the characteristic two transport equations [32] for the $k - \varepsilon$ below:

$$\frac{Dk}{Dt} = \frac{\partial k}{\partial t} + \tilde{U}_j \frac{\partial k}{\partial x_j} = \frac{\partial}{\partial x_j} \left(\left(\vartheta + \frac{\vartheta_T}{\sigma_k} \right) \frac{\partial k}{\partial x_j} \right) + P_k - \varepsilon, \quad (2.26)$$

and

$$\frac{D\varepsilon}{Dt} = \frac{\partial \varepsilon}{\partial t} + \tilde{U}_j \frac{\partial \varepsilon}{\partial x_j} = \frac{\partial}{\partial x_j} \left(\left(\vartheta + \frac{\vartheta_T}{\sigma_\varepsilon} \right) \frac{\partial \varepsilon}{\partial x_j} \right) + C_{\varepsilon 1} P_k \frac{\varepsilon}{k} - C_{\varepsilon 2} \frac{\varepsilon^2}{k}. \quad (2.27)$$

Considering the Boussinesq hypothesis as given in Eq. (2.24), the turbulence production term P_k is modeled as

$$P_k = 2\vartheta_T S_{ij} S_{ij}, \quad (2.28)$$

of which the constants, determined from experimental data [57], have the following values

$$C_\mu = 0.09, C_{\varepsilon 1} = 1.44, C_{\varepsilon 2} = 1.92, \sigma_k = 1.0, \sigma_\varepsilon = 1.3. \quad (2.29)$$

2.3.2 Modifying the $k - \varepsilon$ model: RNG $k - \varepsilon$ model

As mentioned earlier in chapter 2.1.1, modifications were made to the standard $k - \varepsilon$ model to allow for a better prediction of a complex flow. The RNG model variation in particular, employs a statistical method known as the Renormalization Group method. As a result, the Renormalization Group (RNG) $k - \varepsilon$ model provides more accuracy for swirling and rapidly strained flows [5]. Another difference lies in the near wall treatment. The $k - \varepsilon$ model requires *ad hoc* wall damping functions, whereas with the RNG $k - \varepsilon$ model, a direct integration to the boundary can be carried out without *ad hoc* wall damping functions [51]. Noteworthy is the fact that the model functions for high Reynolds numbers.

The turbulent kinematic viscosity ϑ_T , in this case assumed as the eddy viscosity, has the same definition as in Eq. (2.25). The turbulent kinetic energy is the same as given in Eq. (2.17), whereas the constant C_μ is assumed to be 0.085 and the turbulent kinetic energy dissipation rate ε is given by

$$\varepsilon = \vartheta \left(\overline{\frac{\partial \tilde{U}'_i}{\partial x_j} \frac{\partial \tilde{U}'_i}{\partial x_j}} \right). \quad (2.30)$$

The transport equations for k and the ε are defined as

$$\frac{Dk}{Dt} = \frac{\partial k}{\partial t} + \overline{\tilde{U}_i} \frac{\partial k}{\partial x_i} = \frac{\partial}{\partial x_i} \left(\left(\frac{\vartheta_T}{\sigma_k} \frac{\partial k}{\partial x_i} \right) \right) + P_k - \varepsilon, \quad (2.31)$$

and

$$\frac{D\varepsilon}{Dt} = \frac{\partial \varepsilon}{\partial t} + \overline{\tilde{U}_i} \frac{\partial \varepsilon}{\partial x_i} = \frac{\partial}{\partial x_i} \left(\left(\frac{\vartheta_T}{\sigma_\varepsilon} \frac{\partial \varepsilon}{\partial x_i} \right) \right) + C_{\varepsilon 1} P_k \frac{\varepsilon}{k} - C_{\varepsilon 2} \frac{\varepsilon^2}{k}. \quad (2.32)$$

The turbulence production term remains the same as given in Eq. (2.28). However, changes can be noted in the model constant values and the definition of $C_{\varepsilon 1}$:

$$C_{\varepsilon 2} = 1.68, \sigma_k = 0.7179, \sigma_\varepsilon = 0.7179, \quad (2.33)$$

and $C_{\varepsilon 1}$ being equal to

$$C_{\varepsilon 1} = 1.42 - \frac{\eta(1 - (\eta/\eta_0))}{1 + \beta\eta^3}, \quad (2.34)$$

where

$$\eta = S \frac{k}{\varepsilon}, \quad (2.35)$$

with the strain-rate tensor S defined as

$$S \equiv \sqrt{2S_{ij}S_{ij}}. \quad (2.36)$$

The remaining constants assume the following values

$$\eta_0 = 4.38, \beta = 0.015. \quad (2.37)$$

2.3.3 The RSM

Through RSMs, the Reynolds stress is determined directly by solving the Reynolds stress transport equations. As opposed to this model, the eddy viscosity models employ a linear relation between the Reynolds stress τ_{ij} and the mean strain-rate S_{ij} , resulting in inaccuracy whilst predicting complex flows with rotation and curvature. While the Boussinesq approach models isotropic turbulence, the RSMs allow for modeling anisotropic turbulence. The RSMs exist generally out of five constitutive equations, with two of the equations related to the differences between the turbulent normal stresses and the remaining three to deviating components [32, 59].

Taking into consideration the definition of the Reynolds stress tensor τ_{ij} as $\overline{\tilde{U}'_i \tilde{U}'_j}$, the transport equation [32] for τ_{ij} results in

$$\overline{\tilde{U}'_k} \frac{\partial \tau_{ij}}{\partial x_k} = - \left(\tau_{ik} \frac{\overline{\tilde{U}'_j}}{x_k} + \tau_{jk} \frac{\overline{\tilde{U}'_i}}{x_k} \right) + d_{ij} - \varepsilon_{ij} + \Pi_{ij}. \quad (2.38)$$

Comparing the equation above to Eq. (2.11) shows the transient term missing and the production term expressed in a more explicit form. This leads to the production terms to be modeled analogically as the convective terms in other transport equations.

The remaining terms on the right-hand side of Eq. (2.38), are defined by their formative characteristics, with the three remaining terms separately solved by closure models. As there are many models solving these terms, the focus will be kept on the most accurate models presented by Choi and Kang (2002) [13]. According to Choi and Kang (2002) [13], the diffusion tensor d_{ij} and the turbulent pressure-strain term Π_{ij} , are predicted the most accurately, respectively by Mellor and Herring (1973) [41] and Speziale et al. (1991) [52], as they generate results closest to the experimental results in a open-channel flow. For the turbulent kinetic energy dissipation rate term is chosen the model proposed by Rotta (1951) [45]. As Kang and Choi (2006) [35] produce good results in predicting complex flows, even demonstrating an alternative type of secondary flow, the RSM model presented in their work, the Speziale, Sarkar and Gatski (SSG) RSM will be combined with the previously mentioned accurate models to solve the last three terms on the right-hand side of Eq. (2.38).

The diffusion tensor is thus defined as

$$d_{ij} = C_s \frac{\partial}{\partial x_k} \left(\frac{k^2}{\varepsilon} \left(\frac{\partial \tau_{ij}}{\partial x_k} + \frac{\partial \tau_{ik}}{\partial x_j} + \frac{\partial \tau_{jk}}{\partial x_i} \right) \right). \quad (2.39)$$

For this tensor the constant C_s assumes a value of 0.22/3 and the turbulent kinetic energy k is defined as

$$k \equiv \tau_{ii}/2. \quad (2.40)$$

The turbulent energy dissipation rate of the Reynolds stress transport equation, ε_{ij} is modeled with

$$\varepsilon_{ij} = \frac{2}{3} \varepsilon \delta_{ij}. \quad (2.41)$$

The turbulent kinetic energy dissipation transport equation becomes

$$\overline{U_j} \frac{\partial \varepsilon}{\partial x_j} = \frac{\partial}{\partial x_k} \left(C_\varepsilon \frac{k}{\varepsilon} \tau_{kl} \frac{\partial \varepsilon}{\partial x_l} \right) + \frac{\varepsilon}{k} \left(C_{\varepsilon 1} P_k - C_{\varepsilon 2} \varepsilon \right), \quad (2.42)$$

in which P_k is the turbulent kinetic energy production and model constants take on the values

$$C_\varepsilon = 0.18, C_{\varepsilon 1} = 1.45, C_{\varepsilon 2} = 1.90. \quad (2.43)$$

The pressure-strain term Π_{ij} , serving for redistributing the turbulent kinetic energy among the Reynolds stresses, is presented as

$$\begin{aligned}\Pi_{ij} = & \alpha_0 \varepsilon b_{ij} + \alpha_1 \varepsilon (b_{ik} b_{jk} - 1/3 b_{mn} b_{nm} \delta_{ij}) + \alpha_2 k S_{ij} + \alpha_3 P_k b_{ij} \\ & + \alpha_4 k (b_{ik} S_{jk} + b_{jk} S_{ik} - 2/3 b_{kl} S_{lk} \delta_{ij}) + \alpha_5 k (b_{ik} W_{jk} + b_{jk} W_{ik}).\end{aligned}\quad (2.44)$$

Equation (2.44) presents a yet unknown variable the anisotropy tensor b_{ij} defined as

$$b_{ij} = \frac{\tau_{ij}}{2k} - \frac{1}{3} \delta_{ij}.\quad (2.45)$$

In Eq. (2.44), the mean strain-rate tensor S_{ij} contains the same definition as in Eq. (2.8), while the rotation tensor W_{ij} is presented as

$$W_{ij} = \frac{1}{2} \left(\frac{\partial \tilde{U}_i}{\partial x_j} - \frac{\partial \tilde{U}_j}{\partial x_i} \right).\quad (2.46)$$

The empirical model constants as determined by Speziale et al. (1991) [52] are

$$\alpha_0 = -3.4, \alpha_1 = 4.2, \alpha_3 = -1.8, \alpha_4 = 1.25, \alpha_5 = 0.4,\quad (2.47)$$

with α_2 solved by

$$\alpha_2 = 0.8 - (1.3(b_{nm} b_{mn})^{1/2}).\quad (2.48)$$

3 METHODOLOGY

"If we knew what we were doing it would not be called research, would it?"

-Albert Einstein, German theoretical physicist

3.1 NUMERICAL METHOD VALIDATION

The first phase of the research is carried out by employing an artificial channel that can be modeled using CFD tools.

Therefore, the artificial channel, a benchmark channel, was chosen based on the following criteria:

- In this specific case, the benchmark channel is chosen by similarities in its appearance to a natural channel: open-channels with a varying cross section and floodplain (compound channel cross section). The channel would also be required to contain bends, indicating the existence of secondary currents;
- In order to numerically replicate the channel, an extensive geometry description is required;
- Distinctly defined boundary conditions under a controlled environment, such as a laboratory, in order to reproduce the flow in the channel;
- Available experimental data in the form of either average velocity, turbulence intensity, turbulent kinetic energy, surface velocity or secondary flow in different sections of the channel.

As multiple prerequisites are required for the ideal benchmark channel, it is only to be expected that all requirements will not be necessarily met in the same work. Complying with all conditions described above, model FCF-B23, as reported by both de Lima da Silveira e Lorena (1992) [39] and Jing et al. (2011) [31] is found. This model contains an artificial meandering channel with a trapezoidal cross section and a floodplain. The channel is located in the SERC-FCF. The experimental setup of the channel, signifying extensive geometry information, is designed by de Lima da Silveira e Lorena (1992) [39]. The meandering main channel and floodplain geometry were based on studies on river morphology, following a shape similar to rivers found in the

nature. The design also accounts for sufficient main channel length and width for the development of the flow, and shear layers in the floodplain. Therefore, after trials and validation, the design of the artificial channel, as visualized in Fig. 3.1, is composed of:

- A total length and width of respectively 49 and 10 *m*;
- A cross over angle of 60°;
- The main channel in the model is comprised of 4 meander wavelengths, with each meander wavelength equal to a length of 12 *m*;
- Bends in the form of half-moon, with a mean radius of curvature equal to 2.743 *m*, each followed by a straight-cross over length of each 2.5 *m*;
- Top width of the main channel equal to 1.2 *m*;
- Sinuosity of 1.374;
- A bankfull (*h*) depth of 150 *mm*;
- Double amplitude of the meander equal to 4.91 *m*;
- Meander belt width equal to 6.11 *m*;
- Half-width of floodplain beyond the meander belt equivalent to 1.95 *m*;
- The channel cross section consists out of a 45 ° trapezoidal slope (created by the side walls inclined 1:1), with the bottom width being 0.9 *m* and the aforementioned bankfull depth and top width of the main channel.

As the work presented by de Lima da Silveira e Lorena (1992) [39] is purely experimental, additional references in the form of Jing et al. (2011) [31] are required to numerically replicate the flow in the benchmark channel. Jing et al. (2011) [31] have simulated four cases in their work, comprising of one inbank flow and three overbank flow cases, of which they study velocity profiles, velocity streamlines and secondary currents for 8 regions as presented in Fig. 3.2. The numerical results are compared to experimental results also measured by Jing et al. (2011) [31] in the previously presented 60 ° meandering channel under a discharge capacity of 1.1 *m*³/*s*. The simulated domain consists out of only two wavelengths, rendering a computational model with a length of 26 *m* and width of 10 *m* (Fig. 3.3). The two wavelengths result in a meandering main channel with five bends and five straight cross over lengths. The bends maintain the same mean radius of curvature as designed by de Lima da Silveira e Lorena (1992) [39]. The central angle of a bend is 120 °, except in the case of the first and fifth bend, where the angle assumes a value of 60 °. As the modeled channel length differs from

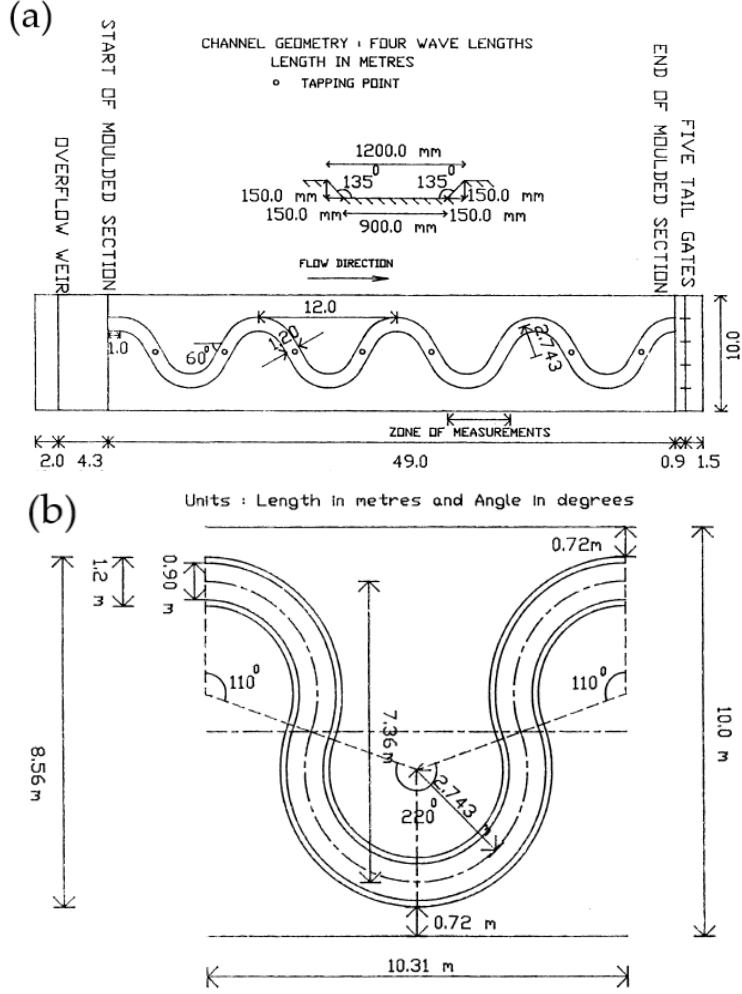


Figure 3.1 – Benchmark channel design (a) plan view as constructed within the SERC-FCF with multiple bends to research secondary currents and a 45° compound trapezoidal (varying) cross section, presenting a likeness to morphology encountered in natural channels and (b) detailed geometry for straightforward adapting into the chosen designing software, derived from de Lima da Silveira e Lorena (1992) [39].

the artificial channel in the facility, the two wavelength channel is extended with a 2 m straight channel to allow for flow development and avoid deviations between numerical and experimental results. In present work, the focus lies on replicating the flow generated under the conditions presented in Tab. 3.1 for case 3, section 3, which is located at the peak of fourth curve. The k_{in} (turbulence kinetic energy) and ε_{in} (Turbulent kinetic energy dissipation rate) at the inlet, evaluated by Choi and Kang (2008) [12], Guo et al. (2009) [24] and Jing et al. (2009) [30], are calculated respectively by:

$$k_{in} = \frac{3}{2}(IU_{in})^2, \quad (3.1)$$

$$\varepsilon_{in} = C_{\mu}^{3/4} \frac{k_{in}^{3/2}}{0.1R}, \quad (3.2)$$

where I is the turbulence intensity, assumed to be 10% and R is the (hydraulic) radius. The inlet in case 3 is modeled with a inlet velocity U_{in} , determined by $U_{in} = Q/A$, in which Q is the volumetric flow rate and A the cross sectional area of the inlet. The relative water depth DR is defined as the ratio between water depth over the flood plain (h) and the water depth in the main channel (H).

DR	Q (m^3/s)	H (m)	U_{in} (m/s)	k_{in} (m^2/s^2)	ε_{in} (m^2/s^3)
0.25	0.2480	0.2	0.378	2.14×10^{-3}	8.14×10^{-4}

Table 3.1 – Case 3 inlet values by Jing et al. (2011) [31].

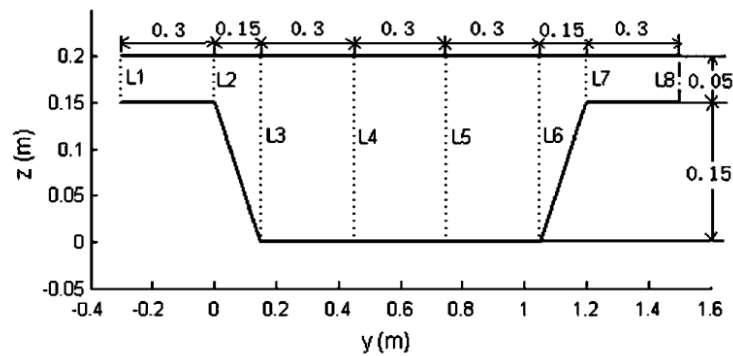


Figure 3.2 – Benchmark channel cross section of 45 ° of the meandering 60 ° channel designed by de Lima da Silveira e Lorena (1992) [39] with the eight studied regions per cross section as reported by Jing et al. (2011) [31].

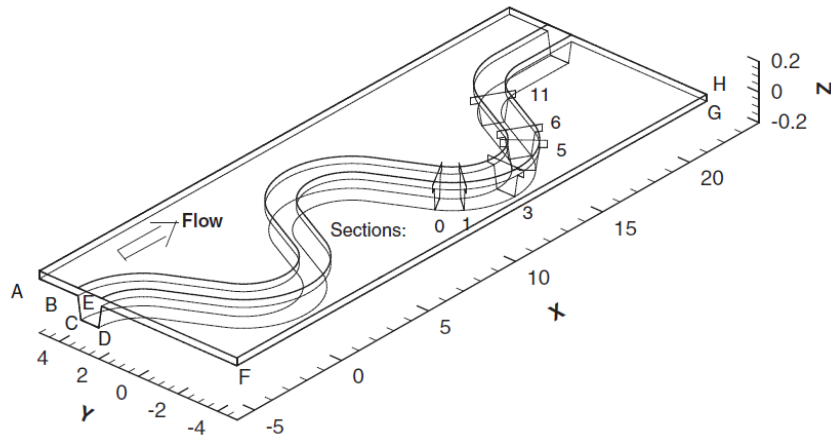


Figure 3.3 – Channel domain with the studied sections as simulated by Jing et al. (2011) [31].

Present work models the benchmark channel according to de Lima da Silveira e Lorena (1992) [39] in Ansys SpaceClaim, subsequently imported into Ansys Meshing to generate a computational mesh using tetrahedral elements, to counter a poor quality mesh. The channel is modeled with an inlet, outlet, channel walls, channel bed and a

free surface. To define the flow near the walls, the inflation layer option is activated for 15 layers, with a first layer size of 3.8×10^{-4} m.

The inlet boundary has been modeled with the same U_{in} as in Tab. 3.1. The outlet has been defined as a static pressure equal to zero, along with a pressure profile blend of 0.05. The walls are modeled as smooth walls with a non-slip condition, while the free surface boundary is set as a slip wall. The wall functions remain unchanged as the standard wall function setting per model (scalable wall function). The simulations are carried out using Ansys CFX software.

The results will be focused on regions L3-L5, located in the main channel, as the knowledge of the flow structures in said regions are of importance, as in the case of installing turbines, they would be installed in the deeper, thus the main channel region.

Prior to the simulations generating results to be compared to both types of results produced by Jing et al. (2011) [31], the mesh grid is analyzed using the $k - \varepsilon$ model while retaining the described simulation setup. The initial mesh will be successively refined three times through varying the linear global element order, increasing the number of nodes. The velocity U and turbulence intensity I profiles, two important variables for the proposed numerical method in this work (used for turbine siting), for L3-L5 are studied, after which selected points within these profiles will be plotted against the nodes. The mesh is considered independable of the solution, when the plotted variable no longer varies with the increasing mesh size.

The mesh grid analysis is followed up by a turbulence assessment study, employing three turbulence models: a RSM, the $k - \varepsilon$ model (see chapter 2.3.1) and the RNG $k - \varepsilon$ model (see chapter 2.3.2). The chosen RSM is the SSG RSM (see chapter 2.3.3), depicted henceforth as simply RSM. The models are chosen after the state-of-the-art review in chapter 2.2 displayed these type of models (RSM, the $k - \varepsilon$ model and a modification of the $k - \varepsilon$ model) as the most likely to generate consistent and reliable results on controlled environment open-channel flow. The remaining boundaries are modeled as in the original setup. The results obtained from the three models will be plotted along the numerical and experimental results generated by Jing et al. (2011) [31]. The longitudinal u and transverse v velocities comparison results are expected to demonstrate the model displaying the most consistent and reliable results as compared to the reference data, simultaneously proving the proposed methodology capable of simulating the flow within the benchmark channel. The most proficient model will be used further to compare the velocity fields and also procure secondary currents within the cross sectional plane known as section 3 case 3.

3.2 NUMERICAL SIMULATION OF THE SEFAC CHANNEL

After determining the turbulence model most likely to simulate trustworthy results for an artificial channel within a controlled environment, the endeavor is made to employ this model for simulating the Sefac channel. The collected bathymetry by the field data collection team within the Lambari project, of which the collecting procedure is explained in appendix A, is turned into a computational mesh employing the Ansys SpaceClaim software. The channel is modeled with an inlet, outlet, a free surface plane and channel walls (including the channel bed). The free surface plane is assumed as a zero water level. The mesh is generated in Ansys Meshing. Once again, to counter a poor mesh quality as the result of an irregular geometry, tetrahedral elements are used to produce the mesh, as shown in Fig. 3.4.

The inlet has been modeled with a initial measured flow rate of $91 \text{ m}^3/s$. Within Ansys, this flow rate is converted into a mass flow rate \dot{m} , 91000 kg/s . The remaining boundary conditions remain unchanged compared to those used during the method validation. Before initiating the simulations, a mesh grid analysis is carried out to configure the mesh. This study follows the same process as described in the benchmark mesh grid analysis, employing the boundary conditions described as above and the most trustworthy and consistent turbulence model from the turbulence model assessment. All simulations are realized in Ansys CFX. During all cases, three monitoring points will be assigned to monitor the solution, also shown in Fig. 3.4. The first is located in the depression area, while the remaining points are spread halfway along the channel and near the end of the channel mesh domain. The coordinates of the three monitoring points **p1**, **p2** and **p3** (in m) used for monitoring the solution are listed below:

- **p1**: $x= 405.571, y= -101.721, z=-10.9537$
- **p2**: $x= 326.91, y= -83.3865, z=-0.65613$
- **p3**: $x= 163.945, y= -111.418, z=-1.2$

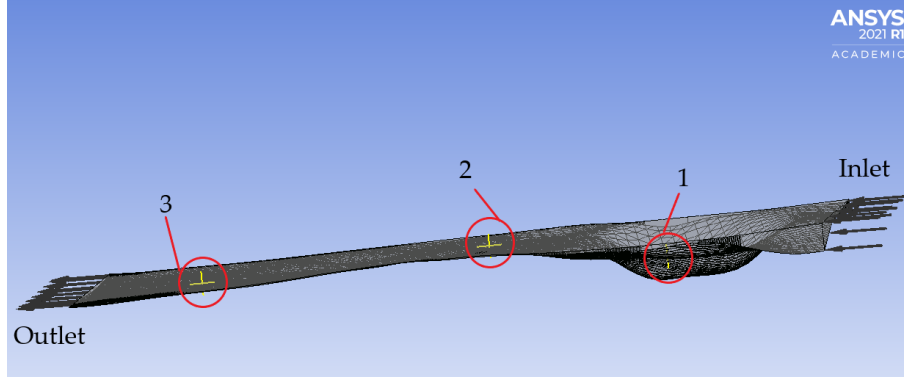


Figure 3.4 – Monitoring points location in the Sefac channel mesh, with the first point nearest to the inlet.

3.2.1 Installation areas for the hydrokinetic turbines

Studying the simulated velocity contours, areas with the highest velocities are chosen. Subsequently, cross sectional planes are constructed along these areas to study the depths for their suitability for installing turbines. To obtain a better understanding of the occurring velocities, per cross section four areas (P1-P4) are chosen to retrieve velocity profile data. As mentioned earlier, one of the distinguishing factors in this research will be to not only consider the velocities and depths, but also the turbulence levels in the chosen areas. To this end, the turbulence intensity per profile is studied, along with the occurrence of secondary flow in the sections. The turbulence intensity is calculated by rewriting Eq. (3.1):

$$I = \frac{\sqrt{\left(\frac{2}{3}k\right)}}{U_{sim}} \quad (3.3)$$

The selection of ideal planes to install turbines is made up by a high velocity, deep channel bed area, low turbulence intensity level and no or low secondary flow.

3.2.2 Turbine siting and the annual potential power generation of the turbine farm

As one of the objectives of this methodology is to assess hydrokinetic energy potentials for a natural channel annually, such methodology must be capable of predicting the hydrokinetic energy for various flow rates. To this end, flow rate data per year for the years 2015-2019 are analysed. Out of the all available data, only the years 2018 and 2019 present daily measured flow rates. Out of the two indicated years, the year 2018 contains extremely fluctuating data, with a smallest flow rate of $31.51 \text{ m}^3/\text{s}$ and largest flow rate measured at $313.76 \text{ m}^3/\text{s}$. It is exactly this type of data that can most

likely demonstrate the developed methodology to be capable of being applied to any flow rate. Figure 3.5 shows the flow rates divided in general into two categories: in the first approximately 200 days of the year occur low flow rates, whereas the remainder of the year shows a high flow rate period. For calculating the annual power generation capacity, the most frequent occurring flow rates along with their duration in 2018 must be determined. Using the flow rate data from 2018, a 20-day moving average shows two intervals throughout the year, emphasized with black circles in Fig. 3.5, where the graph takes on a steady behavior, meaning the flow rate varies little over that period.

These two intervals show two frequent occurring flow rates within the data: $51.39 \text{ m}^3/\text{s}$ and $158.72 \text{ m}^3/\text{s}$, lasting respectively for 131 and 165 days.

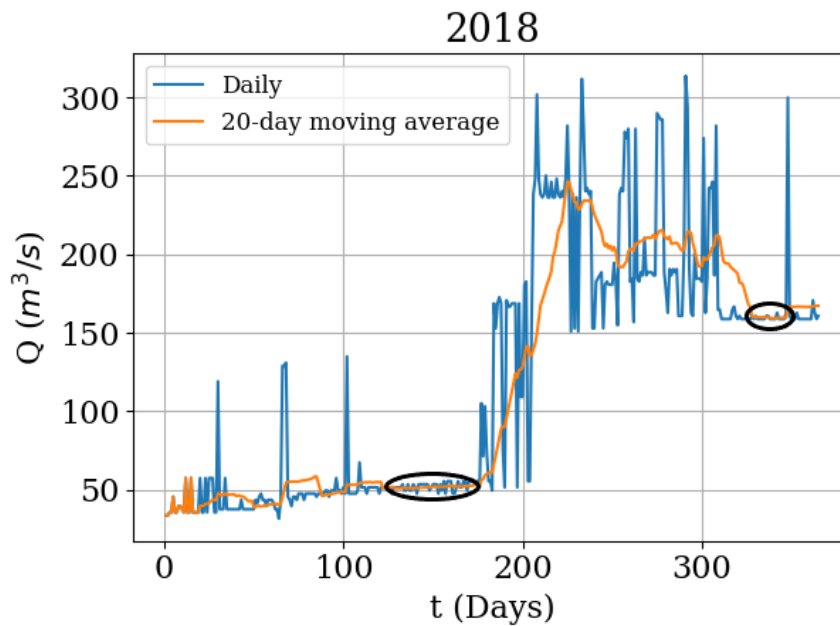


Figure 3.5 – Daily measured and 20-day moving average flow rates with the two most frequent occurring flow rates in the Sefac channel during 2018.

The two obtained flow rates will be used as the inlet boundary condition after being converted to the mass flow rate \dot{m} . The mesh generation process, the remaining boundary conditions and the turbulence model remain the same as described for the general simulation process discussed in section 3.2. The turbines will be sited considering the changing velocity values and profiles and turbulence levels. Once the turbine layout is finalized, the potential generated power, also known as $P_{converted}$ in appendix B, per flow rate is calculated through an alternative method, given by

$$P_{converted} = \frac{1}{2} C_p A \rho U_{sim}^3, \quad (3.4)$$

where

$$A = \frac{1}{4}\pi D^2. \quad (3.5)$$

The turbine efficiency in a similar flow situation as determined in appendix B is taken into consideration. Finally, the potential generated annual power is estimated.

4 RESULTS AND DISCUSSION

"When I meet God, I am going to ask him two questions: Why relativity? And why turbulence? I really believe he will have an answer for the first."

-Werner Heisenberg, German theoretical physicist

4.1 BENCHMARK SIMULATIONS

4.1.1 Mesh grid sensitivity analysis

The sensitivity analysis is carried out by studying how the velocity U and the turbulence intensity I profiles vary with increasing mesh size. The analysis will contain the results of results of four meshes, with their sizes given in Tab. 4.1. Data for three regions, L3, L4 and L5, in the main channel have been extracted for perusal.

Table 4.1 – Mesh sizes for the benchmark mesh grid analysis.

Mesh	Nodes
1	899328
2	1665067
3	2363097
4	3053323

The velocity profiles in Fig. 4.1 show the velocity increasing gradually up to approximately a depth of ≈ 0.17 m, after which a sharper increase is noted. L3 and L4 show initially differences between the first two meshes, only to diminish in the finest meshes. For L5, only the first mesh profile diverges from the rest. Based on only the velocity profiles, the two finest meshes demonstrate the velocity to be independent of the mesh grid. However, in this research, the turbulent kinetic energy k is also an important factor for ultimately determining the hydrokinetic potential in a natural channel, making it paramount to also ascertain whether this variable is reliant on the mesh grid. Figure 4.2 shows how the turbulent kinetic energy k varies, in the form of the turbulence intensity I , with an increasing mesh size. As also observed in Fig. 4.1, the last two meshes for L3 seem to demonstrate a converging solution. However, for L4 and L5, the two final meshes still show variations. As no clear judgement regarding the mesh grid sensitivity can be made based on the turbulence intensity profiles, values at certain points of visible divergence of the profiles will be studied with increasing mesh

size in Fig. 4.3. As an additional confirmation, the same will be repeated for the velocity variable in Fig. 4.4. The velocity values plotted against the mesh nodes already show a stabilized behavior for the two finest meshes, indicating that the solution for the velocity has converged for all three regions. The same is noticed for the turbulence intensity values, where the last two meshes show a close to stable behavior, with the highest difference between all values recorded at 9% for L5.

Table 4.2 presents the approximated processing time for each simulation carried out during this study. As expected, with an increasing mesh size, the processing time increases significantly. However, the computational cost remains low, as the highest processing time is just over 1 hour. The simulations were realized using a Supermicro server with as main processor the Intel (R) CPU E5-2643 v2 @ (containing 2 processors), a Random-access Memory (RAM) memory of 64 GB and an operational system of 64 bits. The simulations were carried out using parallel processing.

Table 4.2 – Processing time for the simulations employing different benchmark channel mesh sizes.

Mesh size	Processing time
899328	≈ 16 min
1665067	≈ 45 min
2363097	≈ 58 min
3053323	≈ 1 hour and 14 min

Taking into consideration the low computational cost and the results presented for the mesh grid sensitivity analysis, especially the close to stable behavior of the turbulence intensity for L4 and L5, the mesh used for the simulations should have a number of nodes equal to or greater than the finest mesh.

4.1.2 Turbulence model assessment

Following the mesh grid analysis, the mesh employed for the simulations contains 3053323 nodes and 6973984 elements, with a linear global element size of 0.05 m and an average y^+ of 7.28.

The results of the $k - \varepsilon$, the RNG $k - \varepsilon$ model and the RSM are compared in this section to the numerical and experimental data provided by Jing et al. (2011) [31]. Once again, three regions located in the main channel, L3, L4 and L5 are considered for the comparison. For the model assessment, the following parameters are considered:

- The longitudinal velocity u (Fig. 4.5);
- The transverse velocity v (Fig. 4.6).

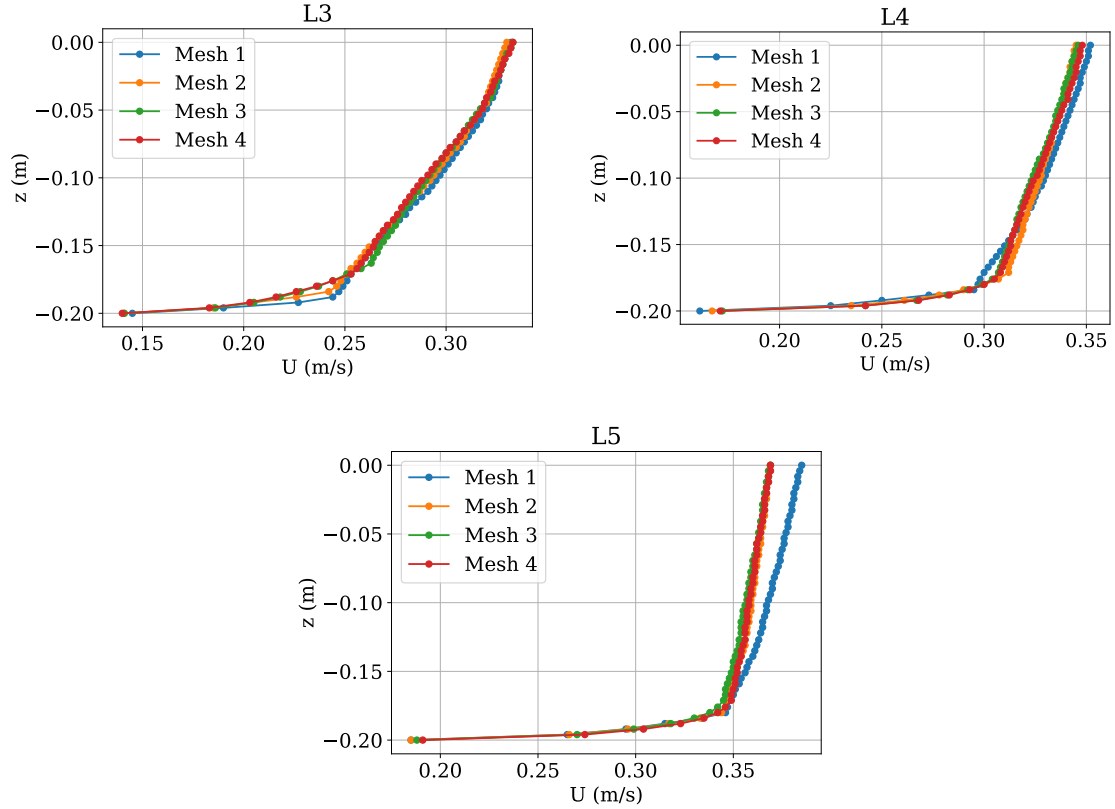


Figure 4.1 – Benchmark mesh grid analysis results for the turbulence intensity U for regions L3, L4 and L5, obtained by the $k - \varepsilon$ model.

The longitudinal velocity profiles vary increasingly from the experimental and numerical results by Jing et al. (2011) [31] in the direction of the water surface. The divergence is the greatest for regions L4 and L5. This may be caused by the location of these regions. Both regions find themselves in the middle of the main channel, where interactions between the floodplain and main channel are the strongest, with the floodplain flow containing a significantly lower velocity than the main channel. The longitudinal profiles only show noticeable differences compared to the reference data nearing the floodplain, increasing the likelihood of this assumption. This also explains why there is no great divergence between all longitudinal profiles, numerical and measured, for region L3, as this is located near the wall. The surface velocity would be influenced by both the low floodplain flow velocity and the higher main channel velocity, thus causing the variations between all numerical results and the experimental results. Taking this supposition into consideration would also explain why there are no significant differences between the transverse v velocity profiles. These profiles represent the flow velocity in the plane itself, not being the primary flow velocity as presented by the longitudinal velocity profiles. For the plane velocity, the boundary layer effects caused by the flow against the channel bed and walls are demonstrated clearly by L3, with the simulated models showing different results for this region. L4

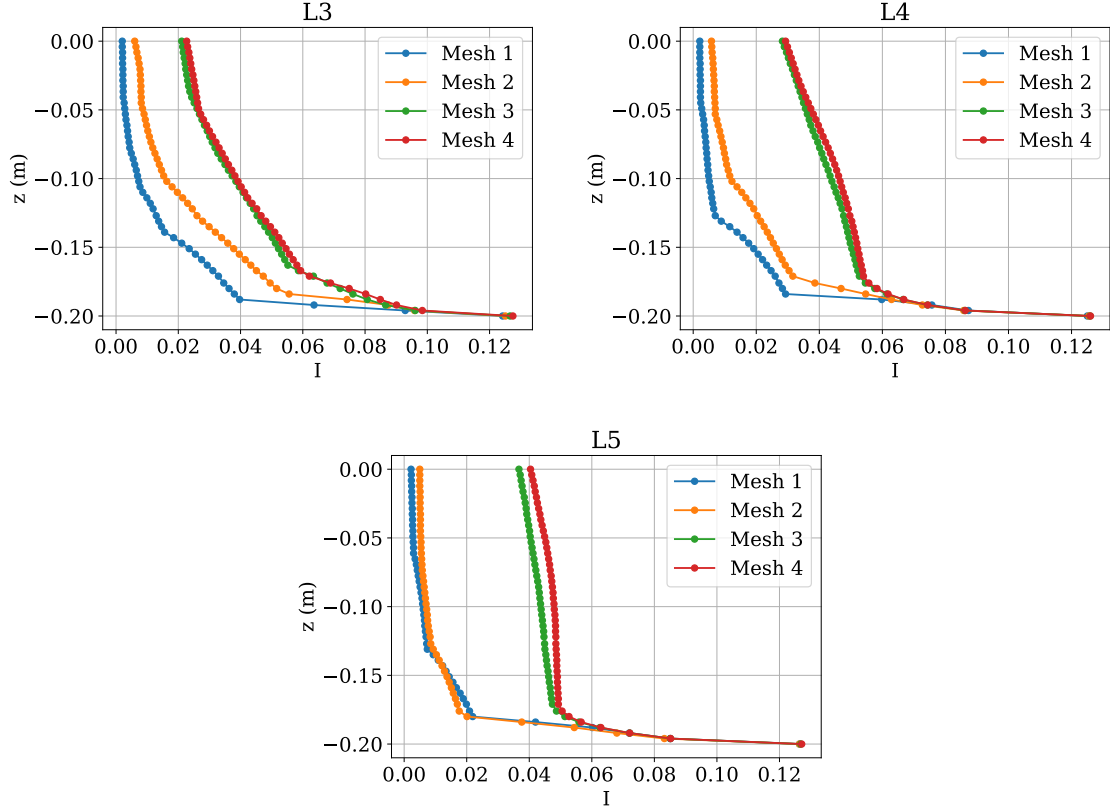


Figure 4.2 – Benchmark mesh grid analysis results for the turbulence intensity I for regions L3, L4 and L5, obtained by the $k - \varepsilon$ model.

and L5 also show effects of the boundary layer, however only near the channel bed.

Studying all six profiles leads to two important considerations in choosing the best performing turbulence model:

- The ability to produce results closest and consistent to the reference data while approximating the water surface in the main channel (L4 and L5);
- The ability to adequately predict the flow near the wall, regardless of the boundary layer effects (L3).

Based on these observations, two models can be considered as likely candidates for the best performing turbulence model. The $k - \varepsilon$ model performs better in the lower depths of the channel for both the longitudinal and the transverse profiles, suggesting that this model may be able to cope with boundary layer effects. Nevertheless, this model demonstrates the weakest performance for all profiles nearing the water surface. These observations are in accordance to the theory discussed in chapter 2.1.1. The $k - \varepsilon$ is known to demonstrate a good performance near the walls with boundary layer effects, as the turbulence in that area is isotropic, which the $k - \varepsilon$ model is widely used and known for. This model shows also poor results in simulating the

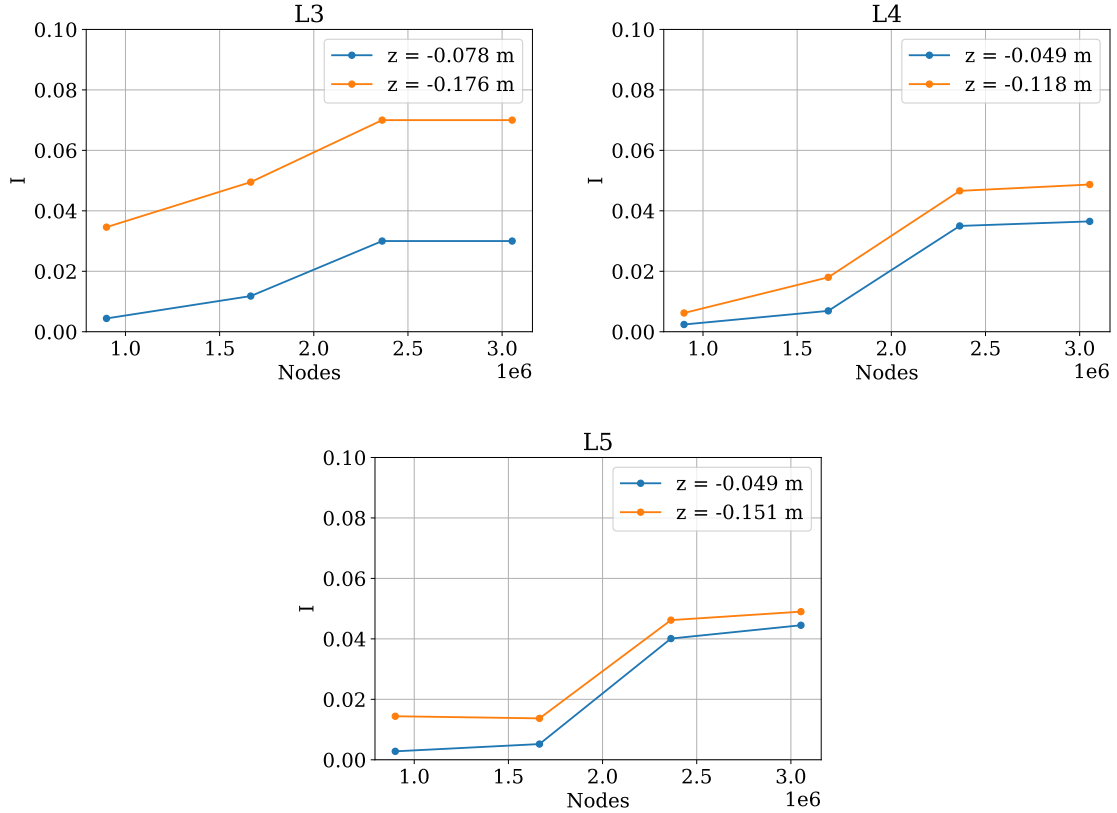


Figure 4.3 – Benchmark mesh grid analysis at two selected heights for the turbulence intensity I for regions L3, L4 and L5, obtained by the $k - \varepsilon$ model.

flow for the benchmark channel, divergences most likely caused by the bends. With the $k - \varepsilon$ model eliminated, the decision lies between the RNG $k - \varepsilon$ model and the RSM. For all six profiles, the RSM manages to predict surface velocities closest to the experimental data. Regarding its capabilities of coping with boundary layer effects, this model also demonstrates promising results. As this model calculates the Reynolds stress components directly, opposed to eddy-viscosity models, allows for a more accurate modeling of the anisotropic turbulence in the benchmark channel. For region L5, this model shows a transverse velocity value almost equal to the experimental data near the channel bed. This gives the RSM the advantage over the RNG $k - \varepsilon$ model, which seems to perform reasonably in all situations, also modeling anisotropic turbulence adequately, but not as capable as the RSM. Thus, complying with the two stated considerations earlier in this paragraph, the RSM is more than likely capable of simulating unpredictable flow behavior in a natural channel. In all finality, the RSM is presented as the best performing turbulence model for the benchmark channel flow.

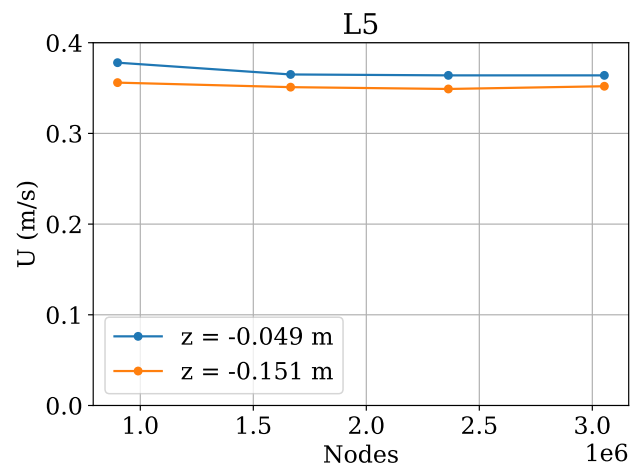
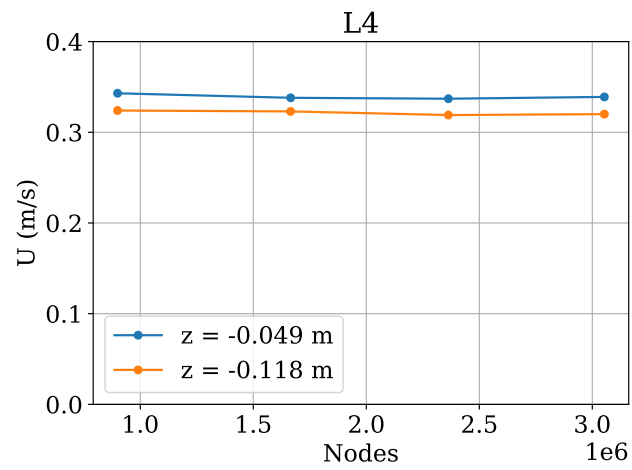
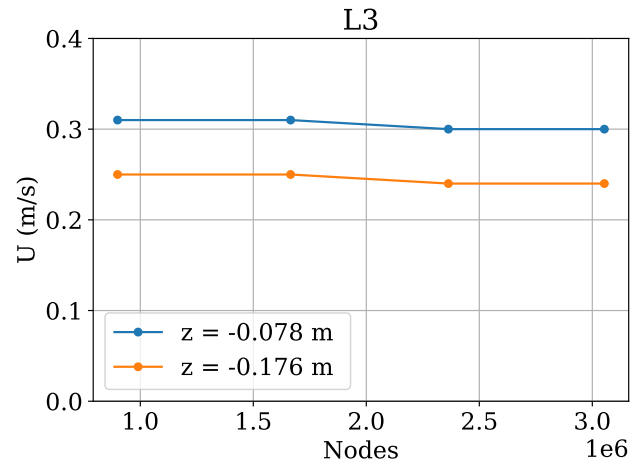


Figure 4.4 – Benchmark mesh grid analysis at two selected heights for the average velocity U for regions L3, L4 and L5, obtained by the $k - \varepsilon$ model.

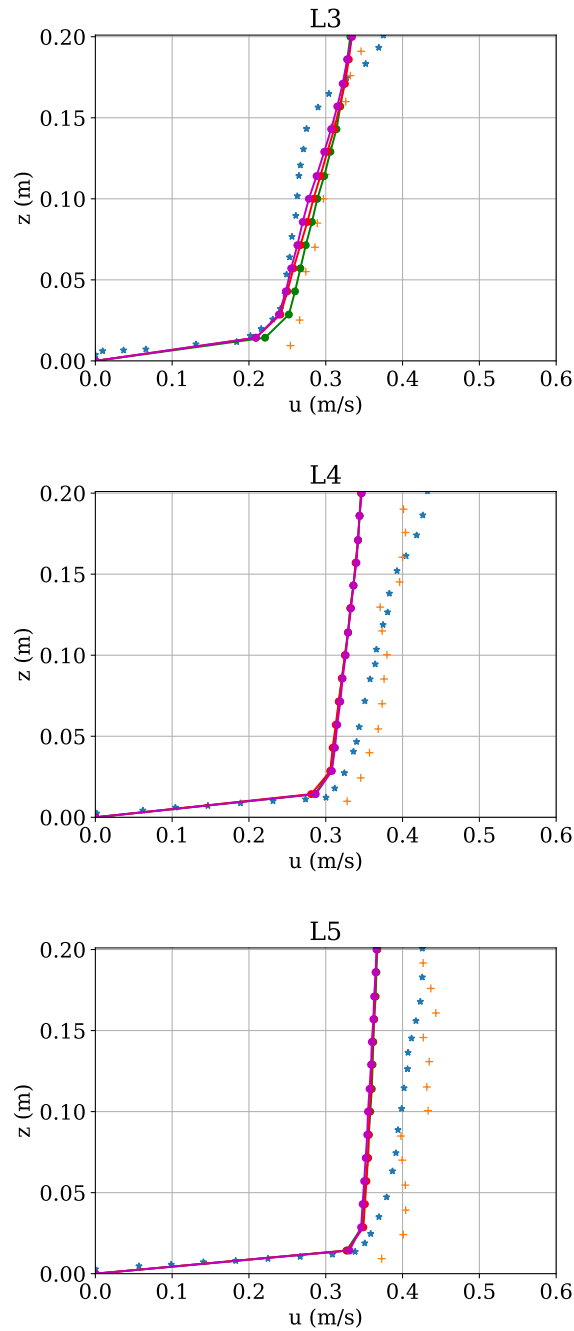


Figure 4.5 – Results comparison among the simulated models in present work, experimental and numerical results derived from Jing et al. (2011) [31] for the longitudinal velocity u from regions L3, L4 and L5. The \star and $+$ graphs are assigned to the numerical and experimental results by Jing et al. (2011) [31] while the green, red and purple lines represent the simulated results by respectively the $k-\varepsilon$, the RNG $k-\varepsilon$ model and the RSM.

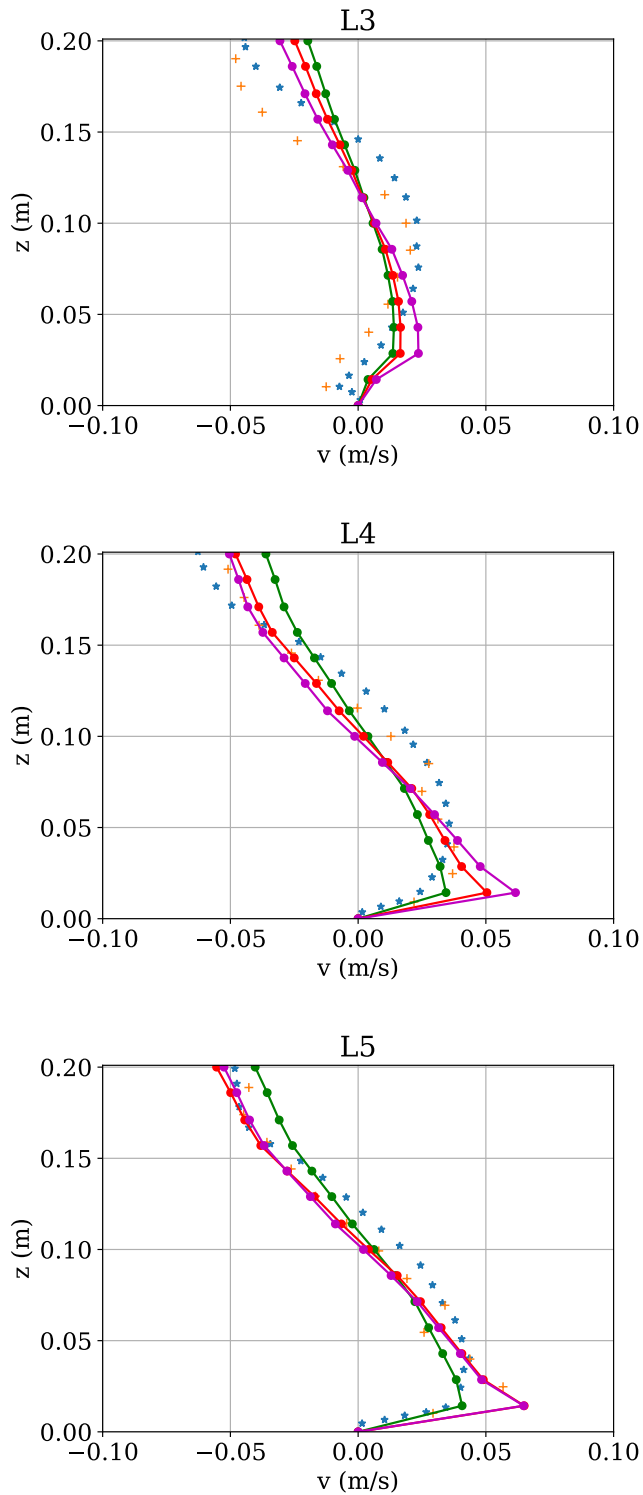


Figure 4.6 – Results comparison among the simulated models in present work, experimental and numerical results derived from Jing et al. (2011) [31] for the transverse velocity v from regions L3, L4 and L5. The \star and $+$ graphs are assigned to the numerical and experimental results by Jing et al. (2011) [31] while the green, red and purple lines represent the simulated results by respectively the $k - \varepsilon$, the RNG $k - \varepsilon$ model and the RSM.

4.2 NUMERICAL RESULTS VALIDATION

With the better performing model established, it becomes important to know whether the simulated values by this model are in fact acceptable to reproduce the results generated by Jing et al. (2011) [31]. As this methodology will ultimately be employed to simulate the flow within a natural channel, it is of utmost importance for the simulated results in this work to approximate the experimental results. Out of all six profiles, the greatest discrepancy between these two results is recorded by the longitudinal velocity profile of L5 at a depth of approximately 0.10 *m*. Value comparisons for this region show the simulated value differing 18% from the experimental results. Likewise, the greatest divergence of 100% between both types of results provided by Jing et al. (2011) [31] is observed at the transverse velocity profile of L3, where the numerical result predicts a positive value, and the experimental a negative value, resulting in this high percentage. Compared to a mere 18% difference from the experimental results, the simulated results by the RSM are indeed considered acceptable.

4.2.1 Velocity streamlines

An important feature also necessary to be predicted by the proposed methodology in this work is (strong) secondary flow. A first indication towards this attribute of the benchmark channel may be found within the velocity streamlines. Figure 4.7 shows the velocity streamlines of present work and the experimental and numerical results obtained by Jing et al. (2011) [31]. Both numerically generated results differ from the experimental in the main channel. The difference can be explained by difficulties in numerically capturing the complex flow interaction, caused by shearing forces, momentum exchange and significant flow velocity differences between the floodplain and main channel flow. Both numerical results in Fig. 4.7a and b show in the main channel region the highest local velocity near the left bank. The floodplain area displays high local velocities in the interaction area between main channel and floodplain. Overall, the simulated streamlines of present work show lower velocities compared to the numerical results by Jing et al. (2011) [31]. This was already clear from the principal flow velocity (longitudinal velocity), where especially in the main channel, present work underestimates the velocities compared to the reference data. The experimental result in Fig. 4.7c seems to demonstrate a small vortex in the middle of the channel, suggesting strong secondary flow. Even though this occurrence is not demonstrated by present research through the velocity streamlines, the occurrence of secondary flow in this particular section is further researched in the next paragraph.

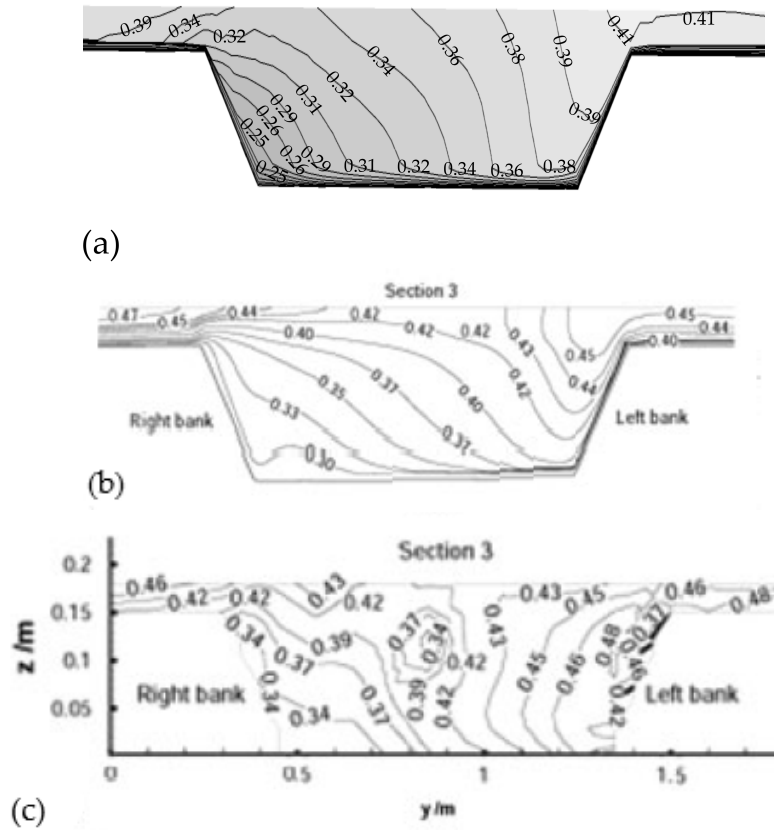


Figure 4.7 – Velocity contours and streamlines for case 3, obtained by (a) present research and both (b) numerically and (c) experimentally by Jing et al. (2011) [31].

4.2.2 Presence of secondary flow

The presence of secondary flow is further researched through a projection of the secondary currents in the cross sectional plane. Figure 4.8 presents the comparison between the currents generated by the RSM and the numerical research by Jing et al. (2011) [31].

Figure 4.8 presents a clearly noticeable occurrence of secondary flow. The velocity vectors form a rotating pattern, clearly indicating this phenomenon. Near the free surface, the currents follow a direction to the left channel bank. Near the channel bed, the flow follows to the right bank of the channel, ultimately generating a clockwise rotating vector field. Caused by the secondary flow direction, the density of the vectors is high coming in from the right bank, remaining in the main channel, where the flow starts circulating, leaving a low velocity flow with less movement and low vector density entering the left bank. Visualizing the flow for section 3 clearly demonstrates how the longitudinal velocity can be affected by the rotating flow, distorting data with heavily varying velocities and causing extremely turbulent flow, giving reason to avoid these areas for installing turbines.

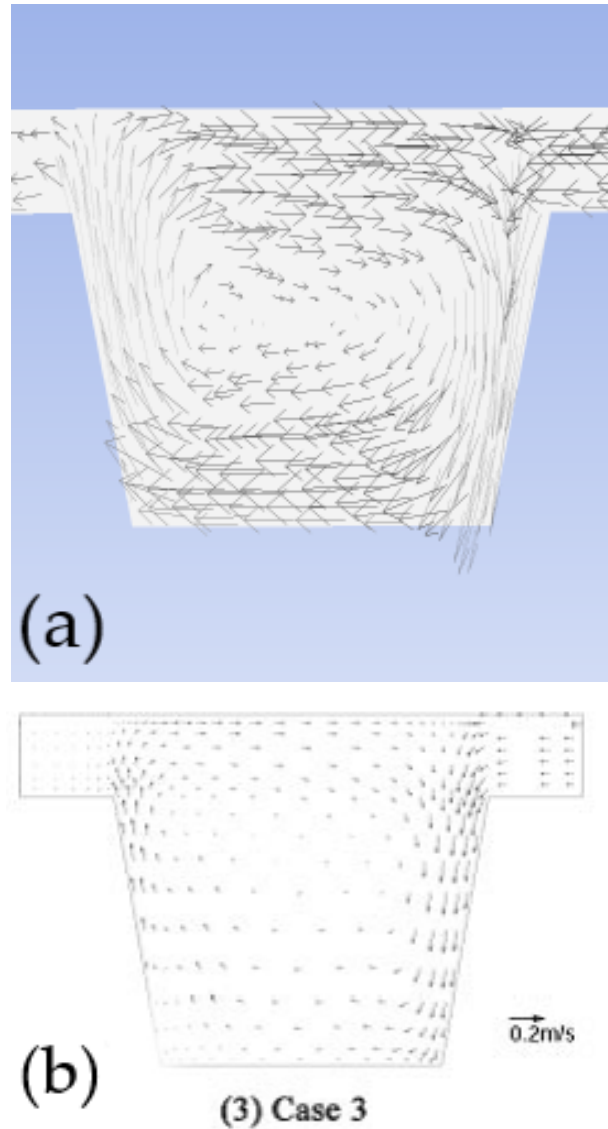


Figure 4.8 – Rotating secondary flow vectors for case 3, obtained numerically employing (a) the RSM and (b) derived from Jing et al. (2011) [31].

Summing up the results presented up to this part of the research, the proposed methodology employing the RSM has managed to generate longitudinal and transverse velocities with an acceptable discrepancy, similar velocity streamlines and the presence of secondary flow. As the objective of the benchmark simulations is to approximate the flow measurements within the artificial channel, the proposed methodology is deemed capable of reproducing the flow within a compound meandering channel.

4.3 SEFAC CHANNEL MESH GRID ANALYSIS

Following the best performing turbulence model from the turbulence model assessment study, the RSM is employed for all simulations concerning the natural channel

geometry. In this paragraph, the mesh grid analysis is realized for three increasing mesh sizes, shown in Tab. 4.3. The variables monitored are the same as during the benchmark grid analysis: the velocity U and the turbulence intensity I , of which the results are shown in Fig. 4.9.

The variances in the results for both variables are shown to decrease with the mesh size. The divergences are the greatest near the water surface and channel bed. The same problems were encountered during the benchmark turbulence model performance assessment, where the different models presented varying predictions near these same two areas. In the case of the natural channel, convergence nearing the water surface is of importance, as the turbines will be installed in this location. For a better understanding of the convergence of the solution, the diverging profiles near the water surface will be studied at a selected height for their behavior in regard to the increasing mesh size, with the results given in Fig. 4.10. Both the velocity and turbulence intensity show a stable behavior for the last two meshes, the values showing only a difference of $\approx 1\%$, signifying that the solution has converged.

The natural channel mesh generation time increases with the mesh size, increasing the computation time, as shown in Tab. 4.4. The simulations were carried out using the same server and processor as in chapter 4.1.1. The simulations here were also realized with parallel processing. Taking a higher computational cost and the convergence results into consideration, the final mesh is generated with a linear global element size of 0.6 m and tetrahedral elements, resulting in a mesh with 2316906 nodes and 12266673 elements. For a better convergence of the solution in the depression area, a local refinement is applied to the mesh.

Table 4.3 – Mesh sizes for the natural channel mesh grid analysis.

Mesh	Nodes
1	515182
2	788902
3	2421211

Table 4.4 – Processing time for the simulations employing different natural channel mesh sizes.

Mesh size	Processing time
515182	≈ 24 hours
788902	≈ 1 day and 5 hours
2421211	≈ 4 days

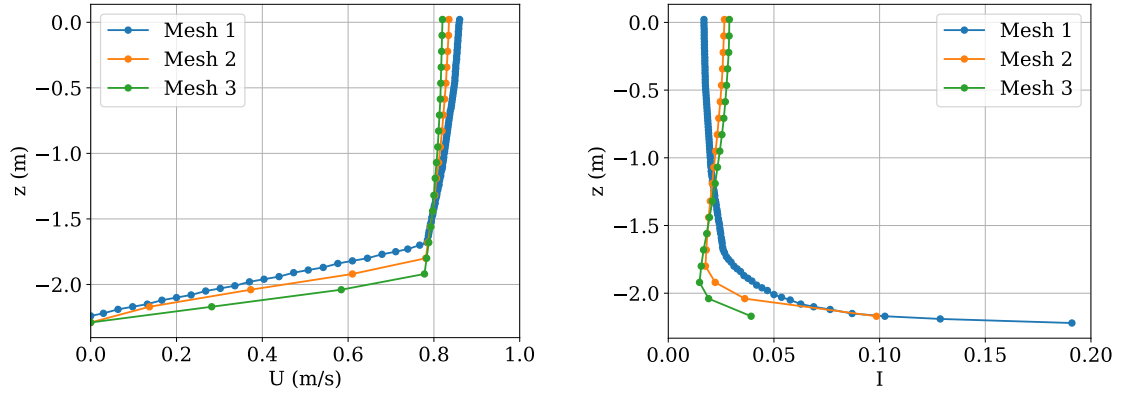


Figure 4.9 – Velocity U and turbulence intensity I profiles by the RSM for the three meshes.

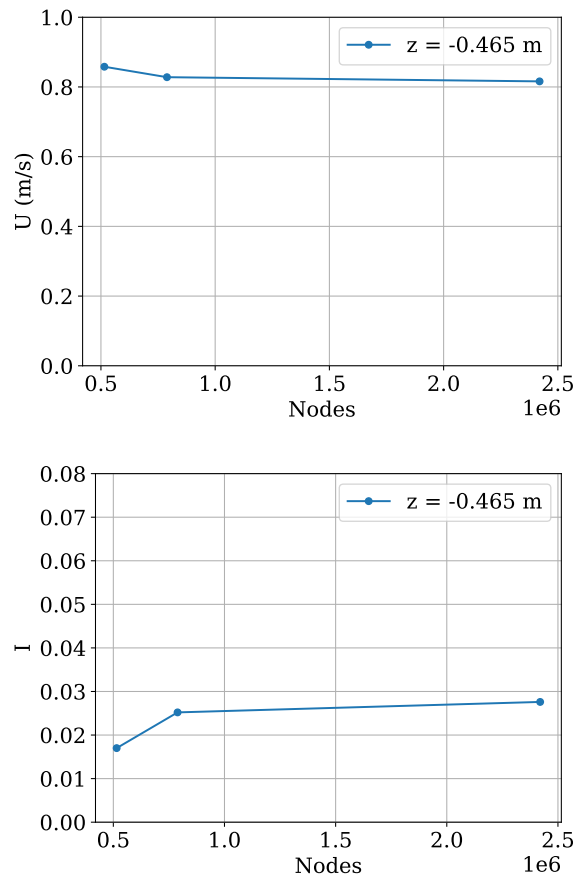


Figure 4.10 – Selected velocity U and turbulence intensity I values plotted against the mesh size obtained by the RSM.

4.4 DESCRIPTION SEFAC CHANNEL GEOMETRY

Studying the Sefac geometry may aid in understanding the flow and possible limitations to installing turbines within this channel. Figure 3.4 presents the Sefac channel without bends. The studied section of the channel downstream contains a straight

reach with a length of 345.27 *m* and a maximum width of 108.99 *m*. The channel width at the inlet is 78.53 *m*. The channel narrows until a value of 65.62 *m* is reached, after which the width increases reaching the broadest part of the channel. The channel bed, given in Fig. 4.11, appears to be strewn with rocks, displaying a rugged area and indicating high level of turbulence in this area. The deepest part is the channel is a depression area right after the inlet, measuring at a depth of 24.5 *m*. The second highest values of depth are encountered in the narrowest part of the channel, with depths of up till 6 *m*. The cross sectional area of the channel resembles section 3 case 3 of Jing et al. (2011) [31]. The highest depth values are found in the middle of the channel, shallowing out in the direction of the river bank. The final result resembles a compound channel with a trapezoidal cross section, consolidating the selection of this open-channel type as the benchmark.



Figure 4.11 – Channel bed of the Sefac channel, obtained by the experimental data collection team with the Chasing Dory underwater drone.

4.5 SELECTION OF INSTALLATION PLANES FOR THE TURBINES

4.5.1 Initial selection

The factors taken into consideration for determining potential turbine sites are: high velocity areas, sufficient depth to install the turbines and low levels of turbulence, signifying low secondary flow. Figures 4.12 and 4.13 present the depth and velocity contours obtained by simulations with the RSM, the most reliable and consistent model following the benchmark channel simulations. Figure 4.12 shows the encountered depths within the simulated natural channel through a contour map. The contour

map places the average depth between 0 and 2.5 m. The yellow-green areas in Fig. 4.13 represent the high velocity areas across the channel. The contours in Fig. 4.13 show in general the highest and lowest velocities located near the channel banks. Unfortunately, for most cases hydrokinetic energy harvesting would prove more than likely difficult, as near the river banks, the depth is not adequate for installing turbines.

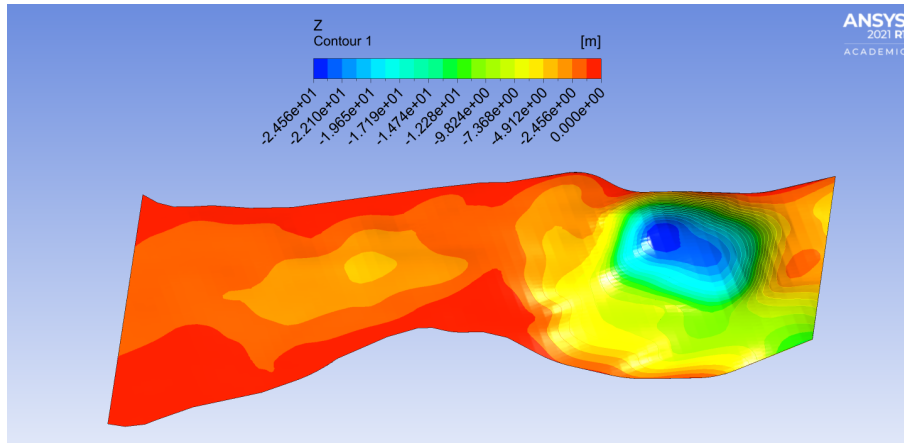


Figure 4.12 – Depth contours obtained by the RSM simulation with the deepest area located right after the inlet and the shallowest areas at the channel banks, indicating a compound channel cross section.

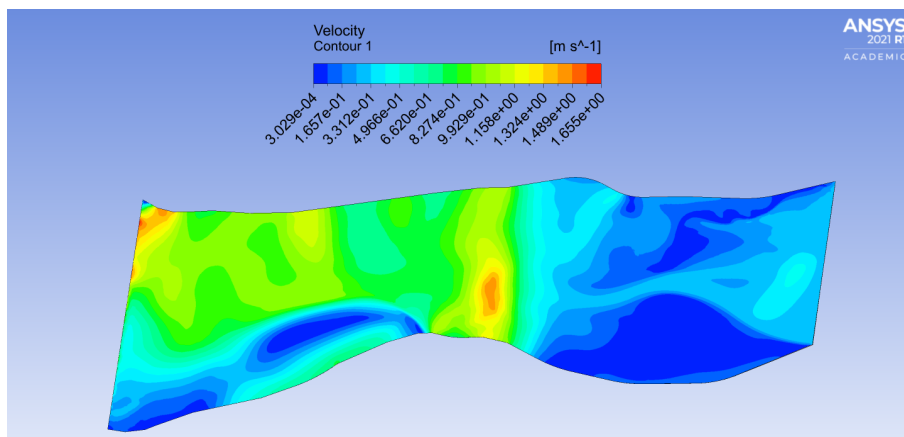


Figure 4.13 – Velocity contours obtained by the RSM, with the free surface showing yellow-green to red contours as high velocity areas.

Studying the velocity and the depth contours allows for initiating the process of finding potential sites for the turbines. The highest velocities are found in 5 sections in the channel, presented in Fig. 4.14. The planes are created from bank to bank, crossing specifically the yellow-green contoured areas. The section width y appears in descending order, with section 5 having the widest and section 1 the narrowest width. Out of all planes, plane 5 is the closest to the outlet boundary, creating the probability of the high velocities in this region influenced by the outlet boundary condition. However, this plane may be safely included in the search for high velocity regions, as the

convective characteristic of the flow creates a weaker influence on the outlet boundary condition as opposed to the inlet boundary condition. Plainly described, the outlet boundary condition has in this case no significant influence on the results in the plane 5 region.

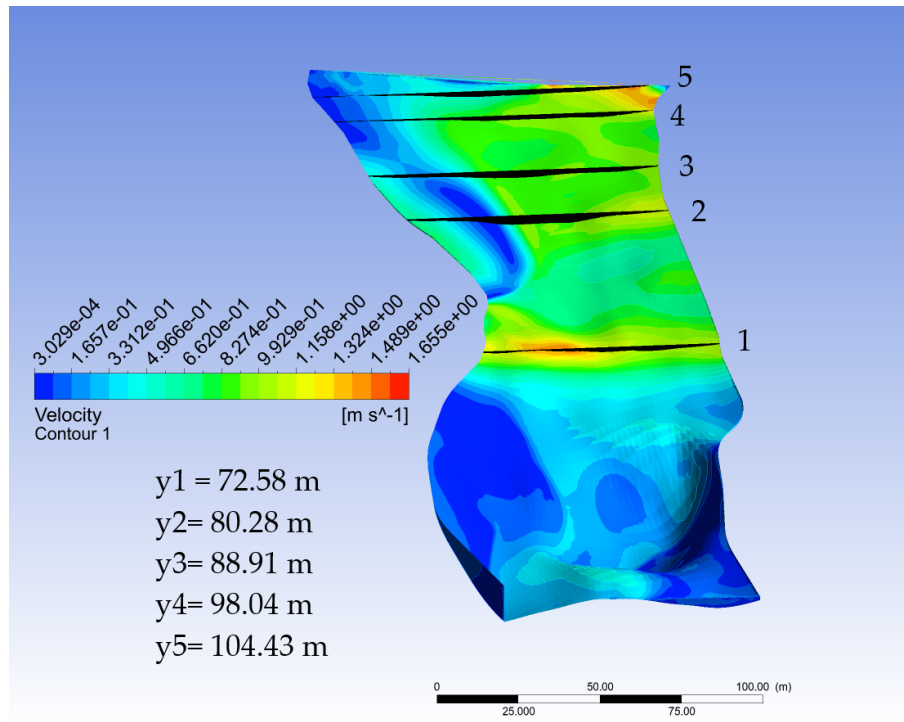


Figure 4.14 – Velocity contour map with initially selected transverse planes and their width y for installing the turbines located in potentially high velocity and sufficient depth areas.

As an accurate velocity value cannot be ascertained from the contours, further research is necessary for finding the specific values for the sections. Each section is studied separately by selecting four regions per section, spaced at an approximate equal distance and also located in the deeper areas in the plane, to retrieve more accurate information on the velocities, depths and turbulence levels. Figures 4.15 - 4.19 shows the local velocity contours per section with the selected regions for data retrieval.

According to Figures 4.15 - 4.19, the maximum depth per section varies from 1.64 m to 3.30 m . These values allow for the installation of a small turbine.

The four selected regions per plane are placed in areas where the sections indicate the highest velocity and depth values. From studying the different contours in Figures 4.15 - 4.19, a preliminary conclusion can already be drawn on the planes containing the highest velocities. Based on the contours, sections 1 and 5 would make great selections as turbine sites, with velocities appearing to be above 1 m/s . Planes 2, 3 and 4 appear to contain velocities in the range of $\approx 0.9 m/s$ to 1 m/s . An in-depth study of velocity profiles will provide definitive information on the values.

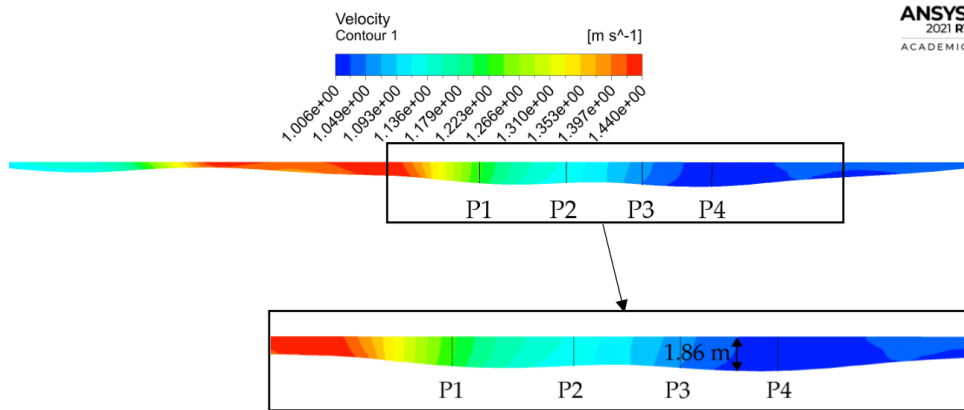


Figure 4.15 – Local velocity contours of plane 1 focused on the four selected regions, starting at the left side of the plane (from the inlet’s point of view) with P1 and ending with P4, along with the maximum depth for further analysis of the velocity and turbulence levels.

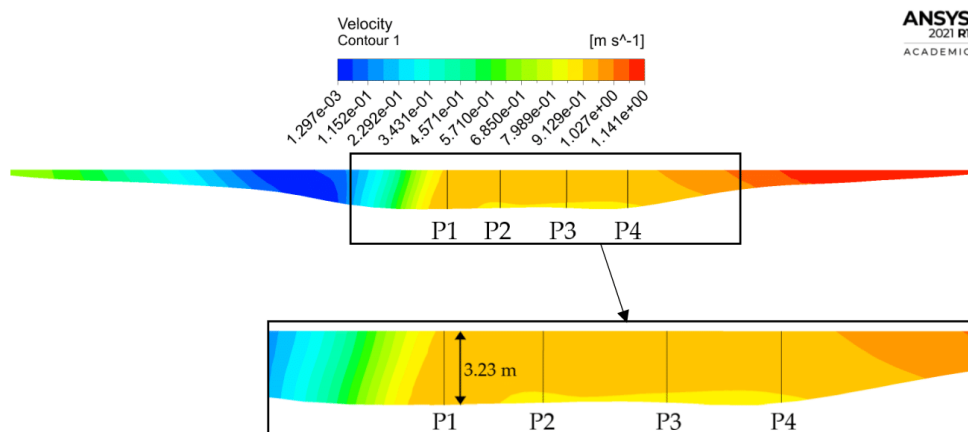


Figure 4.16 – Local velocity contours of plane 2 focused on the four selected regions, starting at the left side of the plane (from the inlet’s point of view) with P1 and ending with P4, along with the maximum depth for further analysis of the velocity and turbulence levels.

4.5.2 Final plane selection

The initial site selection is based on only the required depth and velocity as per the contours. This paragraph focuses on narrowing down the planes along which turbines may be installed by studying the velocity profiles given by Figures 4.20 - 4.24.

All velocity profiles show typical turbulent flow profiles, with a steeper behavior near the channel bed. The graph shows a gradual increase in velocity until a certain depth is reached. From thereon, the velocity only increases sharply till the surface velocity is reached. It is noticeable that the velocity profiles presented by the natural

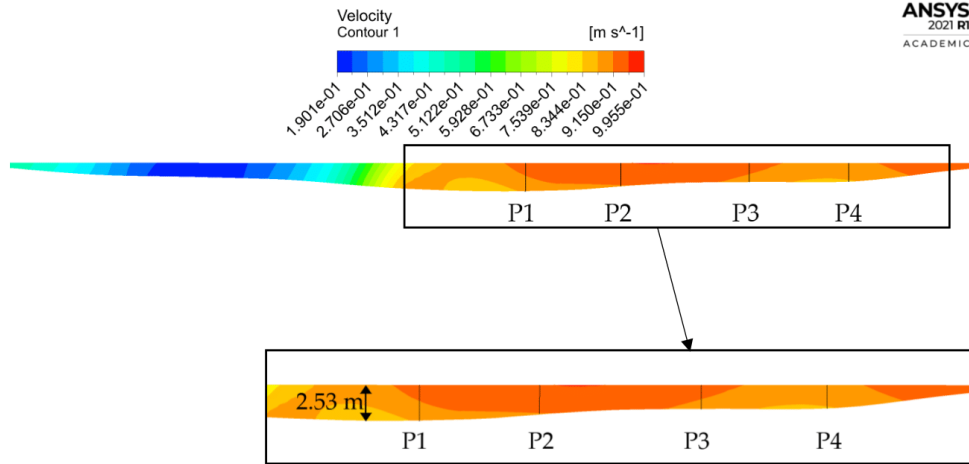


Figure 4.17 – Local velocity contours of plane 3 focused on the four selected regions, starting at the left side of the plane (from the inlet’s point of view) with P1 and ending with P4, along with the maximum depth for further analysis of the velocity and turbulence levels.

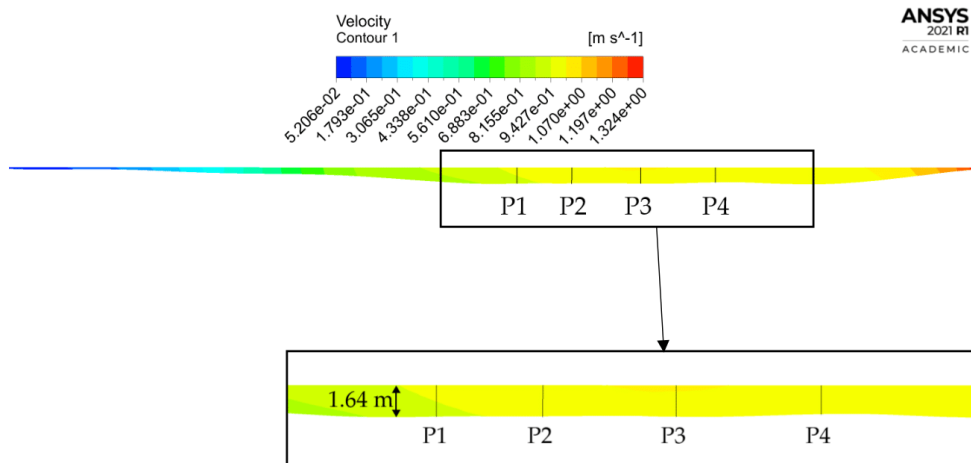


Figure 4.18 – Local velocity contours of plane 4 focused on the four selected regions, starting at the left side of the plane (from the inlet’s point of view) with P1 and ending with P4, along with the maximum depth for further analysis of the velocity and turbulence levels.

channel differ in their behavior from those studied during the benchmark simulations. This is to be expected, as the flow for the natural channel is created by a different and more complex geometry, creating different interactions between the channel bed, walls and the free surface.

As expected from the velocity contours in Fig. 4.15 - 4.19, planes 1 and 5 demonstrate velocities higher than 1 *m/s*. Out of the eight studied regions between these two planes, P1 of plane 1 attains the highest velocity at 1.23 *m/s*, whereas the lowest

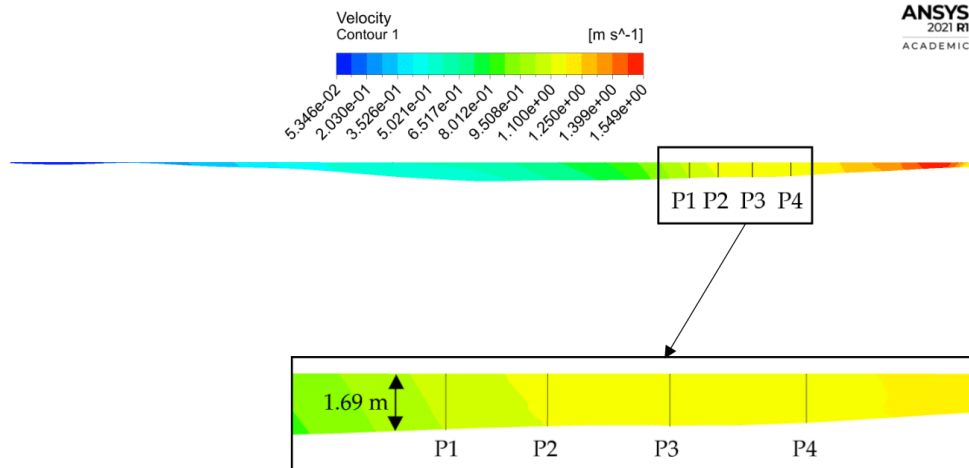


Figure 4.19 – Local velocity contours of plane 5 focused on the four selected regions with the highest depth and velocity values, starting at the left side of the plane (from the inlet’s point of view) with P1 and ending with P4, along with the maximum depth for further analysis of the velocity and turbulence levels.

velocity is also demonstrated by plane 1, however in region P4. The remaining three planes produce values close to 1 m/s , with the lowest encountered in plane 3 P2 at 0.90 m/s . Three-quarters of the profiles of plane 2 show values above 0.95 m/s , which could lead to this plane also being considered for installing turbines, as the velocity is the closest to 1 m/s out of the three remaining sections.

Regarding the depth, the velocity profiles show a minimum value of approximately 1.5 m . This depth will be adequate for installing small turbines.

After completing this part of the study, a clear understanding of the velocity behavior within the five chosen planes is achieved. Considering the velocities and depths encountered in these profiles, sections 1 and 5 are already confirmed as final siting planes, as predicted in section 4.5.1. Out of the three remaining planes, the last selected plane is finalized by also taking into account one last consideration: the wake recovery of the turbines for the maximum extraction of the hydrokinetic energy. Sections 1 and 5 are located at a good distance (more than $20D$) from other sections for the wake recovery. Sections 2, 3 and 4 present velocities near 1 m/s , with section 4 displaying the highest velocities. Nevertheless, section 4 can already be discarded, as the distance between planes 4 and 5 would not be sufficient for the wake recovery and between these two planes, plane 5 attains the highest simulated velocities, with the depths not differing much. Out of planes 2 and 3, plane 2 exhibits the highest velocities, close to 1 m/s and the highest depth values out of all five planes. As plane 3 velocities do not differ much from plane 2, the choice could be made of including this plane in the official selection, however, considering also the wake recovery discards this

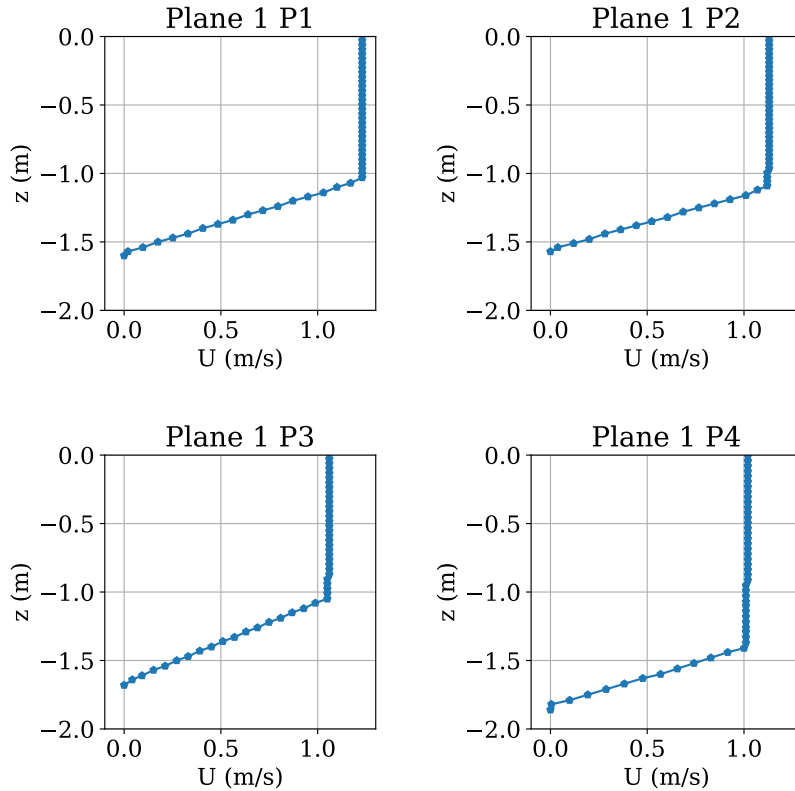


Figure 4.20 – Simulated velocity profiles of the four studied regions for plane 1 with a mass flow rate \dot{m} of 91000 kg/s .

option.

This selection of planes can only be finalized provided none of these planes demonstrate high levels of turbulence. To this end, the secondary flow, an indicator of high turbulence in these planes, is studied in Fig. 4.25.

The secondary velocity in the relevant areas, where the four regions are located, presents extremely low to negative values. The highest value, ≈ 0.24 m/s is encountered in plane 5. This makes the highest secondary flow velocity approximately 21 % of the highest velocity U (1.14 m/s). For this plane and plane 2, the flow direction is uncomplicated, from the right bank to the left bank in plane 2, whereas in plane 5 the opposite flow direction is observed. Based on the flow direction in combination with the transverse velocity values, these two planes do not exhibit significant turbulent behavior. The flow direction in plane 1 may indicate high turbulent levels at P1 and P4. These two regions appear to be located in transitional areas of the transverse velocity, affecting the flow direction and indicating flow separation. The low transverse velocities indicate low turbulence, however visual evidence is needed to analyse where this turbulence is encountered and whether the turbulence is indeed low enough to not have a consequential effect on the turbine performance. Concrete proof regarding

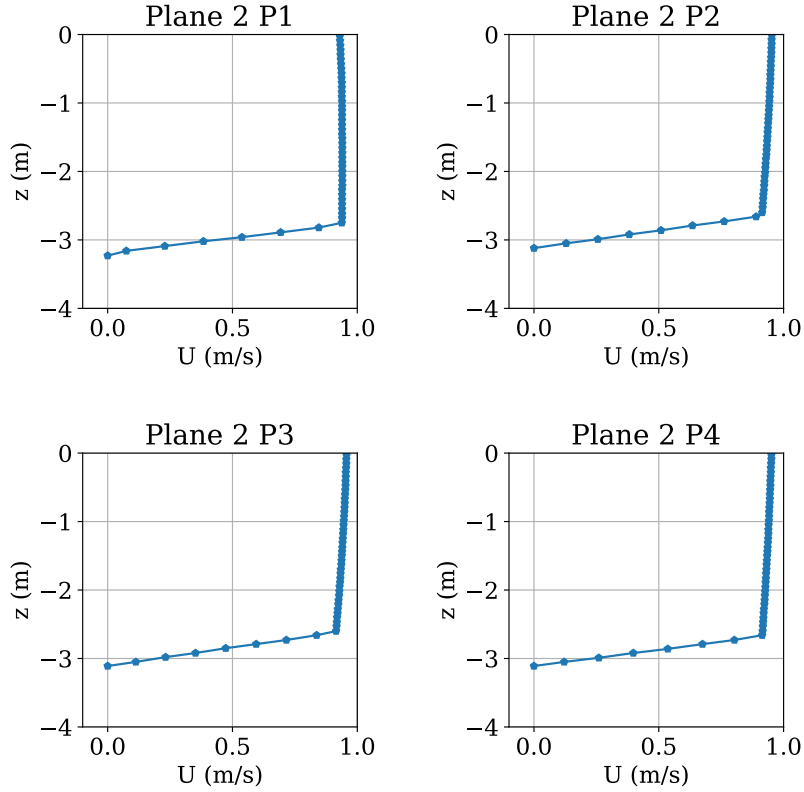


Figure 4.21 – Simulated velocity profiles of the four studied regions for plane 2 with a mass flow rate \dot{m} of 91000 kg/s .

the turbulence levels are obtained by studying the turbulence intensity profiles in Figures 4.26, 4.27 and 4.28.

All turbulence profiles show a similar graph behavior. The highest turbulence levels are encountered near the channel bed, after which this value decreases steadily in the direction of the water surface. The values encountered in nearing the water surface are extremely small, nearing zero. The levels near the channel bed vary per profile and plane. The highest and lowest maximum turbulence intensity show a significant difference, with the highest maximum intensity simulated at 0.17 (17%) at P2 of plane 2 and the lowest at 0.0053 (0.5%) for P2 of plane 5. As the highest turbulence levels, even with an extremely low level, are only encountered near the channel beds, this factor need not be taken into consideration for siting the turbines, as the turbines will most certainly be installed at a distance from this area.

In the end, specifically for this studied natural channel, the final installation planes are selected by procuring areas with a velocity close to or higher than 1 m/s and depth starting from 1.64 m . The final selection of the planes allows for determining the turbine siting per section. However, this cannot be realized by only employing data obtained by simulating one flow rate, as profiles may differ in other simulated values,

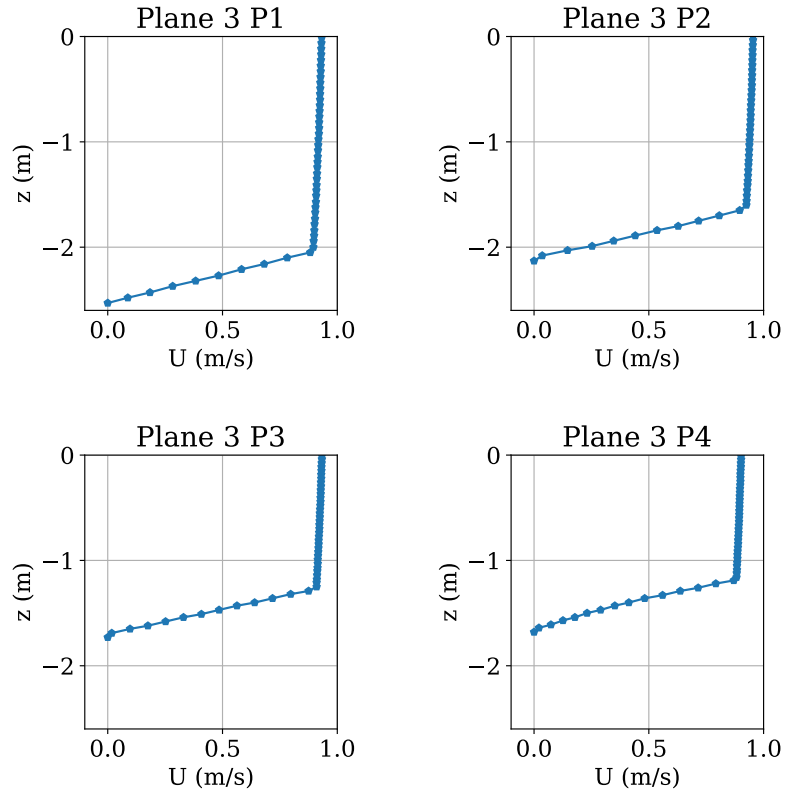


Figure 4.22 – Simulated velocity profiles of the four studied regions for plane 3 with a mass flow rate \dot{m} of 91000 kg/s .

affecting the maximum extraction of the available hydrokinetic energy in a certain profile area. Therefore, the turbine siting will be finalized using results gathered from multiple flow rates.

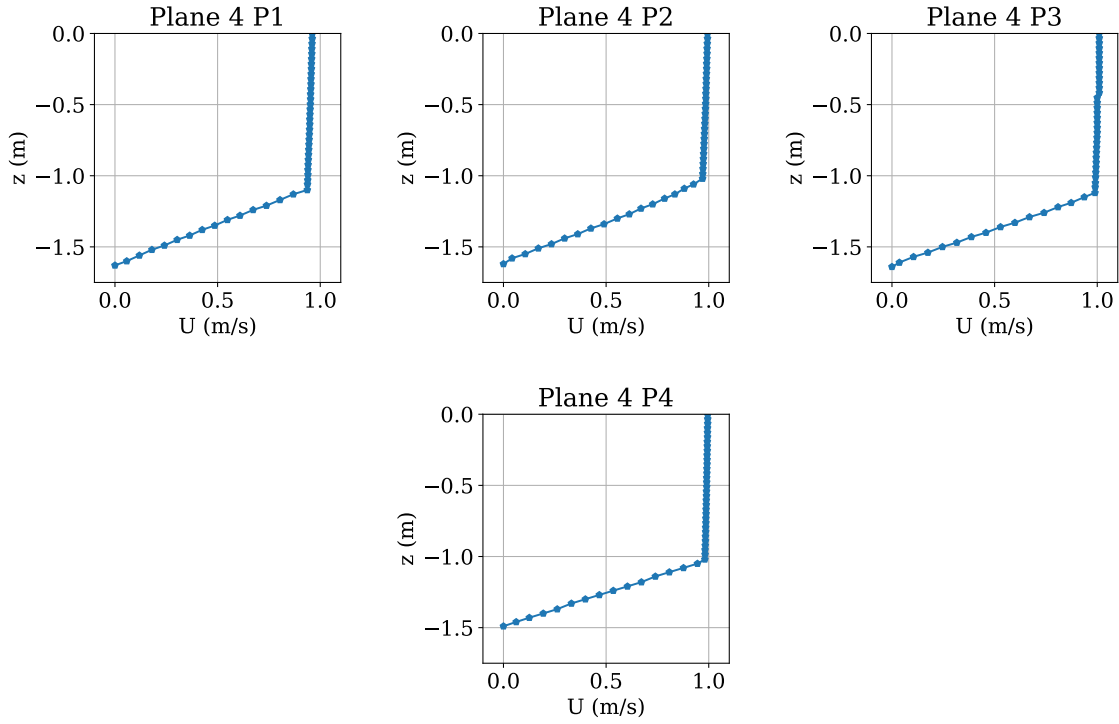


Figure 4.23 – Simulated velocity profiles of the four studied regions for plane 4 with a mass flow rate \dot{m} of 91000 kg/s .

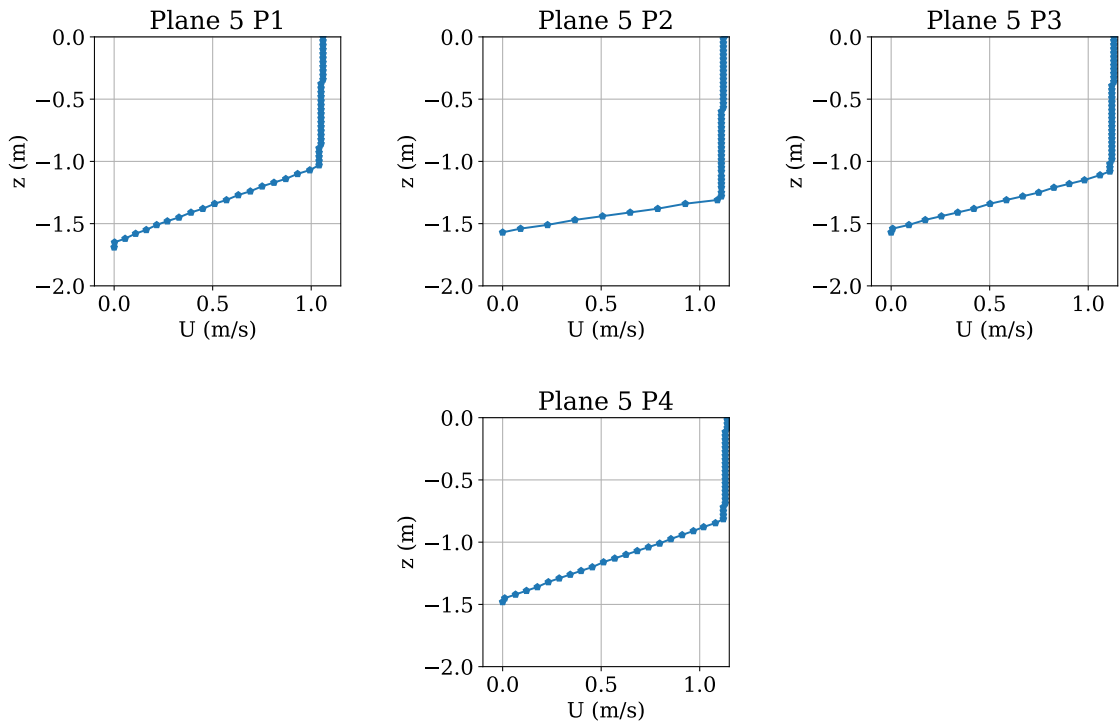


Figure 4.24 – Simulated velocity profiles of the four studied regions for plane 5 with a mass flow rate \dot{m} of 91000 kg/s .

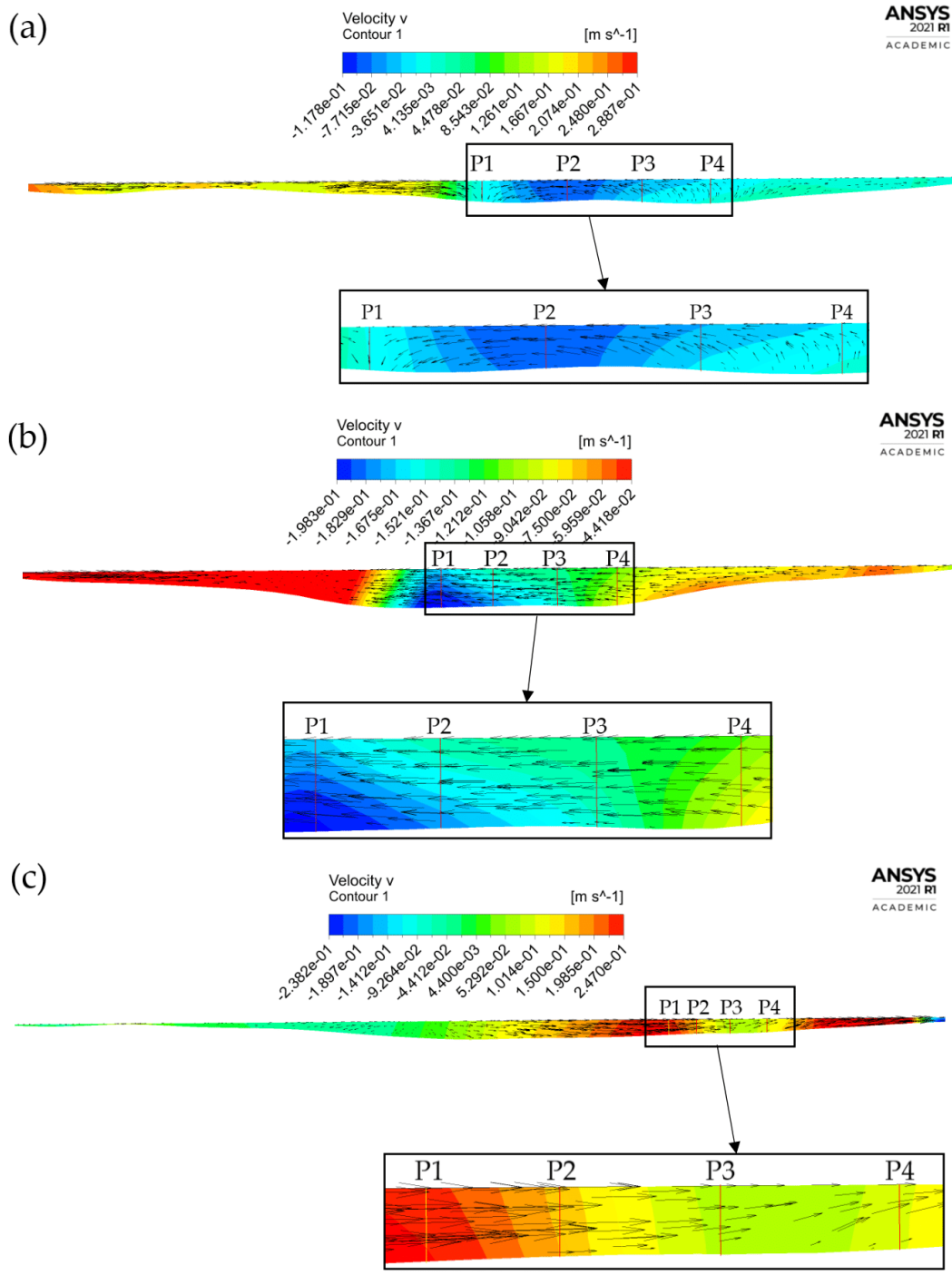


Figure 4.25 – Secondary flow and vector fields focused on the four selected regions with the highest depth and velocity values in the plane, P1-P4, for sections (a) 1, (b) 2 and (c) 5. The secondary flow field is given by plotting the transverse velocity v contours.

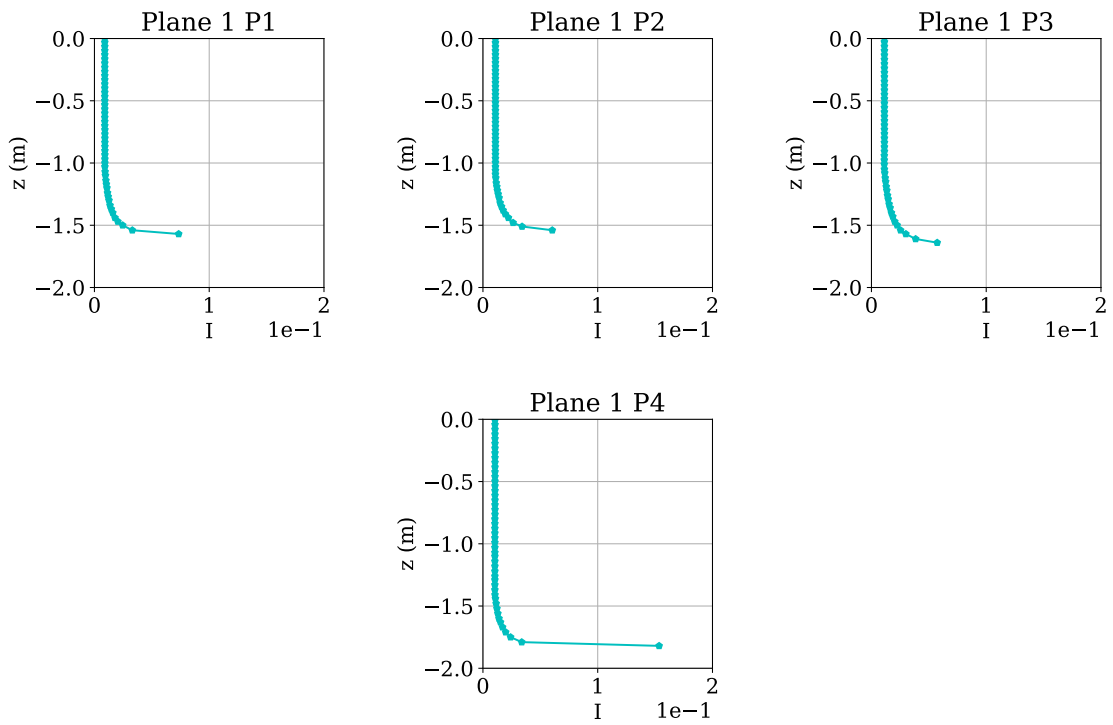


Figure 4.26 – Turbulence intensity profiles of the four studied regions for plane 1 simulated with a mass flow rate of 91000 kg/s.

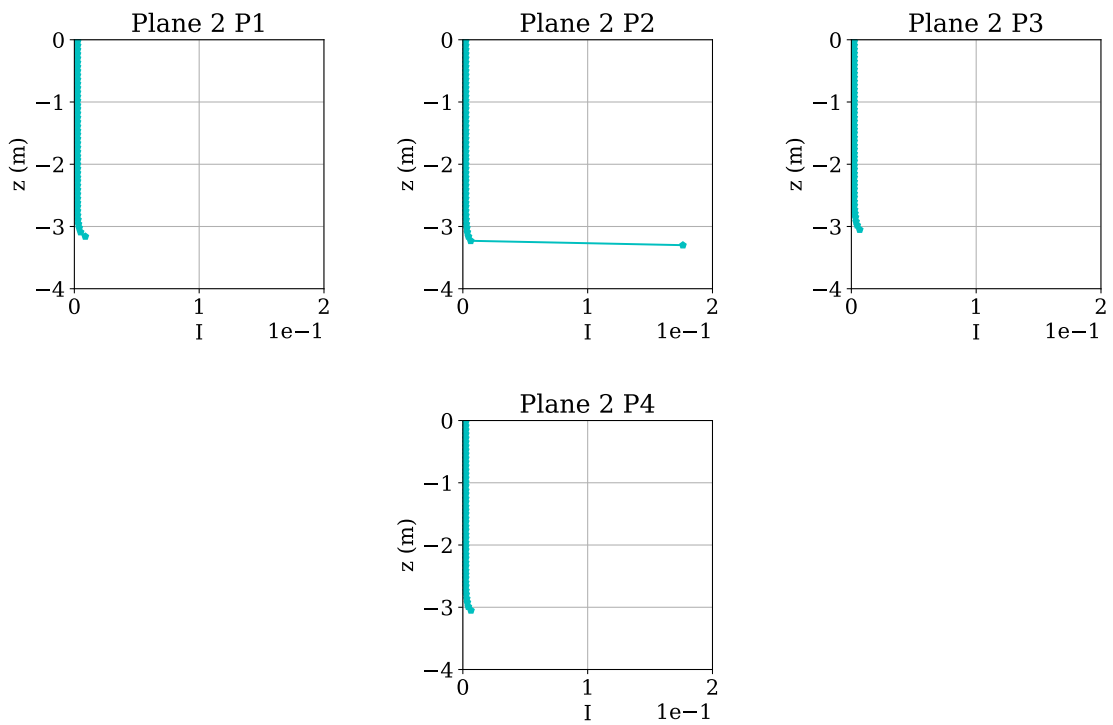


Figure 4.27 – Turbulence intensity profiles of the four studied regions for plane 2 simulated with a mass flow rate of 91000 kg/s.

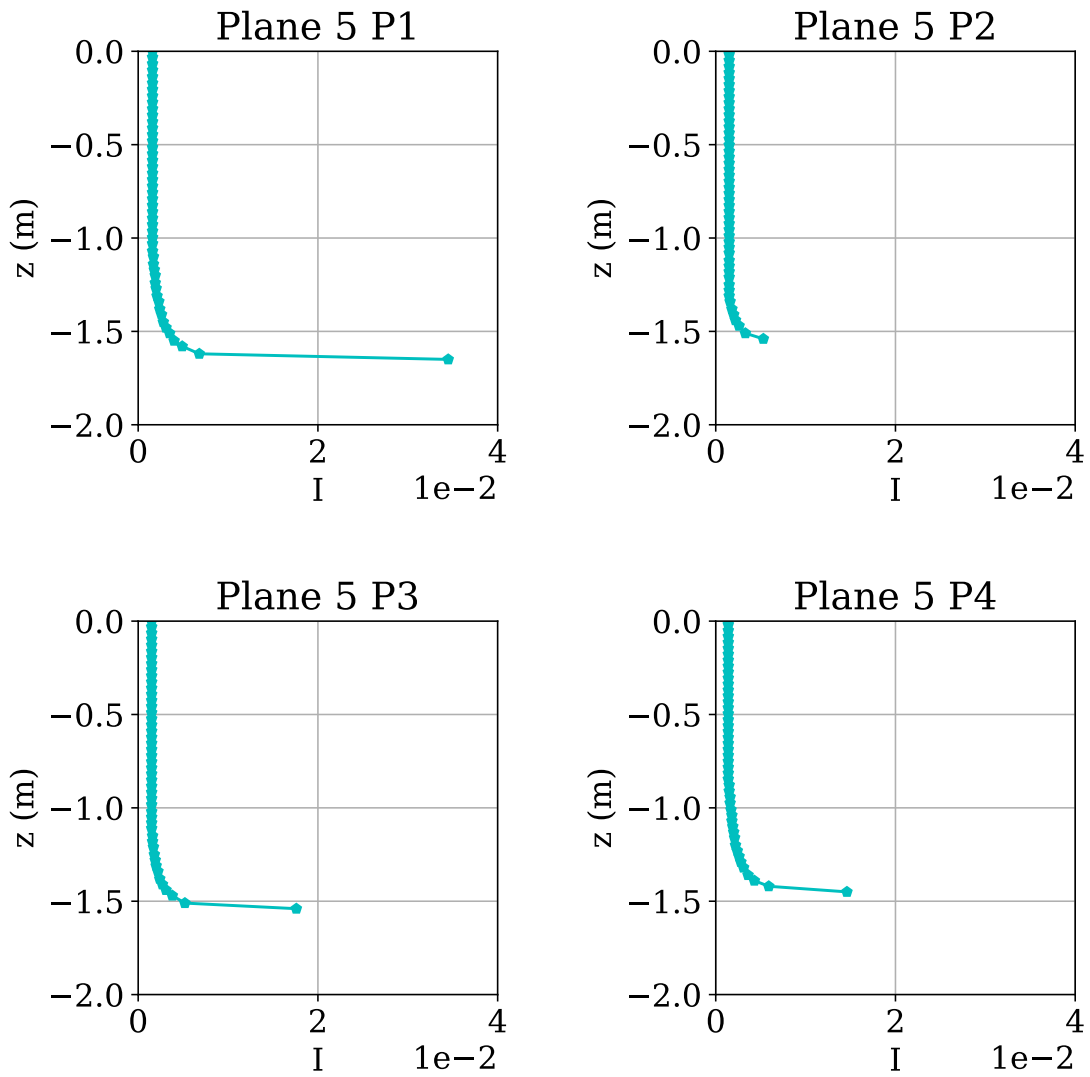


Figure 4.28 – Turbulence intensity profiles of the four studied regions for plane 5 simulated with a mass flow rate of 91000 kg/s .

4.6 ANNUAL POWER GENERATION POTENTIAL OF THE STUDIED AREA

4.6.1 Turbine siting details

The flow rates occurring with the highest frequency for the two selected periods in Fig. 3.5 are: 51.39 (period 1) and 158.72 (period 2) m^3/s . These flow rates are used as inlet boundary conditions for two additional simulations, after being converted to the mass flow rate \dot{m} , employing the RSM. Each flow rate result is discussed in a separate paragraph. The focus will be on velocity profiles simulated in planes 1, 2 and 5, as the remaining factors, such as turbulence intensity and secondary flow are not expected to show significant changes in their behavior, with the geometry remaining unchanged. The turbine siting takes place engaging the relevant velocities of the flow rates, after which the annual hydrokinetic power potential will be calculated with. After observations made in the field and during simulations, turbines with a diameter of 1 m are chosen for this research. The necessary parameters for calculating the potential generated power, $P_{converted}$, of the turbine layout, in Eq. (B.1) are:

- Power coefficient: 0.3 (obtained from the hydrokinetic rotor design project simulated by Team Lambari, described in appendix B);
- Water density: 1000 kg/m^3 ;
- For the area, a diameter of 1 m ;
- The mean velocity of the installation area.

The turbines are sited using the velocity values present at $0.4D$ below the water surface. This value must not vary more than 10% over the four regions for an efficient conversion. The turbines will be separated at a distance of $0.5D$ from each other.

4.6.2 Optimal turbine layout according to period 1

The velocity profiles for this period of the year 2018 are presented in Figures 4.29, 4.30 and 4.31. The profiles do not differ from the original case of 91000 kg/s . Table 4.5 displays the simulated velocities for where potentially turbines may be installed, which is about $0.4D$ from the surface. As it turns out, the simulated velocities are extremely low, compared to the peak condition of 1 m/s used for calculating the turbine efficiency. This is not unexpected, as the results from 91000 kg/s demonstrated velocities of approximately 1 m/s , signifying that a much lower flow rate would present much lower velocities. With these low velocities, the turbine rotor will not be brought into

movement to generate electricity, thus justifying the discarding of the mass flow rate results in period 1 (51390 kg/s) for determining the turbine siting and the annual potential power.

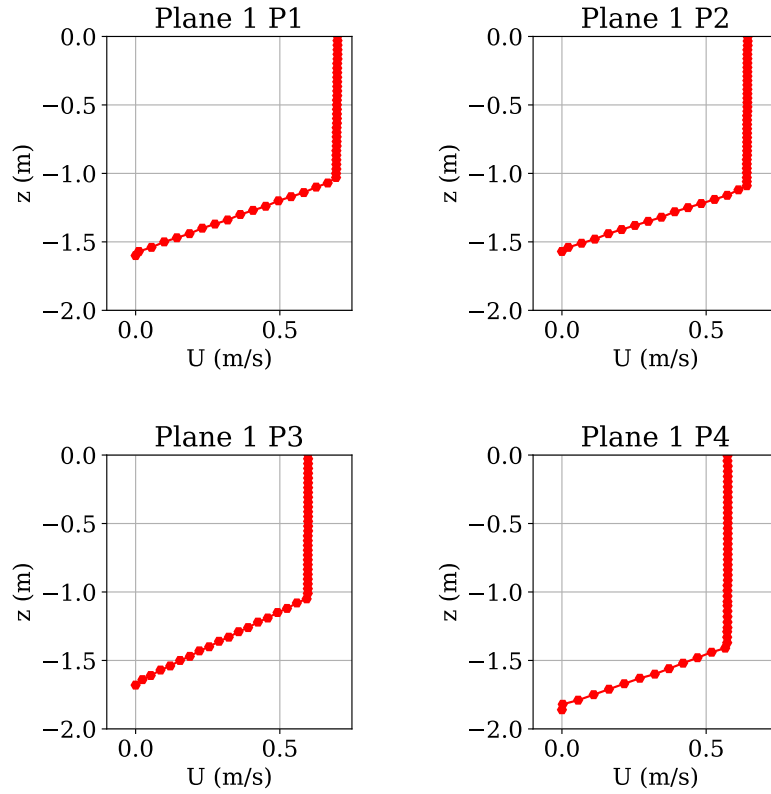


Figure 4.29 – Simulated velocity profiles of plane 1 with a mass flow rate \dot{m} of 51390 kg/s .

Table 4.5 – Simulated velocities for planes 1, 2 e 5 with a mass flow rate \dot{m} of 51390 kg/s .

Area	Velocity $U(m/s)$
Section 1 P1	~ 0.69
Section 1 P2	~ 0.64
Section 1 P3	~ 0.59
Section 1 P4	~ 0.57
Section 2 P1	~ 0.43
Section 2 P2	~ 0.63
Section 2 P3	~ 0.63
Section 2 P4	~ 0.63
Section 5 P1	~ 0.59
Section 5 P2	~ 0.63
Section 5 P3	~ 0.63
Section 5 P4	~ 0.63

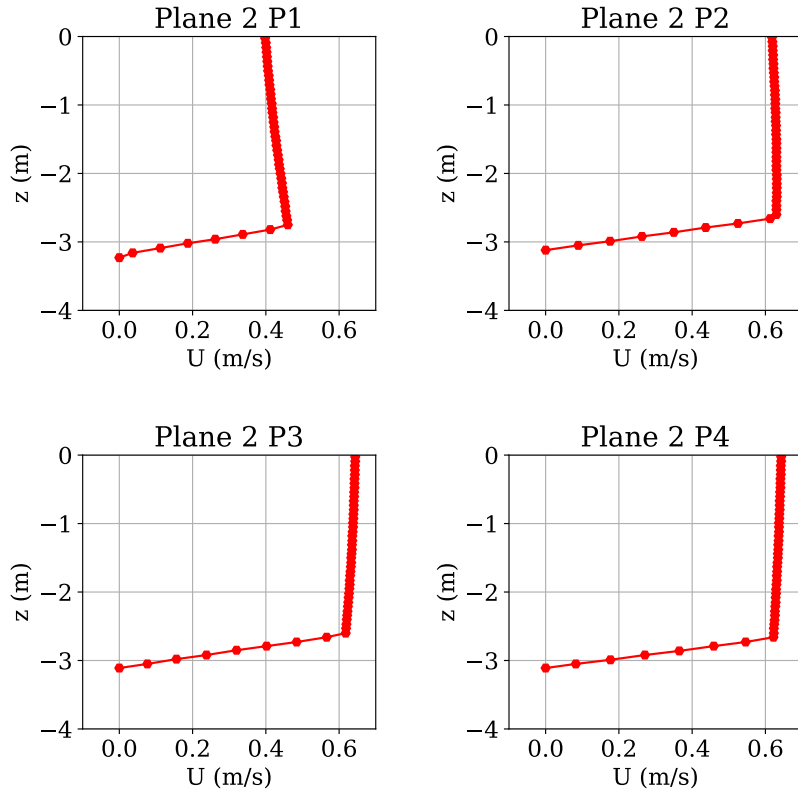


Figure 4.30 – Simulated velocity profiles of plane 2 with a mass flow rate \dot{m} of 51390 kg/s .

4.6.3 Optimal turbine layout according to period 2

The velocity profiles for this mass flow rate are found in Figures 4.32- 4.34. As the difference between the mass flow rate in period 1 (51390 kg/s) and current mass flow rate (158720 kg/s) is more than 300%, the velocities are as expected also higher, passing even the peak condition velocity of 1 m/s used for calculating the turbine efficiency. However, the higher velocities not only signify that the turbine will function during this time of the year, but also that the potential calculated generated power will be subestimated. The lowest observed velocity for this period has a value of 1.56 m/s , which is slightly higher than the 1 m/s used for the turbine efficiency. However, as the turbines will function during this period, the turbine layout can be determined.

Comparing the velocities per profile per section to each other shows plane 1 with a difference of 14.7% between the lowest and highest value. For this instance, the velocity contours prove useful in approaching the installation of turbines despite the difference in the velocity. To this purpose, the velocity contours of plane 1 produced by simulating with a flow rate of 158.72 m^3/s is presented in Fig. 4.35a. The velocity contours show clear transitioning areas between the four studied regions, leading to the assumption that dividing the four regions into two might solve the difference between

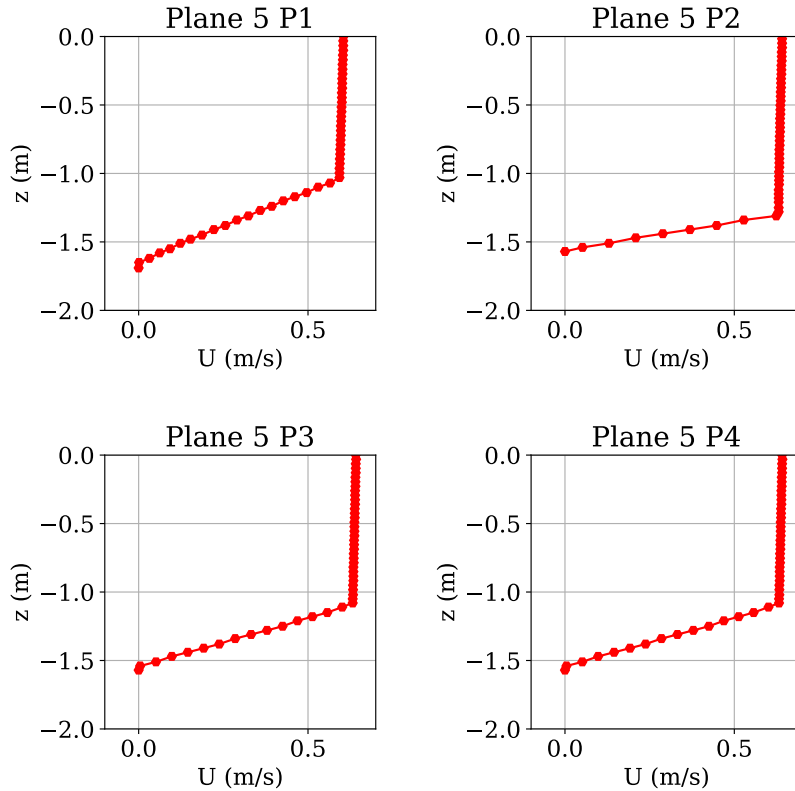


Figure 4.31 – Simulated velocity profiles of plane 5 with a mass flow rate \dot{m} of 51390 kg/s .

the velocities necessary for installing the turbines. Table 4.7 shows the results of this venture. Dividing the four regions in plane 1 into two regions A and B decreases the difference between the highest and lowest velocity up to 6.6% and 3.2% for respectively sides A and B. The largest difference between the velocities per plane for sections 2 and 5 are less than 8%, enabling the availability of all four profile areas for installation. The remaining required mean velocities per plane are also presented in Tab. 4.7.

4.6.4 Determination annual potential power generation

Simulating with two additional flow rates has proven the expected: higher mass flow rates result in higher velocities. P1 from section 1 has presented the highest velocities of all final sections of all three mass flow rates (including 91000 kg/s), while P1 from section 2 the lowest. The majority of all profiles maintained the same profile behavior as the original case. However, the turbines will only manage to generate electricity during the simulated mass flow rate during period 2: 158720 kg/s .

Considering the turbine layout determined by the velocities during period 2, section 1 needs to be divided in order to comply the less than 10% between the velocities in the four studied regions, as the profiles in the other two sections show a negligible difference

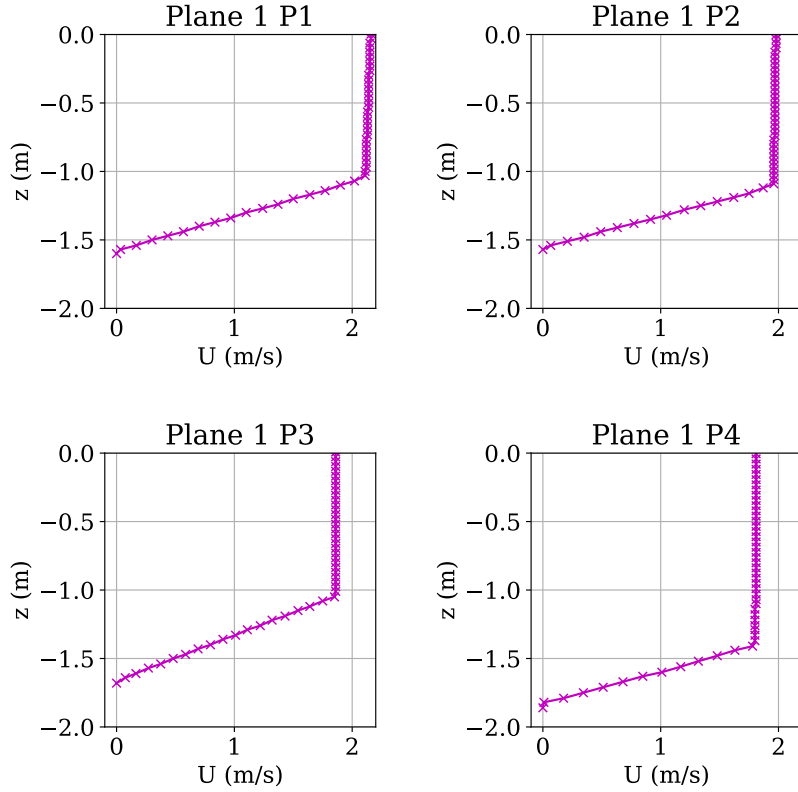


Figure 4.32 – Simulated velocity profiles of plane 1 with a mass flow rate \dot{m} of 158720 kg/s .

Table 4.6 – Simulated velocities for planes 1, 2 and 5 with a mass flow rate \dot{m} of 158720 kg/s .

Area	Velocity $U(m/s)$
Section 1 P1	~ 2.11
Section 1 P2	~ 1.97
Section 1 P3	~ 1.86
Section 1 P4	~ 1.80
Section 2 P1	~ 1.60
Section 2 P2	~ 1.56
Section 2 P3	~ 1.59
Section 2 P4	~ 1.62
Section 5 P1	~ 1.83
Section 5 P2	~ 1.95
Section 5 P3	~ 1.96
Section 5 P4	~ 1.98

between the highest and lowest predicted velocity. The velocities calculated per region in Tab. 4.7, allows for determining the available width per plane for installing the turbines in Fig. 4.35. Subsequently, the potential power generated from the turbines is presented in Tab. 4.8. The annual potential hydrokinetic power generation is calculated in Tab. 4.9.

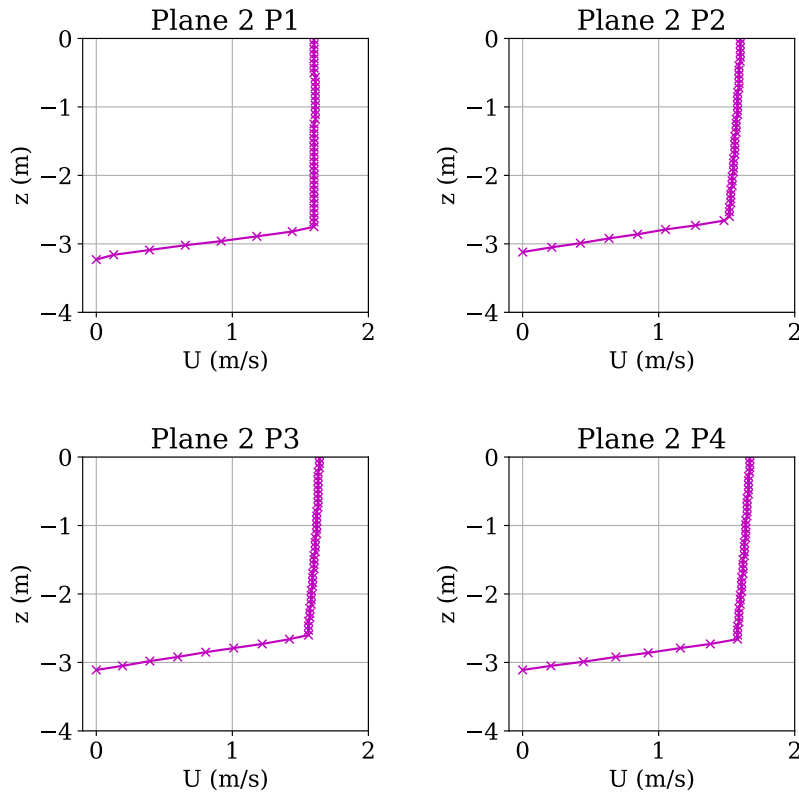


Figure 4.33 – Simulated velocity profiles of plane 2 with a mass flow rate \dot{m} of 158720 kg/s .

Table 4.7 – Mean velocity per section for a mass flow rate \dot{m} of 158720 kg/s .

Area	Velocity $U(m/s)$
Section 1 A	2.04
Section 1 B	1.83
Section 2	1.59
Section 5	1.93

Table 4.8 – Calculated converted power $P_{converted}$ per installation site for a mass flow rate \dot{m} of 158720 kg/s .

Area	Turbines	Power (kW)
Section 1 A	7	7.001
Section 1 B	4	2.888
Section 2	8	3.789
Section 5	5	4.235
Total power		17.913 kW

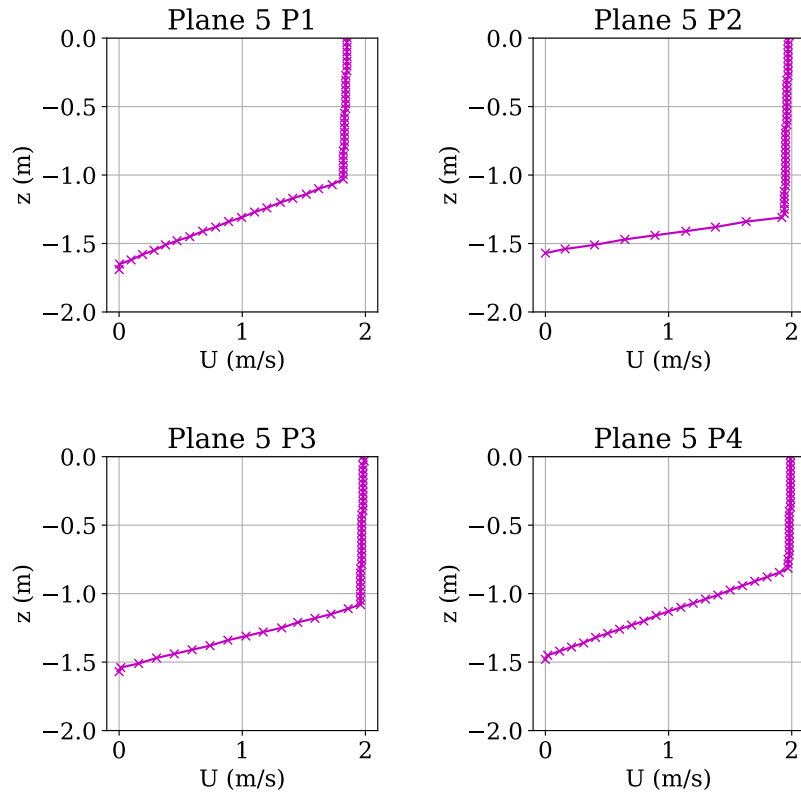


Figure 4.34 – Simulated velocity profiles of plane 5 with a mass flow rate \dot{m} of 158720 kg/s .

Table 4.9 – Annual potential power generation $P_{converted}$ of the turbine layout for 2018.

\dot{m} (kg/s)	Days	Total calculated power (kW)	Total calculated power per flow rate (kWh)
158720	165	17.913	70935.48
Annual calculated potential power generation capacity:			70.935 MWh

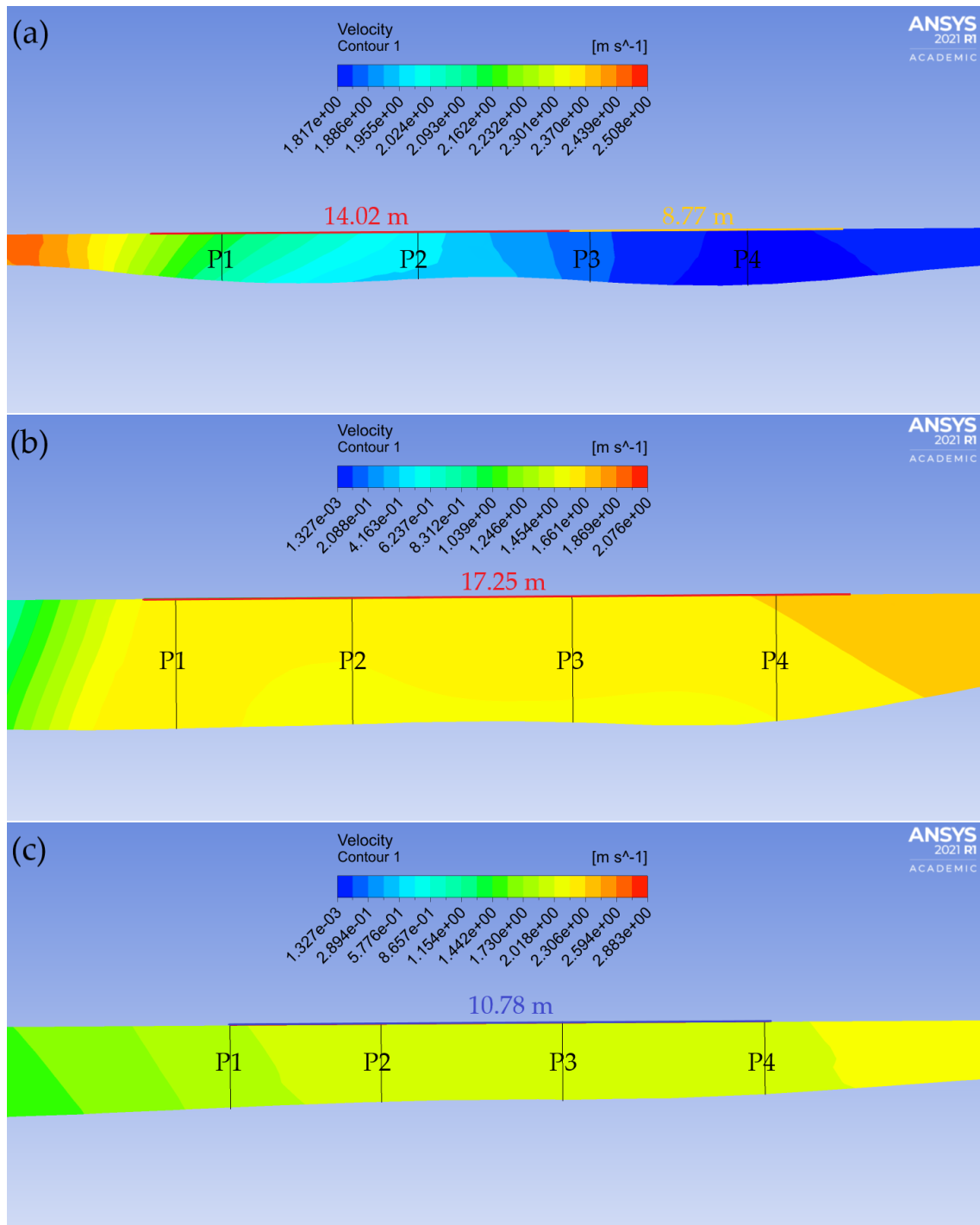


Figure 4.35 – Local velocity contours and depth for a mass flow rate \dot{m} of 158720 kg/s used for determining the available width for installation of the turbines for planes (a) 1, (b) 2 and (c) 5. The planes display the available width to its best advantage, causing the colder and warmer colours (respectively the lowest and highest velocities), similar to the contours found in Figures 4.15, 4.16 and 4.19, to be excluded.

4.7 DISTINGUISHING CHARACTERISTIC OF THE SEFAC CHANNEL

The end of this chapter is dedicated to a notable characteristic of the Sefac channel. As every natural channel has its own characteristics, the depression area right after the inlet is the feature that sets this natural channel apart from others. This area is the deepest area over the whole channel domain at 24.5 m. The depth in this area is most likely caused by the force of the ejected water from the hydroelectric facility after passing through the turbines.

The area displays extremely low velocities, as is expected of deeper areas. Geometrically, the longitudinal section of the area can be compared with a familiar problem in the theory of fluid flow: lid-driven cavity flow. To this purpose, the longitudinal velocity in this area generated by the RSM is studied in Fig. 4.36. This image presents not only the longitudinal velocity, but also how this variable changes with an increased mass flow rate.

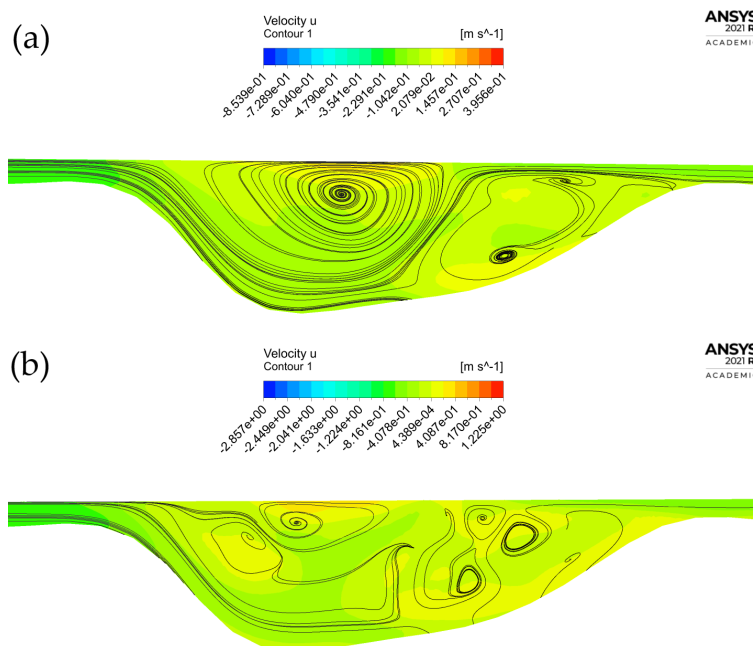


Figure 4.36 – Longitudinal velocity u with velocity streamlines of the longitudinal section (side view) of the depression area for mass flow rates \dot{m} (a) 47410 and (b) 158720 kg/s.

The longitudinal velocity at Fig. 4.36a presents slight variances in contours in the cavity. The velocity appears to be lower before and after the water passes the depression area. Similar to the lid-driven cavity flow case, the depth of this area causes the appearance of strong secondary flow in this part of the channel. The surface flow creates a shearing force, moving the fluid in the depression area, where as a result,

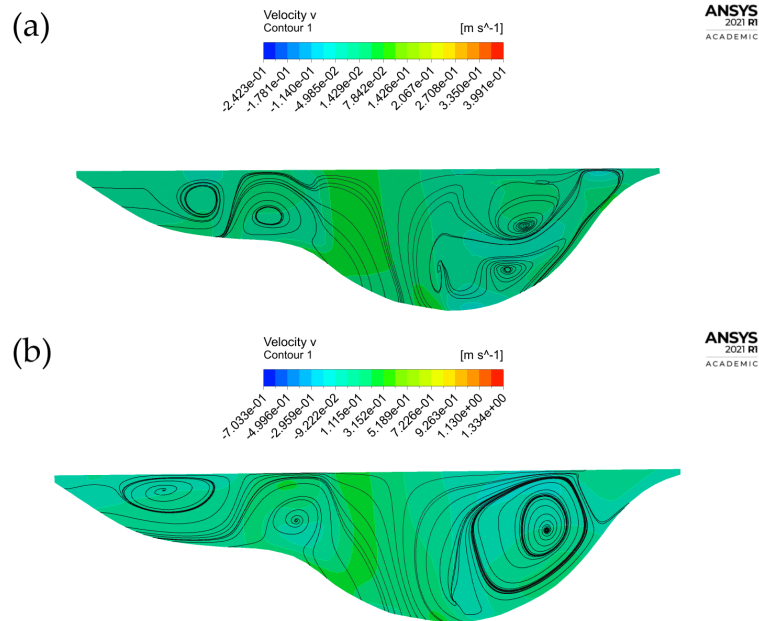


Figure 4.37 – Transverse velocity v with velocity streamlines of the cross section of the depression area for mass flow rates \dot{m} (a) 47410 and (b) 158720 kg/s .

a primary vortex and smaller vortices are created. The smaller vortices are formed due to changes in the channel wall. Compared to the original lid-driven cavity flow case, significant differences are observed. The original case has a higher longitudinal velocity u near the surface and lower in the cavity. Nonetheless, there is a fundamental similarity between both cases, which is the formation of the vortices. In the depression case, the primary vortex is generated in the deepest part of the depression, while the shallower areas show the formation of the smaller vortices. An increased mass flow rate causes the variances in the contours to become more pronounced. However, the primary vortex appears to dissolve into smaller vortices. This may indicate that with a higher longitudinal velocity, the secondary flow will decrease strongly.

The cross section also shows strong swirling secondary flow in Fig. 4.37. Similar to the longitudinal contours, the transverse velocity contours only show slight variations within the depression itself. Contrary to the longitudinal case, the secondary flow appears to become stronger with increasing mass flow rate. For 47410 kg/s , there are several small vortices present, whereas for 158720 kg/s , the smaller vortices form a main vortex right where the depth begins to decrease near the right bank. As for the contours, they seem to grow less pronounced with an increasing mass flow rate.

This depression area is a clear example of the reason of avoiding such areas for the installation of turbines. Not only is there not sufficient velocity for powering on the turbines, but the low velocity also causes a slow flow between 0.4 and 0.0003 m/s (see the velocity contours presented in Fig. 4.13) with low pressure gradients, impairing the

efficiency of the turbine and in long-term eventually impacting the turbine lifespan. This depression area proves that the proposed numerical method can also simulate strong secondary flow in natural channels.

5 CONCLUSION AND RECOMMENDATIONS

"Gotta blast!"

-Jimmy Neutron, Boy genius

5.1 CONCLUSION

The methodology developed to estimate the hydrokinetic energy potential for the Sefac channel has been validated by employing a benchmark channel. This validation brought forth the following:

1. The flow in the benchmark channel is heavily influenced by boundary layers and interactions between the main channel and floodplain;
2. Out of three tested turbulence models, a RSM, the $k - \varepsilon$ model and the RNG $k - \varepsilon$ model, the RSM was able to predict the flow near the wall and free surface the most accurately and consistently compared to the experimental data by Jing et al. (2011) [31];
3. The proposed methodology is able to simulate strong secondary flow similar to the flow structures found in Jing et al. (2011) [31].

Validating the methodology allowed for proceeding with the natural channel simulations. The Sefac channel displays a compound and trapezoidal cross section, consolidating the choice in benchmark channel. Following the initial simulation with a mass flow rate of 91000 kg/s , three planes were found to contain the highest velocities of $\approx 1 m/s$ and depths of higher than 1.5 m and low to no secondary flow. The velocity profiles of these three planes were further studied for two additional flow rates, derived from a 20-day moving average graph of the daily measured flow rate in 2018. The profile behavior was not noticeably influenced by the changing flow rate. Although, as expected, the velocity value showed drastic increase. In the end, the lowest flow rate simulations were not considered for the annual power estimation, as a result of their low velocities, leaving the turbine layout to be decided by results obtained from the

158720 kg/s simulation. According to this flow rate, the optimal turbine layout is as follows:

- Plane 1 divided in two sides, with an available width for installing a total of 11 turbines;
- Plane 2 with an available width for installing a total of 8 turbines;
- Plane 5 with an available width for installing a total of 5 turbines.

The turbines can generate up to $\approx 18 kW$, leading up to an annual estimated generation of $\approx 71 MWh$. Important to take into consideration is the subestimation of the annual potential generation for 2018, as the velocities simulated with 158720 kg/s are higher than the velocity used to calculate the turbine efficiency.

Taking into consideration all the findings in this research, can be concluded:

1. The main objective has been achieved. The developed methodology is capable of assessing the hydrokinetic potential in natural channels, employing a RANS turbulence model, high velocity, sufficient depth and low turbulence levels;
2. The knowledge gap in the literature is fulfilled, as the computational mesh consisting out of bathymetric data has been simulated by the methodology and during the turbine siting process the negative impacts of turbulence and secondary flow have been taken into consideration. Fortunately, the selected planes display no great turbulence, as no rotating secondary current fields nor high levels of turbulence are encountered. Additionally, it has also been proven through the strong secondary flow in the depression area, that the proposed numerical method is capable is simulating this type of flow in natural channels. The methodology is thus consolidated as trustworthy and versatile.

5.2 FUTURE WORKS

In future researches, a more accurate prediction of the annual power generation can be made by determining the turbine efficiency with a more suitable peak velocity. The velocities in the installation area per plane (and per plane division) can be employed as peak velocities, determining a specific turbine efficiency for the installation area, and thus a more accurate value for the potential power generation.

For a better indication of the flow rate to simulate, an extensive statistical analysis must be carried out to determine the frequent occurring flow rates within the channel.

Desired would also be discover the maximum flow rate, as within the frequent occurring flow rates in this work, only one could be employed for the annual potential power calculation, as the remaining two contained low velocities. Thus, for a more accurate assessment, it is important to know exactly during which time periods the turbines will be able to convert energy.

On the subject of a more accurate assessment of the hydrokinetic energy, velocities closest to the flow in the actual Sefac channel would also support and strengthen the results. This can be obtained through a comparison between the simulated results and experimental results. The experimental results would be collected directly from the Sefac channel by an Acoustic Doppler Profiler (ADP). Information on the data collection with the ADP device is provided in appendix A.

Assessing the hydrokinetic potential in the Sefac channel is only the beginning of an extensive process. The actual energy conversion will be influenced by more factors, such as the changing flow field after installing the turbine. A potential future work can thus be to simulate this channel with the turbine farm installed. This way, clear results can be obtained as to what the actual energy conversion will be and by what factors this conversion process is exactly influenced.

BIBLIOGRAPHY

- [1] Tominaga Akihiro and Nezu Iehisa. Turbulent structure in compound open-channel flows. *Journal of Hydraulic Engineering*, 117(1):21–41, jan 1991.
- [2] F Ali, C Srisuwan, K Techato, A Bennui, T Suepa, and D Niammuad. Theoretical hydrokinetic power potential assessment of the u-tapao river basin using gis. *Energies*, 13, 2020.
- [3] Inc. ANSYS. 4.2.3 boussinesq approach vs. reynolds stress transport models. ANSYS FLUENT 12.0/12.1 Documentation 23 Jan. 2009 <<https://www.afs.enea.it/project/neptunius/docs/fluent/html/th/node47.htm#sec-bouss-vs-rst>>, January 2009.
- [4] Inc. ANSYS. 4.3.1 overview. ANSYS FLUENT 12.0/12.1 Documentation. 23 Jan. 2009 <<https://www.afs.enea.it/project/neptunius/docs/fluent/html/th/node49.htm>>, January 2009.
- [5] Inc. ANSYS. 4.4.2 rng k - ϵ model. ANSYS FLUENT 12.0/12.1 Documentation. 23 Jan. 2009 <<https://www.afs.enea.it/project/neptunius/docs/fluent/html/th/node59.htm>>, January 2009.
- [6] André Bakker. Turbulence models. Lectures on Applied Computational Fluid Dynamics <<https://www.bakker.org/Lectures-Applied-CFD.pdf>>, 2008.
- [7] P A V Barbosa, C J C Blanco, A L A Mesquita, and Y Secretan. A simplified methodology for the analysis of the establishment of hydrokinetic parks downstream from hydroelectric plants . *Revista Ambiente e Agua*, 13(3), 2018.
- [8] N B Baryshnikov, G V Zheleznyakov, and Yu. M Natal'chuk. Investigation of the flood-flow process in channels with flood plains. *Hydrotechnical Construction*, 6:787–790, 1972.
- [9] Antonio C. P. Brasil Junior, Rafael C. F. Mendes, Theo Wirrig, Ricardo Noguera, and Taygoara F. Oliveira. On the design of propeller hydrokinetic turbines: the effect of the number of blades. *JOURNAL OF THE BRAZILIAN SOCIETY OF MECHANICAL SCIENCES AND ENGINEERING*, 41(6), JUN 2019.
- [10] Ismail B. Celik. Introduction to turbulence modeling. Lecture Notes Overview of Turbulence Models for Industrial Applications <<http://www.fem.unicamp.br>>, December 1999.

- [11] Ismail B. Celik. Introductory turbulence modeling. Lecture Notes <<http://www.fem.unicamp.br>>, December 1999.
- [12] S.U. Choi and H Kang. Reynolds stress modeling of turbulent open-channel flows. In *Water Resources Research Progress*, Seoul, South Korea, 2008.
- [13] SUNG-UK CHOI and HYEONGSIK KANG. *NUMERICAL TESTS OF REYNOLDS STRESS MODELS IN THE COMPUTATIONS OF OPEN-CHANNEL FLOWS*. WORLD SCIENTIFIC, 7 2002. doi:10.1142/9789812777591_0008.
- [14] Gary Coleman and Richard Sandberg. A primer on direct numerical simulation of turbulence – methods, procedures and guidelines, 3 2010.
- [15] COMSOL. Navier-stokes equations. Multiphysics cyclopedia 22 Feb. 2017 <<https://www.comsol.com/multiphysics/navier-stokes-equations>, February 2017.
- [16] J D S Cruz, C J C Blanco, and A C P Brasil Junior. Flow-velocity model for hydrokinetic energy availability assessment in the amazon. *Acta Scientiarum - Technology*, 42, 2020.
- [17] Narasimhamurthy V D. Unsteady-rans simulation of turbulent trailing-edge flow, 2004.
- [18] Patrícia da Silva Holanda, Claudio José Cavalcante Blanco, André Luiz Amarante Mesquita, Antônio César Pinho Brasil Junior, Nelio Moura de Figueiredo, Emanuel Neirão Macêdo, and Yves Secretan. Assessment of hydrokinetic energy resources downstream of hydropower plants. *Renewable Energy*, 101:1203–1214, 2 2017.
- [19] Lard Davidson. An introduction to turbulence models. Publication 97/2 <<http://www.tfd.chalmers.se/~lada>>, January 2003.
- [20] Zafer Defne, Kevin A Haas, and Hermann M Fritz. Numerical modeling of tidal currents and the effects of power extraction on estuarine hydrodynamics along the Georgia coast, USA. *Renewable Energy*, 36(12):3461–3471, 2011.
- [21] Paul Duvoy and Horacio Toniolo. Hydrokal: A module for in-stream hydrokinetic resource assessment. *Computers Geosciences*, 39:171–181, 2012. Assessment tool for hydrokinetic energy.
- [22] T Fischer-Antze, T Stoesser, P Bates, and N R B Olsen. 3d numerical modelling of open-channel flow with submerged vegetation. *Journal of Hydraulic Research*, 39(3):303–310, jul 2001.

- [23] Junke Guo and Pierre Juliény. Shear Stress in Smooth Rectangular Open-Channel Flows. *Journal of Hydraulic Engineering-asce - J HYDRAUL ENG-ASCE*, 131, jan 2005.
- [24] Yakun Guo, Hefang Jing, and Chunguang Li. Numerical simulation of compound meandering open channel flow. In *33rd IAHR Congress*, Aberdeen, Scotland, 2009.
- [25] M S Güney. Evaluation and measures to increase performance coefficient of hydrokinetic turbines. *Renewable and Sustainable Energy Reviews*, 15(8):3669–3675, 2011.
- [26] M S Güney and K Kaygusuz. Hydrokinetic energy conversion systems: A technology status review. *Renewable and Sustainable Energy Reviews*, 14(9):X2996–3004, 2010.
- [27] W I Ibrahim, M R Mohamed, R.M.T.R. Ismail, P K Leung, W W Xing, and A A Shah. Hydrokinetic energy harnessing technologies: A review. *Energy Reports*, 7:2021–2042, 2021.
- [28] Nezu Iehisa and Rodi Wolfgang. Open-channel flow measurements with a laser doppler anemometer. *Journal of Hydraulic Engineering*, 112:335–355, 5 1986. doi: 10.1061/(ASCE)0733-9429(1986)112:5(335).
- [29] Jinhee Jeong, Fazle Hussain, Wade Schoppa, and John Kim. Coherent structures near the wall in a turbulent channel flow. *Journal of Fluid Mechanics*, 332(188):185–214, February 1997.
- [30] H Jing, Y Guo, C Li, and J Zhang. Three-dimensional numerical simulation of compound meandering open channel flow by the reynolds stress model. *International Journal for Numerical Methods in Fluids*, 59(8):927–943, mar 2009.
- [31] Hefang Jing, Chunguang Li, Yakun Guo, and Weilin Xu. Numerical simulation of turbulent flows in trapezoidal meandering compound open channels. *International Journal for Numerical Methods in Fluids*, 65:1071 – 1083, 03 2011.
- [32] Antonio Cesar Pinho Brasil Junior, Taygoara F. Oliveira, Claudio José Cavalcante Blanco, Rafael Castilho Faria Mendes, and Sergio de Oliveira Frontin (organizers). *Turbinas Hidrocinéticas Fluviais: tecnologias, potencial hidrocinético e impactos ambientais*. 2022.
- [33] Asif Kabir, Ivan Lemongo-Tchamba, and Arturo Fernandez. An assessment of available ocean current hydrokinetic energy near the North Carolina shore. *Renewable Energy*, 80:301–307, 2015.
- [34] B Kamel, K Ilhem, F Ali, and D Abdelbaki. 3d simulation of velocity profile of turbulent flow in open channel with complex geometry. In Hamieh T., editor, *8th*

International Conference on Material Sciences, CSM8-ISM5 2012, volume 55, pages 119–128, Institute of Civil Engineering, Hydraulics and Architecture, University Hadj Lakhdar, Batna 05000, Algeria, 2014. Elsevier B.V.

- [35] Hyeongsik Kang and Sung-Uk Choi. Reynolds stress modeling of rectangular open-channel flow. *International Journal for Numerical Methods in Fluids*, 51:1319 – 1334, 08 2006.
- [36] Dan Kirby, Pegler Kevin, and Coleman David. Gis for hydrological modelling-gagetown hydrologic model, 6 2011.
- [37] D W Knight and K Shiono. Turbulence measurements in a shear layer region of a compound channel. *Journal of Hydraulic Research*, 28(2):175–196, mar 1990.
- [38] Y Liu and D J Packey. Combined-cycle hydropower systems - The potential of applying hydrokinetic turbines in the tailwaters of existing conventional hydropower stations. *Renewable Energy*, 66:228–231, 2014.
- [39] MANUEL LUIS MAGALHAES DE LIMA DA SILVEIRA E LORENA. *Meandering Compound Flow*. PhD thesis, University of Glasgow, United Kingdom, 6 1992.
- [40] Salim M, K Ong, and S C Cheah. Comparison of rans, urans and les in the prediction of airflow and pollutant dispersionw. In *Proceedings of the World Congress on Engineering and Computer Science 2011 Vol II*, San Fransisco, 2011.
- [41] GEORGE L MELLOR and H JAMES HERRING. A survey of the mean turbulent field closure models. *AIAA Journal*, 11:590–599, 5 1973. doi: 10.2514/3.6803.
- [42] Parviz Moin and John Kim. Numerical investigation of turbulent channel flow. *Journal of Fluid Mechanics*, 118:341–377, 1982.
- [43] Sueli Montenegro. Estudo revela potencial de produção de energia hidrocínética de 2,4 mw em curuá-una. CanalEnergia.com.br. 28 April. 2016 <<https://www.canalenergia.com.br/noticias/17341428/estudo-revela-potencial-de-producao-de-energia-hidrocinetica-de-24-mw-em-curuaua>>, April 2004.
- [44] C M Niebuhr, M van Dijk, V S Neary, and J N Bhagwan. A review of hydrokinetic turbines and enhancement techniques for canal installations: Technology, applicability and potential. *Renewable and Sustainable Energy Reviews*, 113, 2019.
- [45] J Rotta. Statistische theorie nichthomogener turbulenz. *Zeitschrift für Physik*, 129:547–572, 1951.

- [46] Portal Solar S.A. Fontes de energia renováveis: Tudo o que você precisa saber. Fontes de energia renováveis. April. 2015 <<https://www.portalsolar.com.br/fontes-de-energia-renovaveis.html>>, April 2015.
- [47] G Saini, A Kumar, and R P Saini. Assessment of hydrokinetic energy - a case study of eastern yamuna canal. *2020 International Conference on Innovations in Clean Energy Technologies, ICET 2020*, 46:5223–5227, 2020.
- [48] I.F.S.D. Santos, R G R Camacho, G L Tiago Filho, A C B Botan, and B A Vinent. Energy potential and economic analysis of hydrokinetic turbines implementation in rivers: An approach using numerical predictions (cfd) and experimental data. *Renewable Energy*, 143:648–662, 2019.
- [49] Koji Shiono and Donald W Knight. Turbulent open-channel flows with variable depth across the channel. *Journal of Fluid Mechanics*, 222:617–646, 1991.
- [50] Manoj Sood and Sunil Kumar Singal. Development of hydrokinetic energy technology: A review. *International Journal of Energy Research*, 43:5552–5571, 9 2019. doi: 10.1002/er.4529.
- [51] C G Speziale and S Thangam. Analysis of an rng based turbulence model for separated flows. *International Journal of Engineering Science*, 30:1379–IN4, 1992.
- [52] Charles Speziale, Sutanu Sarkar, and T Gatski. Modelling the pressure-strain correlation of turbulence - an invariant dynamical systems approach. *Journal of Fluid Mechanics*, 227, 7 1991.
- [53] H. S. Tang, K. Qu, G. Q. Chen, S. Kraatz, N. Aboobaker, and C. B. Jiang. Potential sites for tidal power generation: A thorough search at coast of new jersey, usa. *Renewable and Sustainable Energy Reviews*, 39:412–425, 2014.
- [54] H Tennekes and J L Lumley. *A First Course in Turbulence*. 1972.
- [55] M. Thiébaud and A. Sentchev. Tidal stream resource assessment in the dover strait (eastern english channel). *International Journal of Marine Energy*, 16:262–278, 2016.
- [56] M Vaghefi, M Akbari, and A R Fiouz. An experimental study of mean and turbulent flow in a 180 degree sharp open channel bend: Secondary flow and bed shear stress. *KSCCE Journal of Civil Engineering*, 20(4):1582–1593, 2016.
- [57] David Wilcox. *Turbulence Modeling for CFD (Third Edition) (Hardcover)*. DCW Industries, jan 2006.

- [58] Ming-Liang Zhang, C.W. Li, and Yong-Ming Shen. A 3d non-linear k- turbulent model for prediction of flow and mass transport in channel with vegetation. *Applied Mathematical Modelling*, 34(4):1021–1031, 2010.
- [59] Xiaowei Zhang, Xiao-Li Jin, Yin Wang, Keenjoe Deng, and Zhong-Ming Ren. Comparison of standard k- model and rsm on three dimensional turbulent flow in the sen of slab continuous caster controlled by slide gate. *ISIJ International*, 51:581–587, 4 2011.

APPENDIX

A BATHYMETRIC DATA ACQUISITION

In order to model the Sefac channel as realistically as possible, the bathymetric data of the river section must be collected. The field data of the Sefac channel is gathered by carrying out depth measurements with a Sontek M9 device, an ADP. This tool has the ability to simultaneously measure the water velocity and river bathymetry. The ADP emits an ultrasonic acoustic wave into the water and measures the backscatter's time from the river bottom and small particles. Following the Doppler effect principles, it becomes possible to compute the depth and the velocity components over the measured water column. The device was assembled in a boat, as shown in Fig. A.1, and was driven along the river. Under this set up, the bathymetric data was obtained following the trajectories presented in Fig. A.2.



Figure A.1 – Setup of the field experiments through a (a) boat with (b) the ADP assembly.

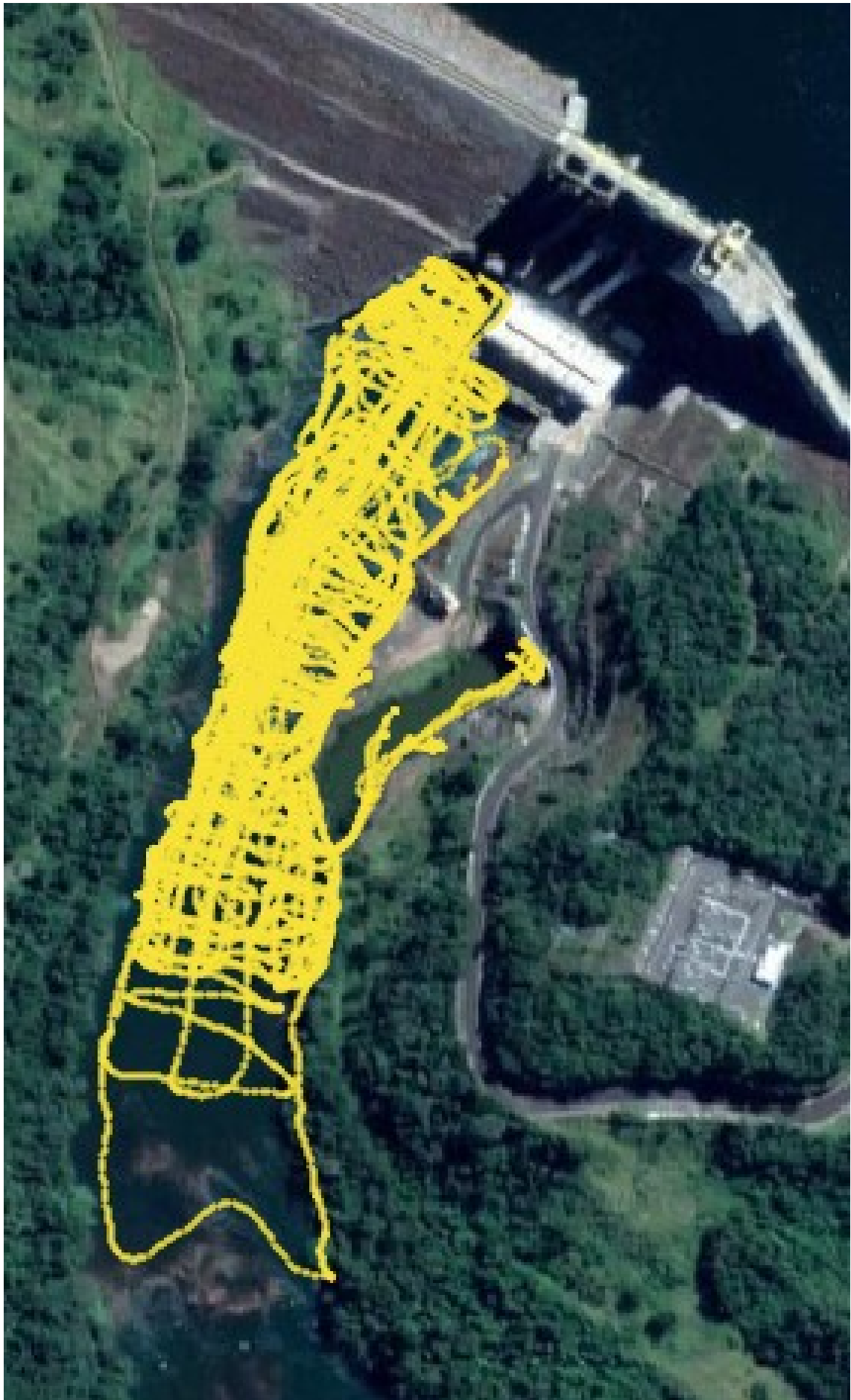


Figure A.2 – Boat trajectories on the channel taken for the measured depth.

B HYDROKINETIC TURBINE ROTOR DESIGN AND TURBINE EFFICIENCY

In order to estimate how much hydrokinetic energy can be converted into electrical energy, the performance of a hydrokinetic turbine rotor under similar flow conditions must be assessed. With the turbine efficiency determined, the potential power of a turbine farm layout can be calculated.

To this end, it is necessary to understand how the interaction between the turbine blade and fluid flow takes place. The Blade Element Momentum Theory (BEMT) serves as a quick, robust and effective tool to not only study the forces on the blade leading to the conversion process and also designing the rotor. It is a description of an integral formulation involving classical equations of fluid mechanics, quantifying the energy conversion process in hydrokinetic turbine blades. As the BEMT is a semi-empirical method, adjustments and corrections may always be implemented to improve the accuracy of the results obtained, considering complex hydrodynamic phenomena, such as blade tip vortex and cavitation [9].

In general, the behavior of a hydrokinetic turbine can be described by two dimensionless variables: the power coefficient, C_p , which expresses its efficiency in relation to the available power; and the blade tip speed, λ , defined, respectively, by

$$C_p = \frac{P_{converted}}{P_{available}} = \frac{\omega T}{0.5\rho A U_\infty^3} \quad (\text{B.1})$$

and

$$\lambda = \frac{\omega R}{U_\infty}. \quad (\text{B.2})$$

in which ω is the runner angular speed, T the torque at the axis, ρ the water density, A the rotor cross sectional area, U_∞ the water flow velocity and R the rotor radius.

Thus, the BEMT method is used as a rotor design tool to compute the C_p , under pre-established operating conditions. This tool can thus also be employed to optimize a geometry. The BEMT algorithm consists of dividing the rotor into elements, assuming complete independence between them. Subsequently, the momentum theory is used for the element, computing the torque by

$$dT = 4\pi r^3 \rho U \omega (1 - a) a' dr, \quad (\text{B.3})$$

in which a e a' are respectively the axial and tangential induction factors. More details on these variables can be found in [9].

The torque, T can also be obtained through the BEM by

$$dT = \frac{1}{2} \rho N_b C \frac{U(1 - a)\omega(1 + a')}{F \sin \phi \cos \phi} C_t dr, \quad (\text{B.4})$$

in which N_b is the number of rotor blades, C the hydrofoil chord in r and the variables C_t e C_n are defined by the drag and lift coefficient (C_l and C_d) as

$$C_t = C_l \sin \phi - C_d \cos \phi, \quad (\text{B.5})$$

and

$$C_n = C_l \cos \phi + C_d \sin \phi. \quad (\text{B.6})$$

Ultimately, the rotor design consists out of a interactive process employing the equations listed previously and following the algorithm below to define the yet to be computed variables:

1. Initial guess for the variables a and a' ;
2. Compute the flow velocity at the blade element;
3. Determine the values of the drag and lift coefficient, carried out by the XFOIL software;
4. Recalculate the variables a and a' ;
5. Continue until the method converges.

The parameters employed to design the rotor are based on field measurements and simulations are presented in Tab. B.1.

The applied parameters result in the geometry presented in Fig. B.1 and geometry information presented in Tab. B.2.

Following the selected method for designing the rotor, the turbine performance curve, $C_p \times \lambda$ is produced in Fig. B.2. The maximum performance of the turbine attains a power coefficient of approximately 0.3. This value occurs at the peak conditions given in Tab. B.1.

Water velocity	1.0 m/s
Rotational speed	40 RPM
Diameter	1.0 m
Hydrofoil	NACA4415
N^o of blades	5

Table B.1 – Inlet parameters of the rotor design based on BEM.

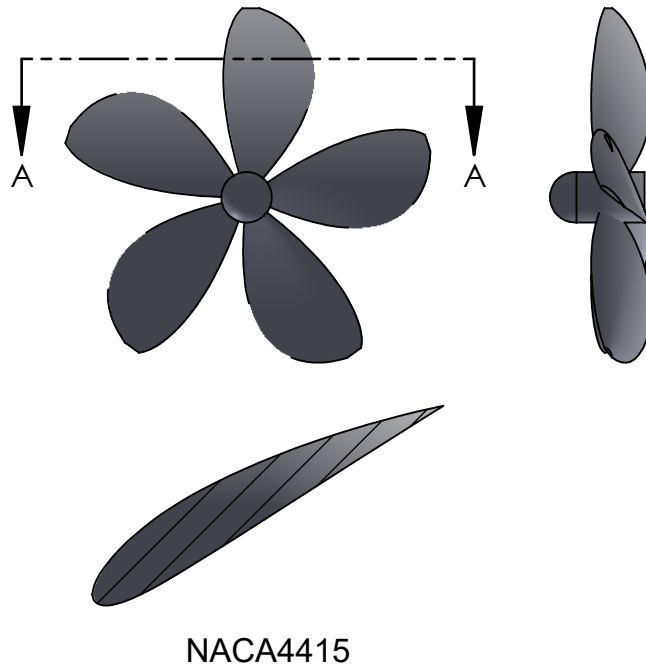


Figure B.1 – Rotor design.

Radius (m)	Chord (m)	Blade angle (°)
0.050	0.086	47.4
0.082	0.132	45.1
0.114	0.172	43.0
0.146	0.205	41.0
0.178	0.232	39.1
0.210	0.253	37.2
0.242	0.269	35.4
0.275	0.278	33.7
0.307	0.280	32.1
0.339	0.274	30.5
0.371	0.261	29.0
0.403	0.237	27.6
0.435	0.202	26.2
0.467	0.148	24.9
0.500	0.050	23.7

Table B.2 – Geometry of the resulting blade following the algorithm for the blade design.

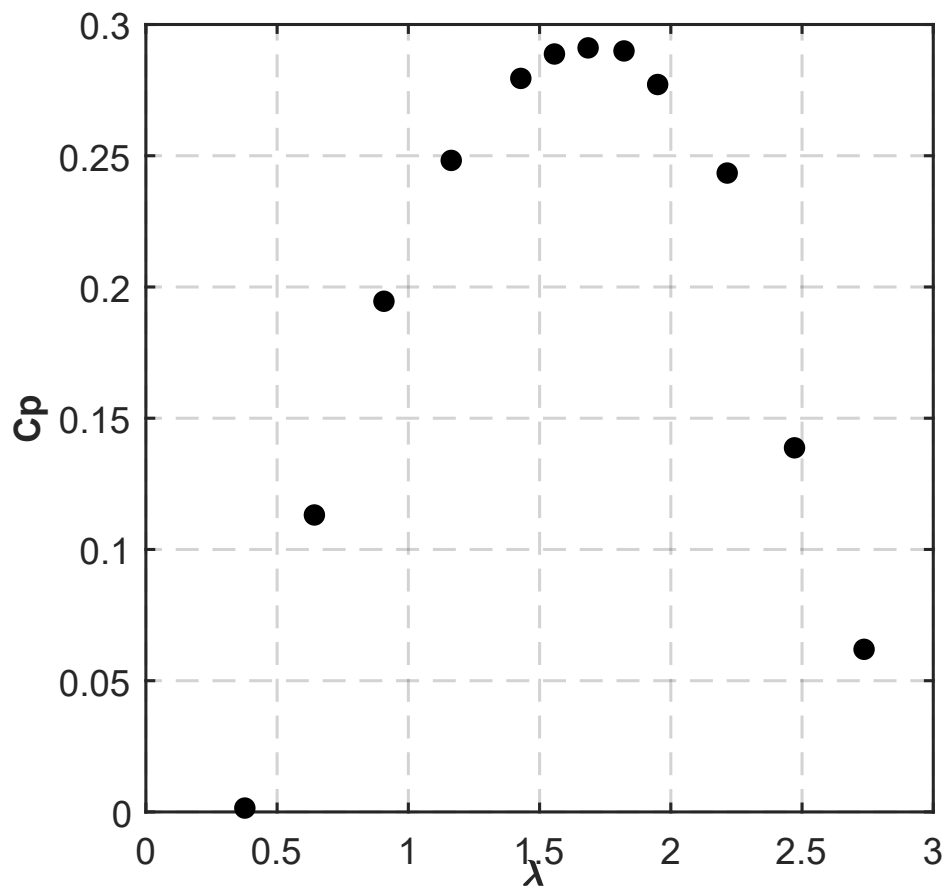


Figure B.2 – Estimated performance curve for the rotor design.